Effect of strain localization on tensile and fatigue characteristics in precipitation-strengthened steels

ヴィレンドラ, クマール, ヴェルマ

Effect of strain localization on tensile and fatigue characteristics in precipitation- strengthened steels

A dissertation submitted to

Graduate School of Engineering, Kyushu University, Japan

for the degree of Doctor of Engineering in Hydrogen Energy System

KYUSHU
UNIVERSITY

Presented by

VIRENDRA KUMAR VERMA

August 2020

Table of Contents

Abstract

The present study deals with the mechanical behaviour of precipitation-strengthened steels under different loading conditions and environments. There are three different types of steel chosen for this purpose. All the three steels basically differ in the nature of precipitates they bear. Since the nature of precipitates is different, their influence on the mechanical behaviour of the material is also different. The behaviour of these steels is understood based on the strain localization phenomenon.

The steels having soft copper (Cu) precipitate, hard titanium carbide (TiC) precipitate and γ′ [$Ni_3(Al,Ti)$] precipitates is designated here as C6, T6 and SUH 660 respectively. C6 and T6 are the two special steels developed in order to have the same tensile properties and micro-hardness. While SUH 660 is commercial austenitic stainless steel having γ′ precipitates, and is a candidate material for hydrogen environment.

The study is broadly divided into four parts. The first part, studies about the fatigue damage behaviour of C6 and T6 for an arbitrary crack length. The second and third part, studies the damage evolution behaviour of SUH 660 under uniaxial tensile loading in ambient environmental conditions and in hydrogen environment respectively. The fourth part, studies the evolution of fatigue crack in SUH 660 under ambient environmental conditions.

Since for C6 and T6 tensile strength is the same, the difference arises out of the nature of precipitate and microstructure, T6 having hard precipitate and fine microstructure shows strain localization. Thus a transition is forecasted in the fatigue behaviour. This leads to carrying out the fatigue experiments for C6 and T6 for an arbitrary initial crack length. The results show that C6 and T6 have better fatigue crack resistance in the short crack and long crack region, respectively. Since T6 bear hard precipitate and C6 bear soft precipitate, a strain localization can be expected in the case of T6. However, hardness of precipitate is not the only parameter to decide strain localization, it may be due to non-uniform distribution of TiC precipitates in the metal. Thus, strain localization in T6 is confirmed by DIC (digital image correlation) results. The plastic zone in the case of T6 is narrow and asymmetrical. Better fatigue performance of C6 in short crack regime is because of effective plasticity induced crack closure (PICC), as a result of uniform and

symmetric plastic zone formation. For the long crack regime, T6 develops a more uniform plastic zone, thus neutralising the advantage of C6. In this regime, the hard precipitates and fine grain are held responsible for better fatigue performance of T6.

In the case of SUH 660, the precipitates have an indirect influence on the damage evolution behaviour. The precipitates result in anti-phase boundary formation which suppresses the tendency of cross-slipping. This inefficiency of cross-slip result in strain accumulation, as the stress accommodation capability is reduced because of slip planarity. This results in the damage initiation at the inclusions and grain boundary. The voids thus generated successively grows by coalescence and shearing of the ligament. This phenomenon is highly aggravated in hydrogen environment as the tendency of crack initiation resistance and propagation resistance is reduced. The cracks formed are relatively sharp and wide open. As the hydrogen charging current density is increased the nature of fracture shows a transition from quasi-cleavage to inter-granular fracture. Transportation of hydrogen, to the grain boundary, with the help of dislocation motion, results in inter-granular fracture when the concentration of hydrogen reaches a critical concentration.

In the case of fatigue loading, it is very surprising to notice that the crack does not evolve from the inclusion. The fatigue experiments show that the crack initiates from some location other than the artificial defect. This gives an idea of self-generated initial flaw. Surface and fractographic observations show that the crack has initiated from the grain itself, that points towards the possibility of grain acting as the initial defect due to considerable strain localization in the grain. This is the reason why SUH 660 show low fatigue limit, as expected from its tensile strength.

Chapter 1 Introduction

1.1 Background

1.1.1 Steels strengthened by precipitates

Methods have been devised in order to increase the yield strength, ductility and toughness of metals [1]. Plastic deformation is a result of dislocation motion and consecutive multiplication. In order to enhance the material's mechanical property, we need to introduce a mechanism so as to prohibit the motion of dislocation [2]. The various mechanisms proposed for this purpose are work hardening, solid solution strengthening, precipitation-strengthening, grain boundary strengthening, transformation hardening, and so on [3].

Precipitation-strengthening, also known as age hardening or particle hardening, is a heat treatment process that is used to increase the yield strength of metals. This is the common technique used for most of the structural alloys like aluminium, magnesium, nickel, titanium and some steels [4, 5]. In fact, in superalloys, it results in excellent high-temperature strength. Precipitation-strengthening relies on the change in solid solubility with the temperature that results in fine particles of impurity phase. This results in the dispersion of the hard/ soft particles within metal grain structure, thus creating hindrance in the dislocation motion [6, 7]. Since dislocations are the dominant carriers of plasticity, this will lead to material hardening [8, 9]. Unlike ordinary tempering, in this process the metal is held at elevated temperature for a considerable time to allow the precipitation to take place. This time lag is called as "aging". Solution treatment and aging are sometimes referred to as STA in specification sheets of the alloy.

The mechanics of force particle interaction in the case of precipitation-strengthening is shown in Fig. 1.1. The force acting on a mobile dislocation in a stressed metal containing a dispersion of second phase particle is shown schematically. Considering the balance of force between the line tension, T, of dislocation and resistance force, F, of the second phase particle yields [10],

$$F = 2T \sin\theta \tag{1.1}$$

As F increases, bowing of the dislocation increases, thus θ increases. The magnitude of resistance force is a deciding factor for the sequence of events. The dislocation line tension will be maximum when $\theta = \frac{\pi}{2}$ radians.

If the second phase particle is hard, such that the resistance force F is greater than $2T$, then the dislocation will bypass the particle either by Orowan looping [10] or cross-slip and the particle will remain undeformed (Fig. 1.2). In this situation the actual strength of the particle is irrelevant and the bypassing operation will depend only on the inter-particle spacing. In case, the strength of the particle is such that the maximum resistance force is attained before $\sin\theta = 1$, the particle will be sheared off and the dislocation will pass through the particle (Fig. 1.3).

It therefore concludes that, for a given inter-particle spacing, hard particles will result in maximum precipitation-strengthening and this condition defines the maximum degree of strengthening attainable. Soft particles will result in a lesser degree of strengthening [11, 12].

The particle size dependence of the hardening process is variable and depends on whether the particle belongs to a regime of small particle or large particle. When the particles are relatively small, one solution, relevant to very limited dislocation bending, yields [13]

$$\Delta\tau_y = 4.1\, G\varepsilon^{3/2}(rf/b)^{1/2} \tag{1.2}$$

where $\Delta\tau_y$ is the increase in yield stress due to the particles, G is the shear modulus of the matrix, ε is the misfit strain, r is the radius of the particle, f is the volume fraction of the particles, b is the Burgers vector of the dislocation.

In the case of large particles where considerable flexing of dislocations occurs as a result of the spacing of individual particles, any movement of the dislocation has to overcome a large number of obstacles per unit length [13]

$$\Delta\tau_y = 0.7\, Gf^{1/2}\varepsilon^{1/4}(b/r)^{3/4} \tag{1.3}$$

For small particles, strain hardening increases with increasing particle size, whereas, for the case of large particles the case is just reverse. This means that there will be a maximum in the strengthening at a critical particle size which is of the order of

$$r/b = \frac{1}{4}\,\varepsilon^{-1} \tag{1.4}$$

irrespective of volume fraction [13]. The net effect of increasing the particle size is shown in Fig. 1.4 using small and large particle strengthening equations. High precipitate particle density usually resists the dislocation motion, but the particle size needs to be considerable. Therefore, if the particles are coarse and hard enough, then the density will support the inhibition of dislocation motion [14].

A typical example of how dislocation-precipitate interaction will influence the mechanical behaviour of material is shown in Figs. 1.5 and 1.6 [15]. Here two loading conditions are considered one is under tensile loading, the other is under fatigue loading. This model is strongly based on dislocation pile-up, it states that the dislocation will easily pile-up at the precipitates, and if the precipitates are cut the dislocation pile-up somewhere else. Figure 1.5 shows the schematic diagram for dislocation accumulation for tensile loading. Figure 1.5(a) shows dislocation accumulation in non-strained specimen, whereas Fig. 1.5(b) shows the dislocation accumulation in the case of pre-strained specimen. In non-strained specimen the generated dislocation pile-up at the precipitates. With further accumulation of dislocation, the generated back stress will oppose the dislocation generation from dislocation source. So in the case of pre-strained specimen where the generated dislocation has already started accumulating, will result in the enhancement of tensile strength of material by pre-straining. On the other hand, in the case of fatigue loading (Fig. 1.6) where the source of dislocation is crack, a pre-straining phenomenon will result in the dislocation pile-up at some distance from crack (Fig. 1.6(b)). This will cause an ineffective back stress in the case of pre-strained specimen as compared to non-strained specimen (Fig. 1.6 (a)), thus reducing the fatigue life of pre-strained specimen. This shows that the mechanical behaviour of the material is highly dependent on dislocation-precipitate interaction.

1.1.2 Fatigue behavior of metals

1.1.2.1 Fatigue crack initiation

Because of repeated loading there is a continuous accumulation of localized irreversible slip at the microscopic stress concentration sites [16, 17] (grain/twin boundaries inherent in a polycrystalline material) resulting in material separation that is crack formation at micro-level [18]. At low cyclic stress, in pure metals, fatigue crack initiation takes place along the slip bands called persistent slip bands (PSBs). Ladder structures of PSBs provide free channel to dislocation motion and shear deformation is concentrated within the bands. Because of concentrated slip deformation under cyclic stresses surface roughness is formed, which results in the crack initiation along the slip band [19, 20]. Figure 1.7 shows the formation of extrusions and intrusions on the surface as a result of slip deformation [21]. Following crack nucleation, crack propagate incrementally through microstructural obstacles. Specific nature and distribution of these microstructural obstacles will dictate crack growth properties. The crack advancement in ductile metals can be categorized as: (a) microstructural sensitive stage I and microstructural independent stage II, shown in Fig. 1.8. Length of stage I crack is comparable to host grain dimensions. It advances by opening (mode I) and sliding (mode II and/or III) mechanisms. The crack grows along the slip system having maximum resolved shear stress, which differs from grain to grain, thus resulting in path tortuosity [22]. The driving force for stage I crack growth is influenced by the degree of obstruction and the irreversibility of the crack emitted slip. The extent of slip activities at the very early stage of crack growth is confined to only few grains. Eventually crack growth reaches stage II, where it is no longer affected by any interfaces and continues till final rupture. At this point, the plastic zone covers a multitude of grains (as opposed to a few grains in stage I) which gives rise to the observed microstructural-insensitivity of crack propagation as shielded by plastic envelope.

1.1.2.2 Fatigue crack closure

If the applied stress is not enough or the material has sufficient fracture toughness this will result in crack growth inhibition. Contrary to this there are several crack closure mechanisms proposed by previous researchers [23]. Some of the prominent crack closure

mechanism are as follows [24-27]: (a) plasticity induced crack closure (b) roughness induced crack closure (c) oxide induced crack closure (d) phase transformation induced crack closure. The phenomenon of plasticity-induced crack closure is due to the development of residual plastically deformed material on the wake of an advancing fatigue crack. This wake formation will result in effective crack closure as shown schematically in Fig. 1.9. It effects due to the misfit of the rough fracture surfaces of the crack lower and upper parts. As a result, these mismatch wedges come in contact during fatigue loading process, resulting crack closure (Fig. 1.10).

1.1.2.2 Effect of arbitrary crack length on fatigue behavior

Previous studies by the researchers classified the effect of initial crack size on the fatigue limit based on whether the crack is short or long. The detailed study by Murakami [28] on short cracks classified all the cracks whose $\sqrt{area} \leq 1000$ μm as short cracks and $\sqrt{area} > 1000$ μm as long cracks. Where, $\sqrt{area}$ is the square root of the area obtained by projecting a small defect or crack on a plane perpendicular to the maximum principal stress.

Suresh [29] classified the small crack into three categories in a non-corrosive medium as: microstructurally, mechanically and physically small cracks. For short cracks, intensive studies were carried out in order to trim down the parameters for fatigue strength prediction [30]. Since the fatigue limit considered here is the threshold condition for crack non-propagation, therefore it is rational to first consider ΔK_{th} (threshold stress intensity factor range) rather than directly jumping to fatigue limit stress amplitude, σ_w. The relationship of ΔK_{th} with $\sqrt{area}$ was already established [31-33], and is known to have a direct relationship with $\sqrt{area}$. The second most convenient material parameter that can be related to ΔK_{th} was Vickers hardness, *HV*. Thus, the two most important parameters, representing the material parameter and crack/defect geometrical parameter, are Vickers hardness and $\sqrt{area}$, respectively. The prediction equation thus established for calculating ΔK_{th} is as follows (R = -1) [28]

$$\Delta K_{th} = 3.3 \times 10^{-3} (HV + 120) \left(\sqrt{area}\right)^{1/3}. \quad (1.5)$$

The predicted values from the equation above are compared with the experimental results and it shows considerably less error, that is within $\pm$10 %.

For a surface crack [28],

$$K_{Imax} = 0.65\sigma_0\sqrt{\pi\sqrt{area}}\,. \tag{1.6}$$

By combining Eqns. (1.5) and (1.6) the fatigue limit, σ_w, of a cracked specimen can be expressed as [28]:

$$\sigma_w = 1.43(HV + 120)/\left(\sqrt{area}\right)^{1/6} \tag{1.7}$$

where σ_w is nominal stress amplitude, in MPa, defined using the gross area.

The applicability of Eqn. (1.7) is justified by the previous researcher [28] for different types of steels. The results of the comparison are well within the acceptable error band. As far as the limit of applicability of this expression is concerned the upper limit is proposed to be, $\sqrt{area}$ = 1000 μm. For the lower limit, if $\sqrt{area}$ is considered to be zero, the expression will give an infinite fatigue life. However, this seems to be quiet unreasonable, because crack usually nucleates along slip bands and grain boundaries as a result of reverse slip in grains [34, 35]. Thus $\sqrt{area}$ can never be zero and the defect free specimen will also have finite fatigue limit, σ_{w0}. The lower limit of $\sqrt{area}$ is supposed to be related to the length of the non-propagating crack for the un-notched /defect free specimen [36-38]. This gives the concept of no damage crack length, l_0, for which there will be no effect on fatigue limit, upto a certain crack length, l_0.

For the long crack, the theories proposed were quite different from the short crack. This is simply because the crack growth phenomenon as well as the crack closure

phenomenon is different for short crack and long crack. The definition of the crack being short or long depends on the evaluation parameter. When ΔK (stress intensity factor range) is used as an evaluation parameter, small scale yielding (SSY) condition is the deciding factor [39-42]. In order to avoid SSY condition, EPFM (elastic-plastic fracture mechanics) can also be used by the implication of parameter, J [43]. The disadvantage of this approach is that J depends on material but ΔK is a material independent parameter. The value of ΔK_{th} is constant for the case of long crack and is independent of crack length [12]. The crack length dependency of ΔK_{th} for short crack and long crack domain is shown in Fig. 1.11.

Usually short crack grows faster than a long crack, for identical nominal stress intensity factor [44, 45]. Moreover, the short cracks being of microstructural scale interacts more with the microstructural features, thus resulting in the straight path deviation, during crack propagation. The previous researcher proposed a unified model for both short crack and long crack based on barriers in crack propagation [46-48]. One of the microstructure based crack propagation models was Navarro-Rios model [49] which was later on modified by Vallellano et al. [50, 51] to include the effect of crack closure. Fatigue life calculations for the long crack domain is based on the well-know equation proposed by Paris-Erdogan [52]

$$\frac{da}{dN} = C\ (\Delta K)^m \tag{1.8}$$

where a is crack length; da/dN is crack growth rate; ΔK is stress intensity factor range; C and m are coefficients obtained experimentally.

For long crack ΔK_{th} is constant and is given by the expression [53]

$$\Delta K_{th} = (1 - R)(\Delta K_{eff,th} + \Delta K_{op,th}) \tag{1.9}$$

where R is the stress ratio ($\sigma_{min}/\sigma_{max}$); $\Delta K_{eff,th}$ is effective threshold stress intensity factor range; $\Delta K_{op,th}$ is threshold crack opening stress intensity factor range.

Because the crack in this domain follows the SSY condition, the size of the plastic zone is determined by ΔK, which corresponds to applied cyclic stress range and crack length [54]. Plasticity induced crack closure is caused by the plastic deformation left in the wake of the fatigue crack and thus ΔK_{op} depends on applied ΔK. This justifies that ΔK_{th} in Eqn. (1.9) is constant for long crack domain.

In order to predict the fatigue limit for the crack of any arbitrary length, we have

$$\Delta K_{th} = 2 \times 0.65 \sigma_w \sqrt{\pi \sqrt{area}}\,. \tag{1.10}$$

Therefore ,

$$\sigma_w = \frac{\Delta K_{th}}{2 \times 0.65 \sqrt{\pi \sqrt{area}}}\,. \tag{1.11}$$

Considering the threshold condition

$$\sigma_{eff,th} = \frac{\Delta K_{eff,th}}{2 \times 0.65 \sqrt{\pi \sqrt{area}}} \tag{1.12}$$

where $\sigma_{eff,th}$ is effective threshold stress.

The proposed prediction equation is [53]

$$\sigma_w' = \sigma_{w,R=-1} \left(\frac{1-R}{2}\right)^{\gamma} \tag{1.13}$$

where, σ_w' is fatigue limit with mean stress around zero; $\sigma_{w,R=-1}$ is fatigue limit for *R*= -1; γ is an exponent value that characterises the effect of means stress and depends on the crack size.

When mean stress is high, the proposed equation is

$$\sigma_w'' = \sigma_{eff,th} . \tag{1.14}$$

The fatigue limit thus proposed will be the maximum of the two values

$$\sigma_w = \max(\sigma_w', \sigma_w'') \tag{1.15}$$

1.1.3. Strain localization effects on tensile strength and fatigue limit

Plastic strain localization in materials occurs over a wide range of metals, under different loading conditions and applications. It often plays a crucial role in determining the mechanical behaviour of the material and its suitability for an intended purpose. Strain localization may be caused by different mechanisms and takes place over different length scales, from nano- to macro- scale. The most widely known and obvious manifestation of strain localization is ordinary tensile and fatigue testing.

Fatigue crack growth has been a topic of active research for decades. In the 1960s, a major breakthrough took place in which a phenomenological relationship was discovered between fatigue crack growth rate and the change in stress intensity factor through the so-called Paris Law [55, 56]. Several modifications have been proposed to the Paris relationship to account for various phenomena. Most notably Elber's discovery of fatigue crack closure [23, 57]. Elber investigated the effects of plastic strain accumulation left behind the crack tip and its effects on crack growth behaviour.

A number of factors influence strain localizations near a fatigue crack in addition to loading and geometry; these include grain structure, crack path, and thickness. Microstructure plays a key role in fatigue crack initiation and growth. Consequently, measurements of strain at the microstructural level are crucial for understanding fatigue crack behaviour. Accumulated plastic strain fields associated with fatigue crack growth exhibited inhomogeneities at two length scales. At the macroscale, the plastic wake contained high strain regions in the form of asymmetric lobes associated with past crack tip plastic zones (Fig. 1.12). At high magnification, high-resolution DIC measurements revealed inhomogeneities at, and below, the grain scale [58]. Effective strain not only varied from grain to grain, but also within individual grains (Fig. 1.13). Furthermore, strain localizations were observed in slip bands within grains and on twin and grain boundaries. A better understanding of these multiscale heterogeneities could help explain variations in fatigue crack growth rate and crack path and could improve the understanding of fatigue crack closure and fracture in ductile metals. Experimental measurements have the potential to provide quantitative, microstructure-based predictions of fatigue crack behaviour. By studying individual slip system activity [59], it may be possible to identify the specific slip systems and local strain levels associated with crack propagation. Insight into the variability in the crack path, strain fields, and crack growth rates could also be gained by applying the techniques used in a journal paper [18] to fatigue crack growth situations.

The strain localization also has an important role to play in the case of precipitation-strengthened austenitic steels. Though it does not have a direct impact on the mechanical behaviour of the material; however, the foundation of damage evolution relies on strain localization by dislocation slip planarity. It is observed that in the precipitation-strengthened steels, for example, steels having semi-coherent Ω or γ' precipitates, anti-phase boundary formation (APB) takes place because of precipitation cutting by the dislocations. The APB is an entity that separates two domains of the same ordered phase [60, 61]. It results from symmetry breaking that occurs during the ordering processes, which can start at different locations in a disordered lattice. An APB forms when two such regions contact so that they display wrong compositional bonds across the interface as illustrated in Fig. 1.14 [62].

Dislocations with Burgers vectors that are not translation vectors of the ordered superlattice can also create APB's as they move through an ordered phase [60, 63]. This APB results in the inhibition of cross-slip, thus promoting the planar dislocation glide. Because of the inability of the material to cross-slip, the stress accommodation is limited, and the planar slip will result in stress/strain concentration. This stress/strain concentration at the microstructural discontinuities, like inclusions and grain boundary, results in damage formation. Moreover, group motion of the dislocations in the form of twins results in considerable damage generation at the grain boundary, upon impinging. This early damage evolution because of strain localization will result in degradation of the tensile strength of the material.

For some high entropy alloys (HEA), showing similarity with commercial grade precipitation-strengthened Fe–Ni–Cr-based steel, having high slip planarity, microstructural deformation characteristics (planar dislocation slip) significantly affected fatigue crack initiation and crack propagation [64]. The deformation localization associated with dislocation planarity led to multiple crack initiation on the slip planes. The crack propagation mechanism comprises crack formation on slip planes around the main crack tip and subsequent coalescence. Dislocation planarity, which is high in the HEA, has been recognized as a significant factor affecting fatigue crack resistance as it influences various fatigue-related parameters: (1) work hardenability, (2) degree of crack tip stress shielding, and (3) ease of microstructural damage accumulation [65-67]. The first parameter is attributed to dislocation distribution, which means that high dislocation planarity delays self-accommodation of local stress. This effect increases the stored strain energy, which prevents further motion or multiplication of dislocations [68]. The second parameter is associated with the elastic strain field around the nearest dislocation from a crack tip. Because the planar dislocation array provides high back stress, the elastic strain field at the nearest dislocation decreases the effective tensile stress at the crack tip, which delays crack opening [66]. The third parameter is related to the accumulation rate of lattice defects per cycle at a microstructurally local site. Enhanced dislocation planarity prevents dislocation annihilation and localizes accumulation of dislocations or vacancies. Accelerated increase of local damage density alters the ease of crack initiation and fatigue

crack propagation mechanism from Mode I to Mode II types [67, 69]. Thus, HEA with high dislocation planarity exhibits the characteristic behaviour of fatigue resistance.

1.1.4 Effect of hydrogen environment on the strain localization behaviour

Damage evolution in precipitation-strengthened steels, having planar slip behaviour, is highly aggravated due to the presence of hydrogen environment [70]. In particular, many ferritic steels, austenitic steels and Nickel-base alloys exhibit a ductility minimum at a specific temperature not far from room temperature, which is a serious problem for the use of these materials, e.g. for storage media in automotive applications [71-73]. Figure 1.15 shows the relative reduction of area, $\emptyset_{H2}/\emptyset_{He}$, for various austenitic steels tensile tested in helium as well as in hydrogen [73].

If hydrogen leads to failure of a material at an overall strain substantially lower than in the absence of hydrogen, one speaks of hydrogen embrittlement, be the mechanism itself ductile or brittle [74]. The fracture appears localised at grain boundaries (inter-granular fracture), or within grains (trans-granular fracture). Also, “dimple fracture” is reported, where vacancy agglomeration into micro-voids and micro-void agglomeration results in crack opening [75, 76]. The various processes, which might control the kinetics of crack growth in hydrogen gas are illustrated schematically in Fig. 1.16 and are as follows [77]:

1. Transport of the gas to the crack tip
2. Physical adsorption
3. Dissociative chemical adsorption, activated or non-activated
4. Hydrogen entry (absorption)
5. Diffusion of hydrogen in the stress field to the fracture propagation zone
6. Hydrogen trapping at defects and internal interfaces.

Hydrogen in and around dislocations assist an earlier start of the dislocation multiplication. When the strain rate is sufficiently low, hydrogen results in enhanced

mobility of the dislocations. These effects together, increased number of dislocations, decreased line tension and enhanced mobility promote the opening of micro-cracks under lower applied stress, and hence lead to hydrogen embrittlement [78].

The idea of cohesion reduction suggests that segregation of hydrogen to an incipient fracture zone reduces the local atomic bonding at the crack tip, decreasing the crystal's cohesive energy and inducing embrittlement. Experimental confirmation of lattice de-cohesion is given by Barnoush and Vehoff [79, 80], who explained the observed facilitation of dislocation nucleation mentioned above by a reduction of lattice cohesion due to dissolved hydrogen in the lattice. Jiang and Carter [81] performed density functional calculations to obtain ideal fracture energies as a function of hydrogen coverage. They indeed find a substantial reduction of cohesion when planes are covered with hydrogen, as much as 80 %.

To summarise, a complex interplay of different effects playing a role in the modification of physico-mechanical properties by hydrogen. The most prominent effects are: (a) local weakening of interatomic bond strength in steels, leading to de-cohesion and a lowering of the surface energy and, finally, to brittle fracture with and without martensite formation, and (b) local enhancement of dislocation formation and migration rate, leading to ductile fracture.

1.2. Objectives

Precipitation-strengthened steels were developed in order to account for material with superior mechanical properties. Obviously, different applications demand different properties, the desirable property in one case may be a disadvantage in the other case. Some of the most desirable properties are high strength, toughness and ductility. Apart from this, the fatigue limit of precipitation-strengthened steels is less than the predicted fatigue limit, based on empirical equation ($\sigma_w \cong 1.6\,HV$) [28]. Thus, precipitation-strengthened steels are weaker than experimentally predicted fatigue strength. This indicates that the precautions required for designing precipitation-strengthened steels are different from conventional steels. Previous studies focused on the enhancement of strength in precipitation-strengthened steels [82-84], and less consideration was given to its further improvement in order to reach the approximate value of experimental strength. Therefore, it is necessary to consider the factors that are responsible for weakening the strength of precipitation-strengthened steels. Since, strain localization has a direct impact on dislocation-precipitate interaction, I feel that the most crucial factor which is responsible for the deterioration of strength is strain localization [85-87]. Thus this study focuses on the effect of strain localization on the strength of precipitation-strengthened steels. There are many studies in the past in which the mechanical behaviour of the material was discussed taking into the reference of strain localization. Some researchers discussed the evolution of strain localization during crack propagation from the notch. Additional to this, previous studies also discuss discrete strain localization in various microstructural features [58]. The effect of strain localization is also anticipated in the form of plasticity induced crack closure [88]. The difference in crack propagation behaviour is explained with the help of difference in plasticity generated in the wake and ahead of the crack tip [89].

At first, I have considered two specially developed precipitation-strengthened steels which have the same tensile strength and micro-hardness but differ in the nature of precipitates they bear. Moreover, the microstructure of the two steels is also different. This has rendered one steel as more susceptible to strain localization than the other. Thus,

the effect of strain localization on the fatigue limit of two steels is considered for short and long defects.

Secondly, in order to exclusively understand the evolution of damage due to strain localization, commercial precipitation-strengthened steel SUH 660 is considered. This steel has characteristics of slip planarity and shows resistance to cross slip, because of anti-phase boundary formation. The study is carried out to understand the evolution of damage under uniaxial tensile loading due to strain localization. This will develop an understanding of the mechanical behaviour of this steel under miscellaneous conditions. Since this material is also a special material for hydrogen environment, variation in damage evolution behaviour under hydrogen environment is also studied. Based on the understanding developed by carrying out these studies, an attempt is made to understand the damage initiation mechanism and to predict the fatigue limit of this material.

This sums up the overall objective of this study is to explore the effect of strain localization on the mechanical behaviour of precipitation-strengthened steels.

1.3. Thesis outline

This thesis consists of 6 chapters. The chapters are arranged in order to achieve the basic objective of this study. The following paragraphs will give a glimpse of the work content of each chapter:

Chapter 1 will introduce the work done by the previous researchers in the respective field. An overview of the precipitation-strengthening in steels was presented. The basic mechanics of dislocation motion around precipitates is also explained. The effect of arbitrary crack length on the fatigue properties is discussed. The effect of a short and long crack is presented separately. The theories governing the short crack and long crack propagation behaviour is also postulated. This chapter also includes the effect of strain localization on the tensile and fatigue properties of precipitation-strengthened steels. The effect of hydrogen environment on the damage evolution behaviour based on previous findings is reported.

Chapter 2 deals with fatigue crack propagation and fatigue limit properties for two different types of precipitation-strengthened steels. One steel is more susceptible to strain localization than others. Both steels have similar tensile strength and micro-hardness. The fatigue properties are compared for a plain specimen, a specimen with a short crack and long crack. Effect of strain localization on fatigue properties of precipitation-strengthened steel with an arbitrary length crack is discussed with the help of plasticity-induced crack closure. The superiority of the fatigue limit of each precipitation-strengthened steel depends on the initial crack size and the influence of strain localization.

Chapter 3 addresses the damage evolution mechanism in precipitation-strengthened Fe–Ni–Cr-based steel (SUH 660) at ambient temperature in air. Specifically, damage quantification and associated microstructure characterization were performed. The damage initiation sites were inclusion and grain boundaries, impinged by dislocation slip. The early stage of damage evolution was observed before necking of the specimen. Subsequent plastic straining caused damage growth along slip planes and coalescence of damage via localized shear in ligaments between damages, for which the behaviour was associated with the planar character of the slip. The damage evolution behaviour observed in the post-mortem specimen was consistent with fractographic characteristics.

Chapter 4 aims at understanding the change of the hydrogen embrittlement mechanism with respect to the hydrogen content of precipitation-strengthened Fe-Ni-Cr-based steel. Hydrogen was electrochemically introduced with different current densities. The hydrogen-charging deteriorated crack initiation and propagation resistance as well as the crack tip blunting capability. Further, with increasing hydrogen content, the primary cracking sites changed from coarse carbides to slip bands, and then to grain boundaries. Moreover, because the crack initiation probability increased and the resistance to trans-granular crack propagation decreased with hydrogen content, the crack coalescence associated with slip localization occurred more frequently.

Chapter 5 deals with the fatigue characteristics of SUH 660. Crack initiation is the main focus of this study. Microscopic analysis is carried out in order to investigate the crack initiation. It is observed that the crack initiation is mainly at the grain boundaries contrary to inclusions in the case of uniaxial tensile loading. There are multiple crack initiation sites, the initial crack grows and coalescence with the neighbouring crack, which results in the final failure. It is assumed that the $\sqrt{area}$ in this case is the combined area of the observed multiple cracks. This cumulative area will result in the fatigue limit prediction by Murakami's equation.

Chapter 6 summarises the findings of the studies by general conclusions.

1.4. List of published paper during PhD period

Journal papers:

1. Virendra Kumar Verma, Motomichi Koyama, Shigeru Hamada, Eiji Akiyama, Multiple damage mechanisms facilitated by planar dislocation glide in a commercial-grade precipitation-strengthened Fe–Ni–Cr-based steel, Material Science and Engineering: A 2020, 782: 139250.
2. Virendra Kumar Verma, Motomichi Koyama, Shigeru Hamada, Eiji Akiyama, Effects of hydrogen content that alters damage evolution mechanisms in SUH 660 precipitation-strengthened Fe-Cr-Ni steel, Material Science and Engineering: A 2020, 791: 139750.
3. Virendra Kumar Verma, Gopalakrishnan C. K., Shigeru Hamada, Tatsuo Yokoi, Hiroshi Noguchi, Effect of strain localization on fatigue properties of precipitation-strengthened steel with an arbitrarily long crack, International Journal of Fatigue 2020 [Under Review].

Conference papers:

1. Virendra Kumar Verma, Shigeru Hamada, Motomichi Koyama, Understanding the damage initiation mechanism of precipitation-strengthened Fe-Ni-Cr based austenitic steel, Material Today Proceedings 2020.
2. Virendra Kumar Verma, He Liu, Shigeru Hamada, Hiroshi Noguchi, Fatigue crack propagation study of precipitation-strengthened steels, Materials Today Proceedings 2020.
3. Virendra Kumar Verma, He Liu, Shigeru Hamada, Tatsuo Yokoi, Hiroshi Noguchi, Effect of initial crack length on the transition of fatigue properties for precipitation-strengthened steel, JSME M&M 2019.
4. He Liu, Tingshu Chen, Virendra Kumar Verma, Motomichi Koyama, Shigeru Hamada, Hiroshi Noguchi, Similarity between shallow notch and crack effects on structural strength governed by global plastic instability, JSME M&M 2019.

References

[1] A.J. Ardell, Precipitation hardening, Metallurgical Transactions A 16(12) (1985) 2131-2165.

[2] L.M. Clarebrough, M.E. Hargreaves, Work hardening of metals, Progress in Metal Physics 8 (1959) 1-103.

[3] T. Gladman, Precipitation hardening in metals, Materials science and technology 15(1) (1999) 30-36.

[4] A. Kelly, R.B. Nicholson, Precipitation Hardening, Pergamon Press1963.

[5] J.W. Martin, Precipitation Hardening: Theory and Applications, Elsevier Science2012.

[6] P.M. Anderson, J.P. Hirth, J. Lothe, Theory of Dislocations, Cambridge University Press2017.

[7] J. Friedel, Dislocations, Pergamon Press1967.

[8] D. Miannay, P. Costa, D. François, A. Lasalmonie, A.B. Vannes, D. Jeulin, D. Marquis, H. Burlet, F. Vaillant, M. Bornert, Advances in Mechanical Behaviour, Plasticity and Damage, Elsevier Science2000.

[9] D. François, A. Pineau, A. Zaoui, Mechanical Behavior of Materials: Elasticity and plasticity, Kluwer Academic Publishers1998.

[10] E. Orowan, Internal stress in metals and alloys, Faraday society, London, 1948.

[11] G. Lütjering, J. Albrecht, C. Sauer, T. Krull, The influence of soft, precipitate-free zones at grain boundaries in Ti and Al alloys on their fatigue and fracture behavior, Materials Science and Engineering: A 468-470 (2007) 201-209.

[12] Z. Guo, W. Sha, Quantification of Precipitation Hardening and Evolution of Precipitates, MATERIALS TRANSACTIONS 43(6) (2002) 1273-1282.

[13] A. Kelly, M. Fine, The strength of an alloy containing zones, Acta Metallurgica 5(7) (1957) 365-367.

[14] D.J. Edwards, B.N. Singh, S. Tähtinen, Effect of heat treatments on precipitate microstructure and mechanical properties of a CuCrZr alloy, Journal of Nuclear Materials 367-370 (2007) 904-909.

[15] H. Wu, S. Hamada, H. Noguchi, Pre-strain effect on fatigue strength characteristics of SUH660 plain specimens, International Journal of Fatigue 55 (2013) 291-298.

[16] H. Mughrabi, Cyclic Slip Irreversibilities and the Evolution of Fatigue Damage, Metallurgical and Materials Transactions B 40(4) (2009) 431-453.

[17] Y. Murakami, T. Mura, M. Kobayashi, Change of dislocation structures and macroscopic conditions from initial state to fatigue crack nucleation, Basic Questions in Fatigue: Volume I, ASTM International1988.

[18] W. Abuzaid, A. Oral, H. Sehitoglu, J. Lambros, H. Maier, Fatigue crack initiation in Hastelloy X–the role of boundaries, Fatigue & Fracture of Engineering Materials & Structures 36(8) (2013) 809-826.

[19] C. Laird, The application of dislocation concepts in fatigue, Dislocations in solids, North-Holland Amsterdam1983, pp. 55-119.

[20] H. Mughrabi, R. Wang, K. Differt, U. Essmann, Fatigue crack initiation by cyclic slip irreversibilities in high-cycle fatigue, Fatigue mechanisms: advances in quantitative measurement of physical damage, ASTM International1983.

[21] K. Tanaka, T. Mura, A dislocation model for fatigue crack initiation, (1981).

[22] D. Taylor, J. Knott, Fatigue crack propagation behaviour of short cracks; the effect of microstructure, Fatigue & Fracture of Engineering Materials & Structures 4(2) (1981) 147-155.

[23] W. Elber, Fatigue crack closure under cyclic tension, Engineering Fracture Mechanics 2(1) (1970) 37-45.

[24] R. Ritchie, S. Suresh, Some considerations on fatigue crack closure at near-threshold stress intensities due to fracture surface morphology, Metallurgical Transactions A 13(5) (1982) 937-940.

[25] R. Ritchie, S. Suresh, C. Moss, Near-threshold fatigue crack growth in 2 1/4 Cr-1Mo pressure vessel steel in air and hydrogen, (1980).

[26] S. Suresh, R. Ritchie, A geometric model for fatigue crack closure induced by fracture surface roughness, Metallurgical transactions A 13(9) (1982) 1627-1631.

[27] S. Suresh, G. Zamiski, D.R. Ritchie, Oxide-induced crack closure: an explanation for near-threshold corrosion fatigue crack growth behavior, Metallurgical and Materials Transactions A 12(8) (1981) 1435-1443.

[28] M. Yukitaka, Metal fatigue: effects of small defects and nonmetallic inclusions, Elsevier science, Oxford, UK, 2002.

[29] S. Suresh, Fatigue of Materials, 2 ed., Cambridge University Press, Cambridge, 1998.

[30] M. Endo, Y. Murakami, Effects of Hardness and Crack Geometries on ΔK_{th} of Small Cracks Emanating from Small Defects, EGF1, 1986.

[31] H. Kitagawa, S. Takahashi, Fracture mechanical approach to very small fatigue cracks and to the threshold, Trans Jpn Soc Mech Eng 45 (1979) 1289-1303.

[32] H.N. H. Kobayashi, A Stress Criterion for Fatigue Crack Propagation in Metals, Proceedings of 1st International Conference on Mechanical Behaviour of Materials, Kyoto, Japan (1972) 199-208.

[33] B. Leis, A. Hopper, J. Ahmad, D. Broek, M. Kanninen, Critical review of the fatigue growth of short cracks, Engineering Fracture Mechanics 23(5) (1986) 883-898.

[34] J. Kruzic, J. Campbell, R. Ritchie, On the fatigue behavior of γ-based titanium aluminides: role of small cracks, Acta materialia 47(3) (1999) 801-816.

[35] G.R. Romanoski, The fatigue behavior of small cracks in aircraft turbine disk alloys, Massachusetts Institute of Technology, 1990.

[36] Y. Murakami, T. Endo, The effects of small defects on the fatigue strength of hard steels, International conference on fatigue, Materials Experimentation and Design, Warwick University 1981, pp. 431-440.

[37] Y. Murakami, S. Fukuda, T. Endo, Effect of Micro-hole on Fatigue Strength [lst Report, Effect of Micro-hole (Dia.: 40, 50, 80, I00 and 200 pm) on the Fatigue Strength of 0.13% and 0.46% Carbon Steels], Trans. Jpn. Soc. Mech. Eng. Ser. I 44(388) (1978) 4003-4013.

[38] Y. Murakami, K. H., T. Endo, Effect of Micro-hole on Fatigue Strength [IInd Report, Effect of Micro-hole of 40-200 μm in diameter on the Fatigue Strength of quenched or quenched and tempered 0.46% Carbon Steel], Trans. Jpn. Soc. Mech. Eng. A 45(400) (1979) 1479-1486.

[39] W.F. Brown, J.E. Srawley, Plane strain crack toughness testing of high strength metallic materials, American Society for Testing and Materials1967.

[40] ASTM E647-15e1, Standard Test Method for Measurement of Fatigue Crack Growth Rates, ASTM International, West Conshohocken, 2015.

[41] STP 410 E8, Plane Strain Crack Toughness Testing of High Strength Metallic Materials, ASTM International, West Conshohocken, PA, 1966.

[42] ASTM E399-20, Standard Test Method for Linear-Elastic Plane-Strain Fracture Toughness of Metallic Materials, ASTM International, West Conshohocken, PA, 2020.

[43] J.R. Rice, A Path Independent Integral and the Approximate Analysis of Strain Concentration by Notches and Cracks, Journal of Applied Mechanics 35(2) (1968) 379-386.

[44] S. Pearson, Initiation of fatigue cracks in commercial aluminium alloys and the subsequent propagation of very short cracks, Engineering Fracture Mechanics 7(2) (1975) 235-247.

[45] J. Lankford, THE GROWTH OF SMALL FATIGUE CRACKS IN 7075–T6 ALUMINUM, Fatigue & Fracture of Engineering Materials & Structures 5(3) (1982) 233-248.

[46] M. Brochu, Comportement en fatigue de l'aluminium 357 coulé par gravité et rhéocoulé, École Polytechnique de Montréal, 2010.

[47] K. Gall, G. Biallas, H.J. Maier, M.F. Horstemeyer, D.L. McDowell, Environmentally influenced microstructurally small fatigue crack growth in cast magnesium, Materials Science and Engineering: A 396(1) (2005) 143-154.

[48] P. Hobson, M. Brown, E. de Los Rios, Two phases of short crack growth in a medium carbon steel, EGF1, 1986.

[49] A. Navarro, E.R. de los Rios, Short and long fatigue crack growth: A unified model, Philosophical Magazine A 57(1) (1988) 15-36.

[50] C. Vallellano, A. Navarro, J. Domínguez, Two-parameter fatigue crack growth driving force: Successive blocking of the monotonic and cyclic plastic zones at microstructural barriers, International Journal of Fatigue 46 (2013) 27-34.

[51] C. Vallellano, J. VÁZquez, A. Navarro, J. DomÍNguez, A micromechanical model for small fatigue crack growth: an approach based on two threshold conditions, Fatigue & Fracture of Engineering Materials & Structures 32(6) (2009) 515-524.

[52] P. Paris, F. Erdogan, A critical analysis of crack propagation laws, Journal of Basic Engineering 85 (4) (1963) 528-534.

[53] S. Hamada, T. Kinoshita, K. Morishige, K. Hayashi, T. Ishina, H. Noguchi, Engineering definitions of small crack and long crack at fatigue limit under tensile mean stress and a prediction method for determining the fatigue limit of a cracked Mg alloy, International Journal of Fatigue 56 (2013) 86-94.

[54] J.R. Rice, Mechanics of Crack Tip Deformation and Extension by Fatigue, in: J. Grosskreutz (Ed.), ASTM International, West Conshohocken, PA, 1967, pp. 247-311.

[55] P. Paris, F. Erdogan, A critical analysis of crack propagation laws, (1963).

[56] A. McEvily Jr, R. Boettner, On fatigue crack propagation in FCC metals, Acta Metallurgica 11(7) (1963) 725-743.

[57] W. Elber, The significance of fatigue crack closure, Damage tolerance in aircraft structures, ASTM International1971.

[58] J.D. Carroll, W. Abuzaid, J. Lambros, H. Sehitoglu, High resolution digital image correlation measurements of strain accumulation in fatigue crack growth, International Journal of Fatigue 57 (2013) 140-150.

[59] W.Z. Abuzaid, M.D. Sangid, J.D. Carroll, H. Sehitoglu, J. Lambros, Slip transfer and plastic strain accumulation across grain boundaries in Hastelloy X, Journal of the Mechanics and Physics of Solids 60(6) (2012) 1201-1220.

[60] M.J. Marcinkowski, Electron microscopy and strength of crystals, Interscience Publishers, New York, 1963) p 401 (1963).

[61] R. Kikuchi, J.W. Cahn, Theory of interphase and antiphase boundaries in f.c.c. alloys, Acta Metallurgica 27(8) (1979) 1337-1353.

[62] P. Haasen, J.M. Galligan, Physical Metallurgy, Physics Today 31 (1978) 51.

[63] J.M. Howe, 14 - Structure, Composition and Energy of Solid–Solid Interfaces, in: D.E. Laughlin, K. Hono (Eds.), Physical Metallurgy (Fifth Edition), Elsevier, Oxford, 2014, pp. 1317-1451.

[64] K. Suzuki, M. Koyama, S. Hamada, K. Tsuzaki, H. Noguchi, Planar slip-driven fatigue crack initiation and propagation in an equiatomic CrMnFeCoNi high-entropy alloy, International Journal of Fatigue 133 (2020) 105418.

[65] M. Ojima, Y. Adachi, Y. Tomota, K. Ikeda, T. Kamiyama, Y. Katada, Work hardening mechanism in high nitrogen austenitic steel studied by in situ neutron diffraction and in situ electron backscattering diffraction, Materials Science and Engineering A 527(1-2) (2009) 16-24.

[66] K. Habib, M. Koyama, T. Tsuchiyama, H. Noguchi, Visualization of dislocations through electron channeling contrast imaging at fatigue crack tip, interacting with pre-existing dislocations, Materials Research Letters 6(1) (2018) 61-66.

[67] K. Tanaka, T. Mura, Fatigue crack growth along planar slip bands, Acta Metallurgica 32(10) (1984) 1731-1740.

[68] D.C. Ludwigson, Modified stress-strain relation for FCC metals and alloys, Metallurgical Transactions 2(10) (1971) 2825-2828.

[69] T. Shikama, S. Yoshihara, T. Aiura, D. Lee, H. Noguchi, Initiation and Propagation Behaviors of Fatigue Cracks in 5056 Aluminum Alloy Studied by Rotating-Bending Tests with Smooth Specimen, Journal of Solid Mechanics and Materials Engineering 6(5) (2012) 361-373.

[70] M. Louthan Jr, G. Caskey Jr, J. Donovan, D. Rawl Jr, Hydrogen embrittlement of metals, Materials Science and Engineering 10 (1972) 357-368.

[71] E. Riecke, Effects of Hydrogen in Iron and Steel, Arch Eisenhuettenwes 49(11) (1978) 509-520.

[72] W. Hofmann, W. Rauls, Weld. Res, Supplement (1965) 225.

[73] S. Fukuyama, D. Sun, L. Zhang, M. Wen, K. Yokogawa, Effect of Temperature on Hydrogen Environment Embrittlement of Type 316 Series Austenitic Stainless Seels at Low Temperatures, Nippon Kinzoku Gakkaishi/Journal of the Japan Institute of Metals 67(9) (2003) 456-459.

[74] C. Beachem, A new model for hydrogen-assisted cracking (hydrogen "embrittlement"), Metallurgical and Materials Transactions B 3(2) (1972) 441-455.

[75] I.M. Robertson, P. Sofronis, A. Nagao, M. Martin, S. Wang, D. Gross, K. Nygren, Hydrogen embrittlement understood, Metallurgical and Materials Transactions A 46(6) (2015) 2323-2341.

[76] C. Borchers, T. Michler, A. Pundt, Effect of Hydrogen on the Mechanical Properties of Stainless Steels, Advanced Engineering Materials 10(1-2) (2008) 11-23.

[77] H. Vehoff, Hydrogen related material problems, in: H. Wipf (Ed.), Hydrogen in Metals III: Properties and Applications, Springer Berlin Heidelberg, Berlin, Heidelberg, 1997, pp. 215-278.

[78] R. Oriani, Hydrogen embrittlement of steels, Annual review of materials science 8(1) (1978) 327-357.

[79] A. Barnoush, H. Vehoff, In situ electrochemical nanoindentation of a nickel (111) single crystal: Hydrogen effect on pop-in behaviour, International Journal of Materials Research 97(9) (2006) 1224-1229.

[80] P. Sofroni, I.M. Robertson, Transmission electron microscopy observations and micromechanical/continuum models for the effect of hydrogen on the mechanical behaviour of metals, Philosophical Magazine A: Physics of Condensed Matter, Structure, Defects and Mechanical Properties 82(17-18) (2002) 3405-3413.

[81] D. Jiang, E.A. Carter, First principles assessment of ideal fracture energies of materials with mobile impurities: implications for hydrogen embrittlement of metals, Acta materialia 52(16) (2004) 4801-4807.

[82] M. Gholami, J. Vesely, I. Altenberger, H.-A. Kuhn, M. Wollmann, M. Janecek, L. Wagner, Influence of grain size and precipitation hardening on high cycle fatigue performance of CuNiSi alloys, Materials Science and Engineering: A 684 (2017) 524-533.

[83] J.-H. Wu, C.-K. Lin, Tensile and fatigue properties of 17-4 PH stainless steel at high temperatures, Metallurgical and Materials Transactions A 33(6) (2002) 1715-1724.

[84] N. Bekheet, R. Gadelrab, M. Salah, A. Abd El-Azim, The effects of aging on the hardness and fatigue behavior of 2024 Al alloy/SiC composites, Materials & design 23(2) (2002) 153-159.

[85] C. Déprés, C. Robertson, M. Fivel, Crack initiation in fatigue: experiments and three-dimensional dislocation simulations, Materials Science and Engineering: A 387 (2004) 288-291.

[86] R. Jiang, F. Pierron, S. Octaviani, P. Reed, Characterisation of strain localisation processes during fatigue crack initiation and early crack propagation by SEM-DIC in an advanced disc alloy, Materials Science and Engineering: A 699 (2017) 128-144.

[87] W.Z. Abuzaid, H. Sehitoglu, J. Lambros, Localisation of plastic strain at the microstructurlal level in Hastelloy X subjected to monotonic, fatigue, and creep loading: the role of grain boundaries and slip transmission, Materials at High Temperatures 33(4-5) (2016) 384-400.

[88] P. Chowdhury, H. Sehitoglu, Mechanisms of fatigue crack growth – a critical digest of theoretical developments, Fatigue & Fracture of Engineering Materials & Structures 39(6) (2016) 652-674.

[89] R. Pippan, A. Hohenwarter, Fatigue crack closure: a review of the physical phenomena, Fatigue & Fracture of Engineering Materials & Structures 40(4) (2017) 471-495.

[90] A.J.E. Foreman, M.J. Makin, Dislocation movement through random arrays of obstacles, The Philosophical Magazine: A Journal of Theoretical Experimental and Applied Physics 14(131) (1966) 911-924.

[91] R.O. Ritchie, Influence of microstructure on near-threshold fatigue-crack propagation in ultra-high strength steel, Metal Science 11(8-9) (1977) 368-381.

[92] A.M. García, H. Sehitoglu, Contact of crack surfaces during fatigue: Part 1. Formulation of the model, Metallurgical and Materials Transactions A 28(11) (1997) 2263.

[93] H. Sehitoglu, A.M. García, Contact of crack surfaces during fatigue: Part 2. Simulations, Metallurgical and Materials Transactions A 28(11) (1997) 2277-2289.

[94] B. Li, M. Koyama, S. Hamada, H. Noguchi, Effect analysis of stress-intensity-factor-range decreasing rate for obtaining threshold stress-intensity-factor-range, Theoretical and Applied Fracture Mechanics 104 (2019) 102377.

List of tables and figures

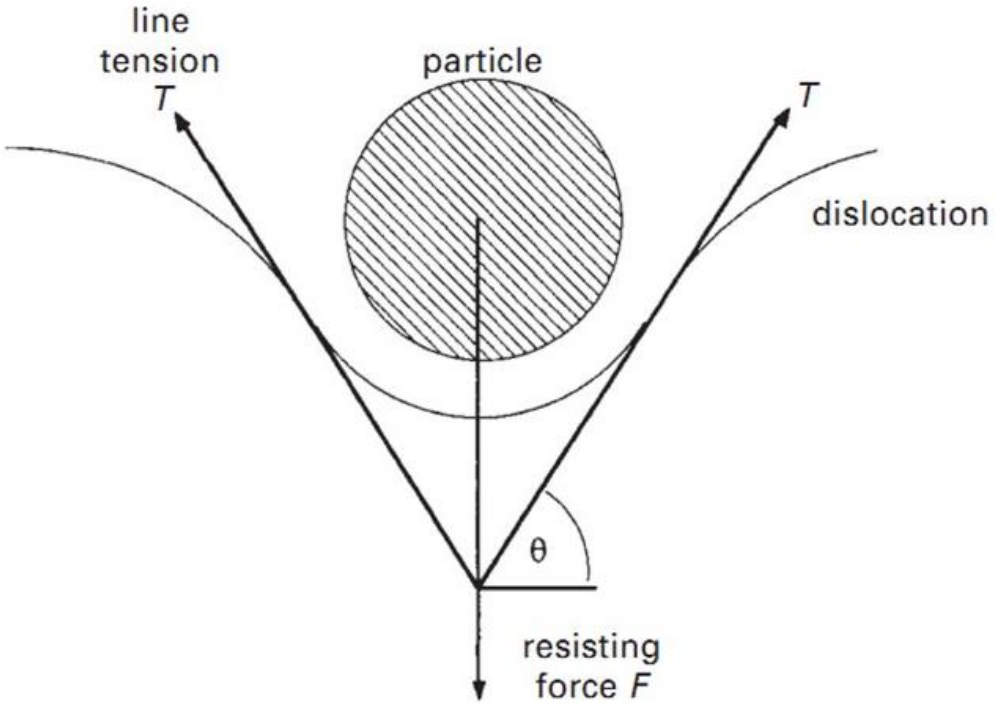

Fig. 1.1. Forces acting during particle-dislocation interaction [10].

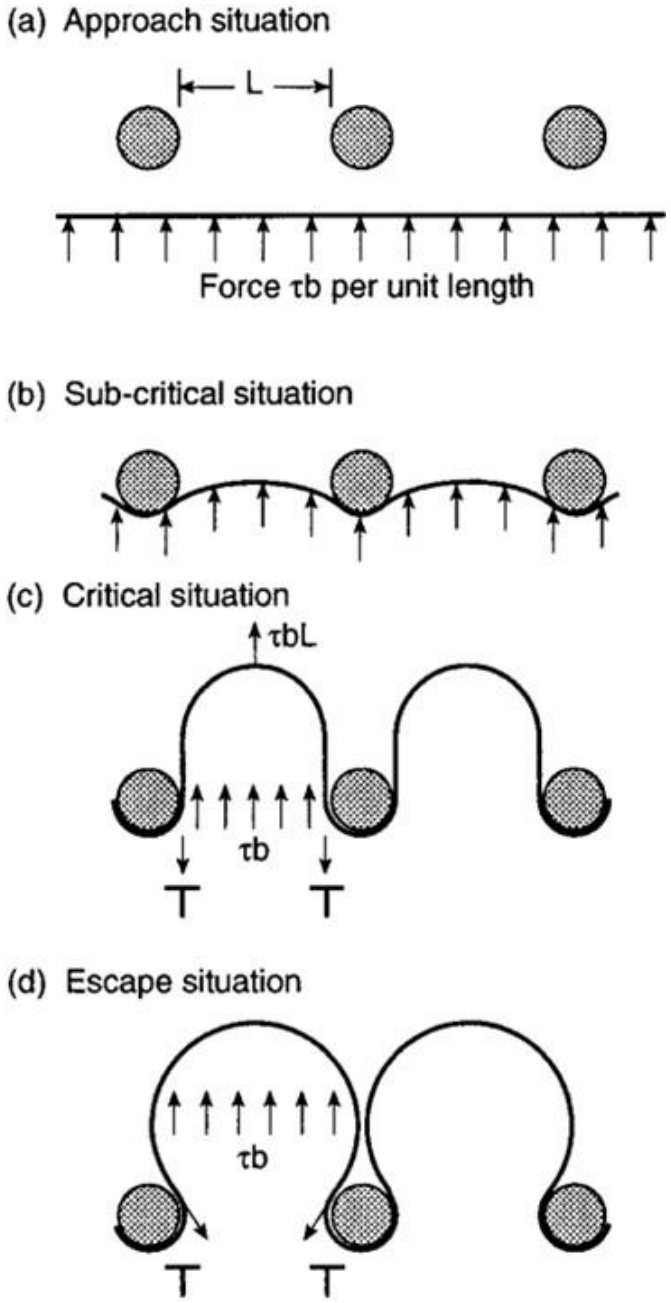

Fig. 1.2. Dislocation interaction with hard undeformable second phase particle: dislocation may pass by Orowan looping or by cross-slip [10].

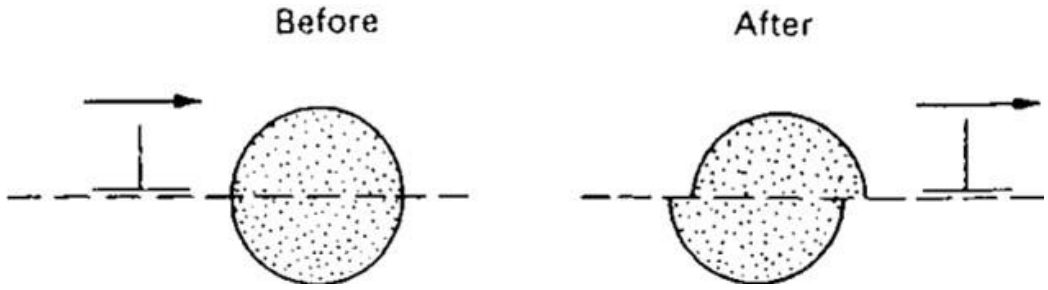

Fig. 1.3. Dislocation passing through particle by shearing (particle cutting) [90].

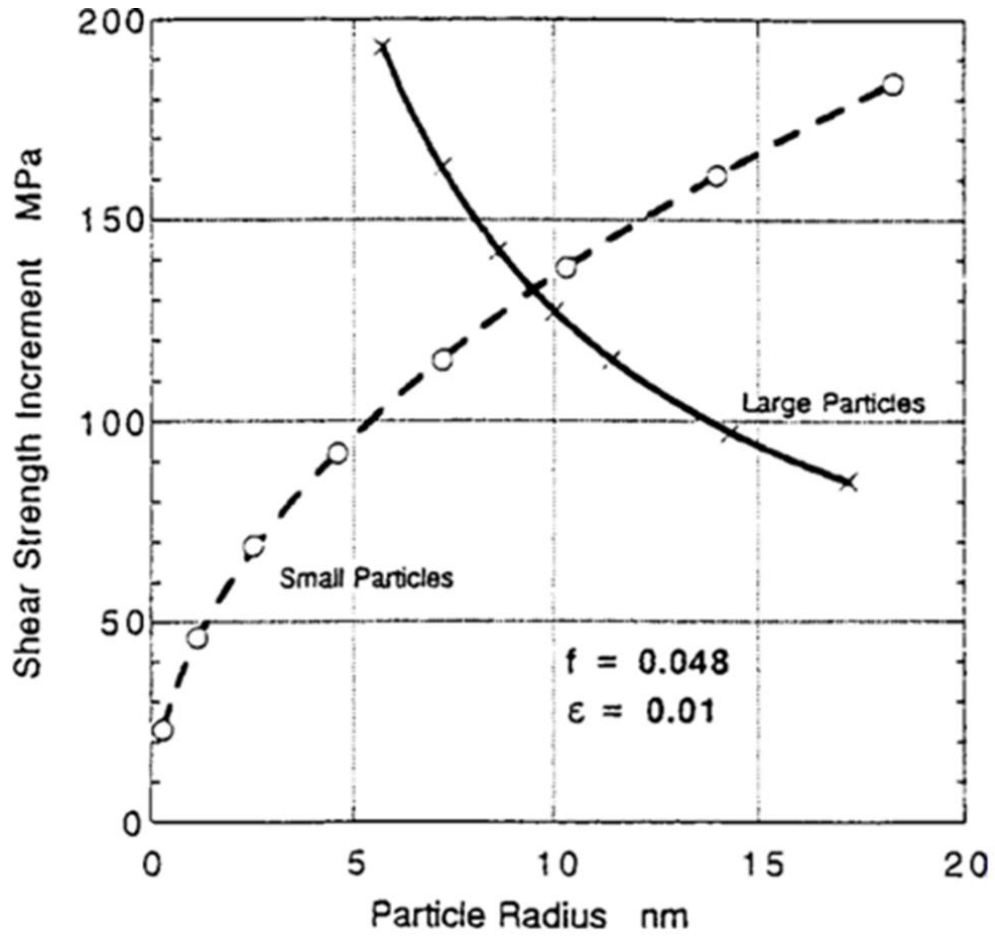

Fig. 1.4. Strain hardening dependency on particle size [13].

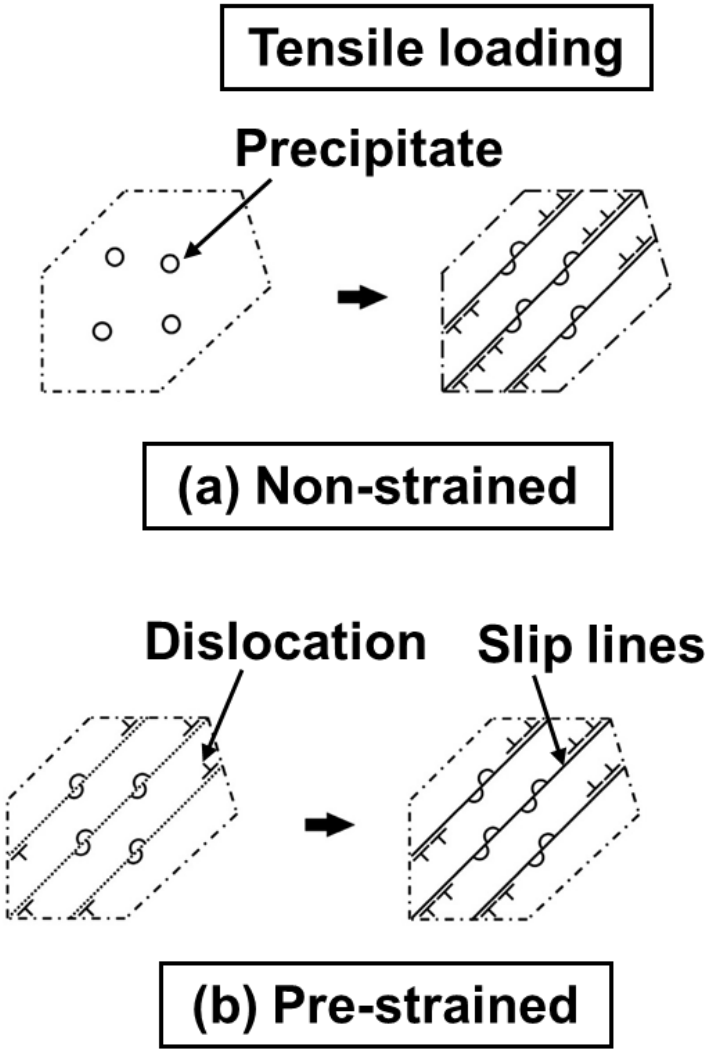

Fig. 1.5. Dislocation-precipitation interaction in tensile loading condition (a) non-strained, (b) pre-strained [15].

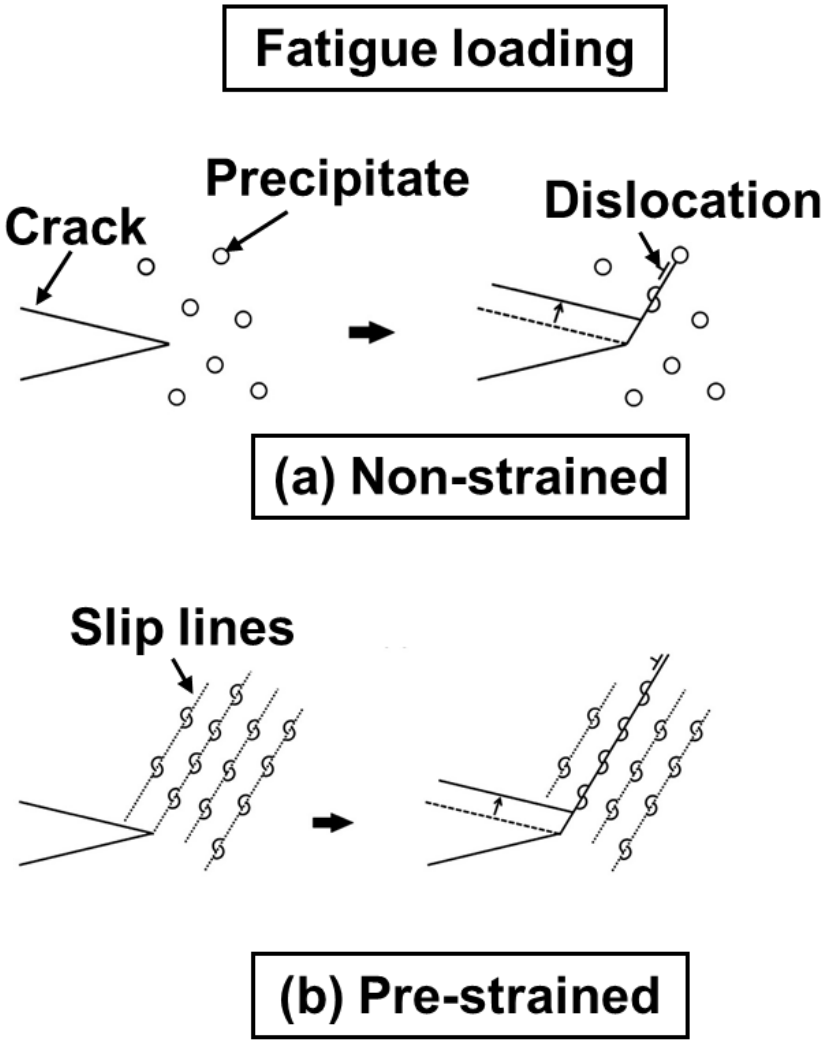

Fig. 1.6. Dislocation-precipitation interaction in fatigue loading condition (a) non-strained, (b) pre-strained [15].

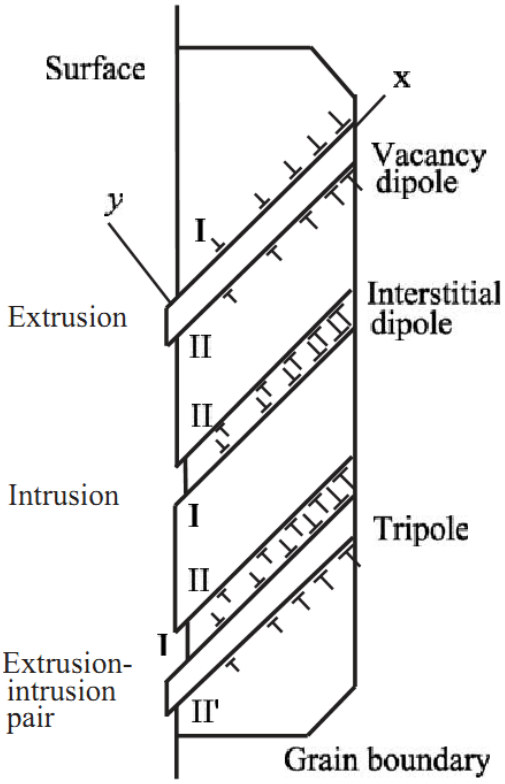

Fig. 1.7. Fatigue crack initiation model, extrusion and intrusion [21].

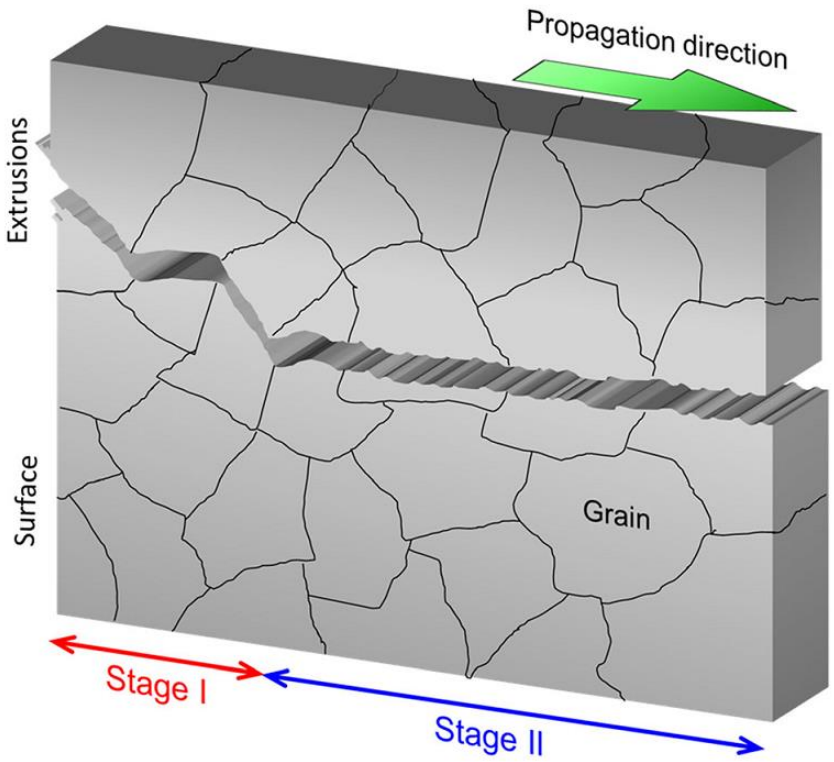

Fig. 1.8. Turtuous stage I (microstructure-sensitive) and straight stage II (microstructure-independent) fatigue crack growth [91].

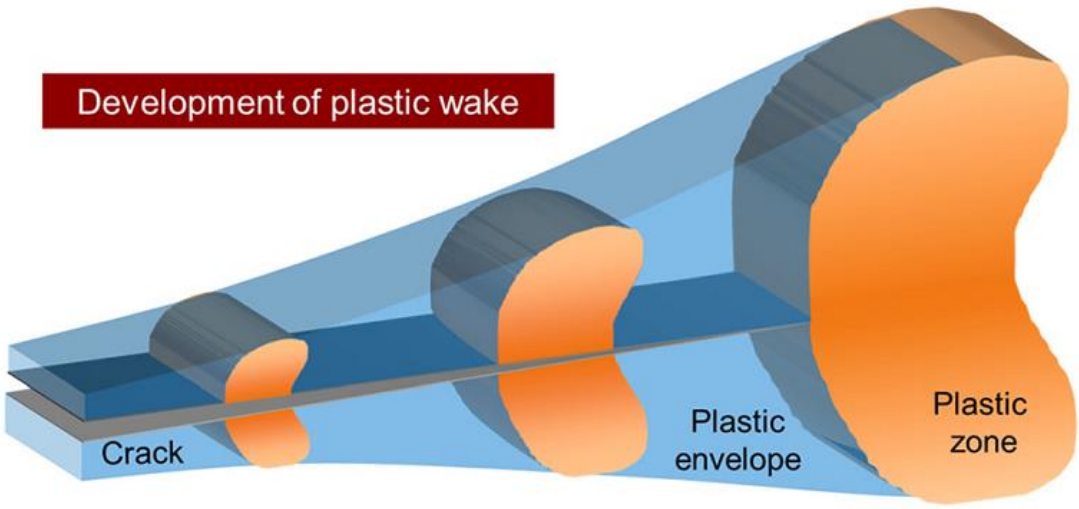

Fig. 1.9. Development of a plastic envelope in the wake of the progressing crack due to the ever-enlarging plastic zone first conceptualized by Elber [23].

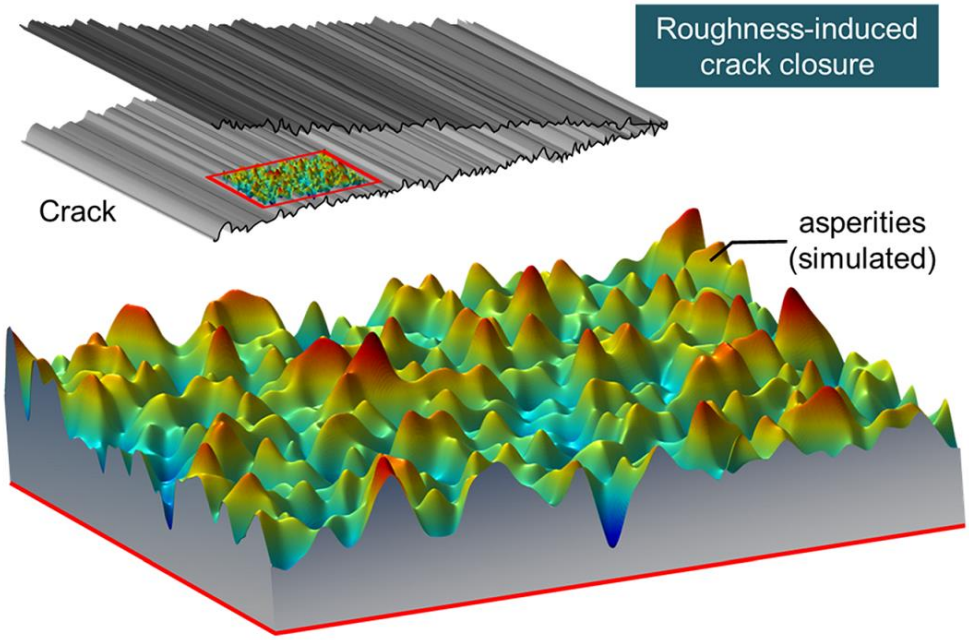

Fig. 1.10. Garcia and Sehitoglu [92, 93] modelled roughness-induced crack closure as a contact problem with random distribution of surface asperities.

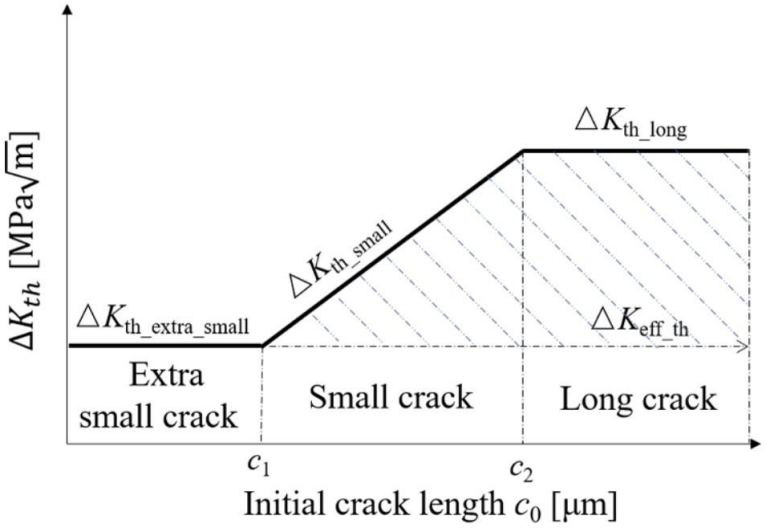

Fig. 1.11. Schematic of initial crack length dependence of threshold stress intensity factor range [94].

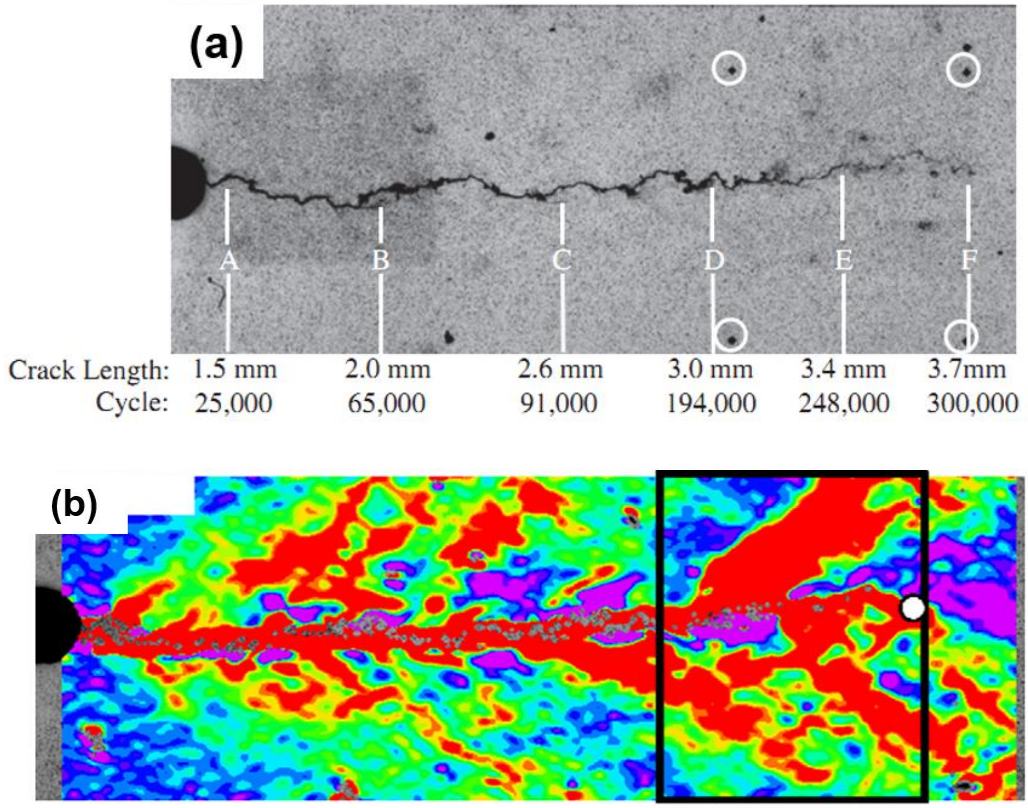

Fig. 1.12. (a) optical image showing crack propagation from an artificial notch (b) DIC image showing the accumulated plastic strain, ε_{yy}, for the instance when crack length 3.7 mm [58].

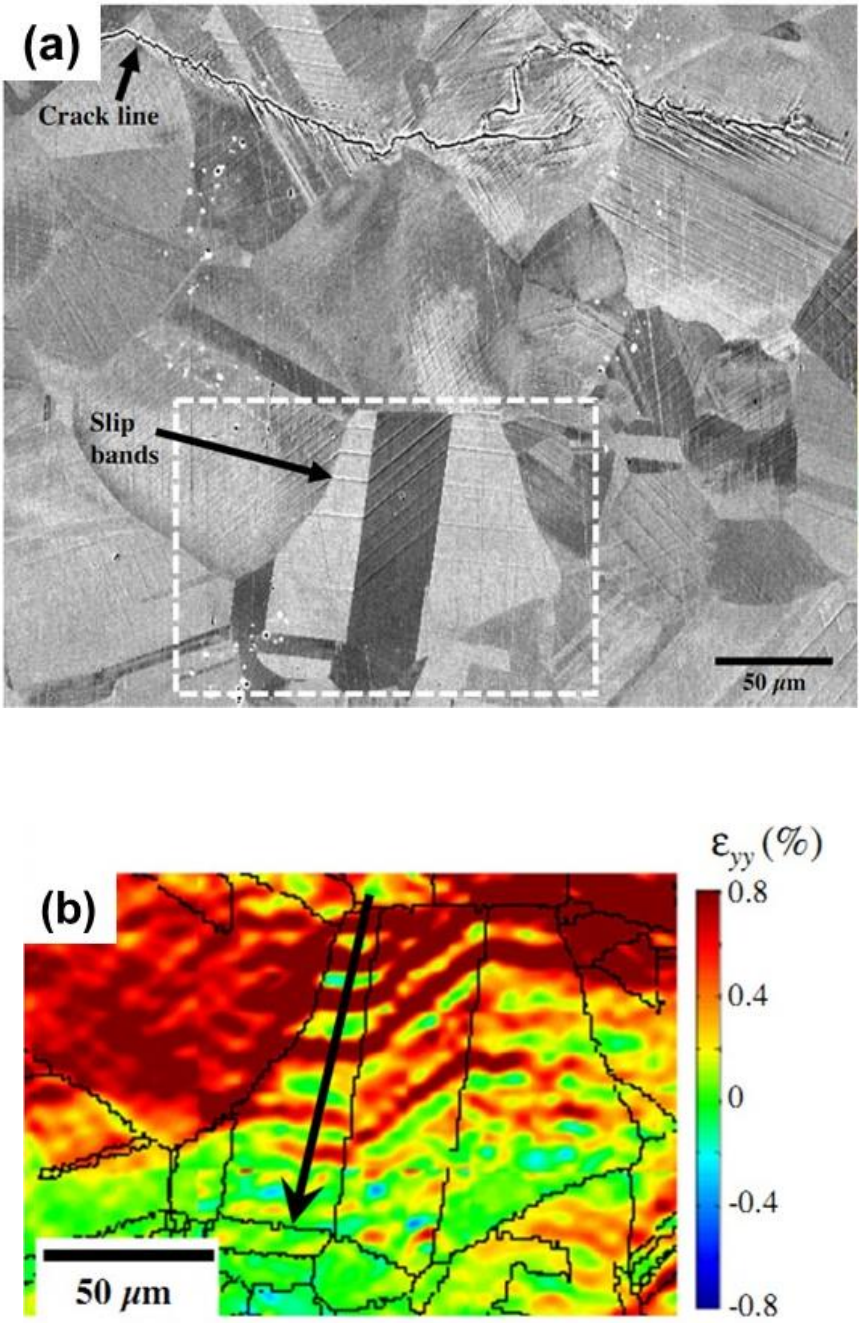

Fig. 1.13. (a) Micrograph showing slip band within grains (b) Strain map, ε_{yy}, of the area shown by white box in (a) [58].

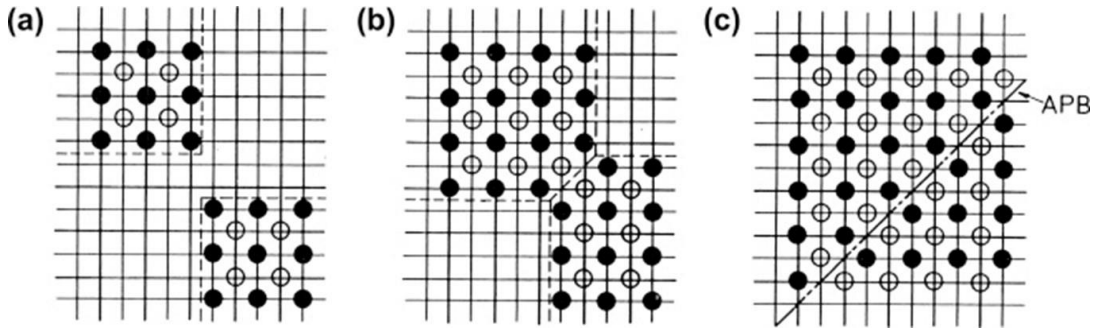

Fig. 1.14. Formation of an APB when ordered regions in which A (open circles) and B (filled circles) atoms occupying different sublattices grow together: (a) nucleation of ordered domains on different sublattices, (b) contact of domains, and (c) the resulting APB (dashed line) [62].

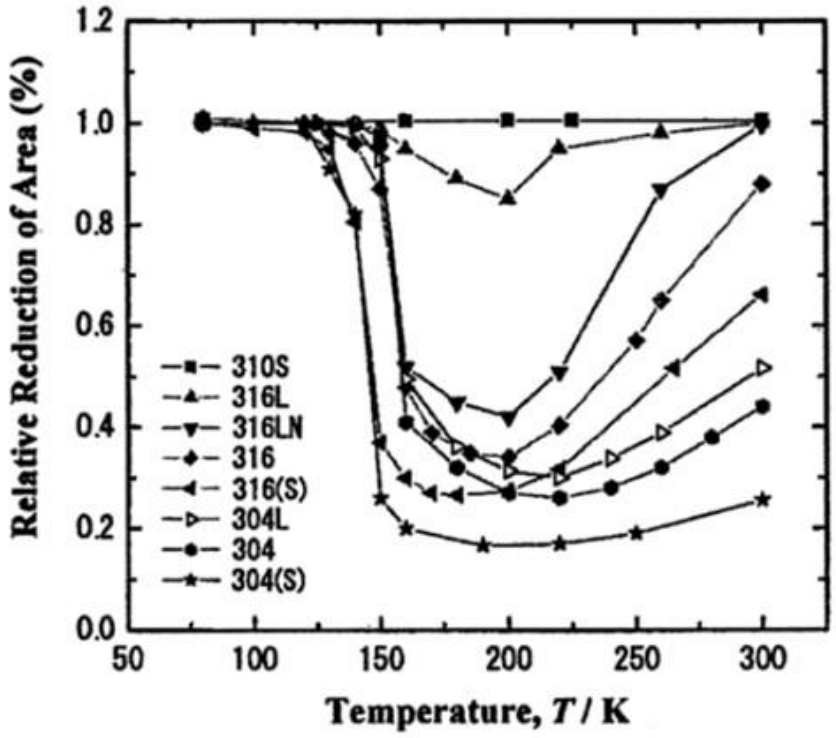

Fig. 1.15. Relative reduction of area ($\emptyset_{H2}/\emptyset_{He}$) for various austenitic stainless steels tensile tested at 10 bar [73].

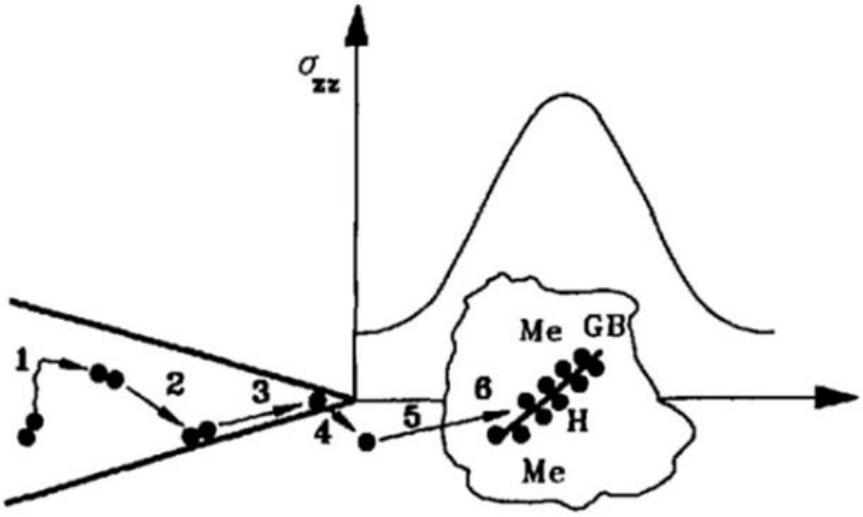

Fig. 1.16. Schematic showing steps for transportation of hydrogen to the fracture propagation zone [77].

Chapter 2 Effect of strain localization on fatigue properties of precipitation-strengthened steel with an arbitrary length crack

2.1. Introduction

The precipitation-strengthened steels developed to match the service requirements have desirable characteristics of high strength and ductility. They also show considerable precipitation and work hardening [1]. They resemble high strength and low alloy steel (HSLA) in their characteristic behaviour [2, 3]. This type of steel is a potential candidate to replace the hot rolled low carbon steel (HRLC), where additional strength and weight reduction are required [4-6].

Precipitation-strengthened steels have high static strength properties, but attention is necessary when they are used for members subjected to fatigue loading [7, 8]. In general, high strength steels are very sensitive to small defects that give rise to stress concentration [9-11]. During fatigue loading, even very small flaws and non-metallic inclusions can give rise to crack initiation and leads to a fatal failure [12, 13]. In modern times the size of an inherent defect in steels is controlled during the production process itself [14, 15]. Therefore, in that case, the defects that may arise during handling and service period is of great importance. For some precipitation-strengthened steels, when the fatigue test is carried out on plain specimen, several flat fracture regions are observed under scanning electron microscope. In other words, a flat fracture region is the origin of crack and leads to final failure [16, 17]. Although there is no clear explanation for the formation of the flat fracture surface, Wu et al. [16] proposed that it might be due to strain localization caused by the cutting of precipitates. Since the flat fracture surface leading to this fatigue failure is caused by the strain localization, it is likely to occur more easily if there is a stress concentration source that causes stress and strain concentration.

Therefore, in this chapter, the effect on the fatigue property of precipitation-strengthened steel is examined using steels that have difference in their affinity for strain localization. The precipitate is generally harder than base-metal, and the strain is localized by cutting precipitates [18, 19], and as a result, it is believed that the strain localization is high in fatigue. Since the Cu-precipitate is soft and its strengthening mechanism [11][20] differs from that of the hard precipitate, the strain will not be localized [21]. The influence of strain localization on the fatigue strength will be clarified through the comparison of the results of two kinds of these precipitation-hardening steel [22, 23]. The steels used for comparison are two precipitation-strengthened steel with the same tensile strength. The tensile strength is around 590 MPa. To improve the stress-strain characteristics in two materials, solid solution hardening and grain size hardening are utilized. One is strengthened by TiC precipitates (T6), and the other is strengthened by Cu precipitates (C6). Since T6 bear hard precipitate and C6 bear soft precipitate, a strain localization can be expected in the case of T6. However, hardness of precipitate is not the only parameter to decide strain localization, it may be due to non-uniform distribution of TiC precipitates in the metal. Thus, strain localization in T6 needs to be confirmed. In our previous study [24], T6 exhibited serration during tensile testing, which signifies strain localization.

In the present study, we have noticed the initial crack length dependence, i.e., the defect size dependence of the fatigue limit characteristics in these materials. In general, the fatigue limit of materials decreases with an increase in defect size [25, 26]. Crack is being categorized as short or long, depending on their dimensions. Previous researchers [27] categorized short cracks as microstructurally, mechanically, and physically short cracks. The criterion for designating a crack as a short or a long crack was proposed by previous studies [28-30] and is based on small scale yielding (SSY).

Furthermore, the fatigue limit characteristics in the small defect region depend on the hardness of the material [28, 31]. The fatigue limit of two materials with different hardness is considered by dividing it into three regions of superiority and inferiority i.e. in the smooth material, in the short crack region, and in the long crack region. Non-propagation cracks are caused by the competition between the driving and deterrent forces of the crack growth [32, 33]. The former is a deformation due to slip originated from the crack tip, and the latter is a crack closure due to the plastic strain region formed by

slippage and remained in the crack wake [27, 34]. The difference between short and long crack regions can be expressed as whether the SSY condition is satisfied or not [35, 36], and the ratio of the size of the plastic region to the crack length of each region is different. For the same load, the shape of the plastic region formed is considered to be different between materials that are susceptible to strain localization and those that are not. The effect of plastic regions with different shapes on crack growth and non-propagation may be different when the plastic region size is large or small relative to the crack length [37-39]. Therefore, I considered that the superiority and inferiority in each region did not follow a fixed trend when the material with high strain localization was compared with the material without it.

Then, the tensile test and hardness test are carried out first, and each static characteristic is grasped. After that, for strain localization, the plastic strain near the notch was confirmed by using the Digital Image Correlation (DIC) method [40, 41]. Then, the fatigue test for a plain, with a short crack and with a long crack specimen are carried out. By the fatigue test, fatigue crack propagation characteristics and fatigue limit characteristics of each material are obtained and examined.

2.2 Experimental procedure

2.2.1. Material

The precipitation-strengthened steels used for the present study are C6 and T6. The chemical composition of C6 and T6 (Table 2.1) shows the presence of Cu and TiC precipitates, respectively. The microstructure observation studies done hereafter (section 2.3.1) reveals the microstructural details of these materials.

The material used for this chapter is processed as follows:

C6: A 300 or 150 kg material was melted in a vacuum melting furnace and cast into 50 kg flat ingots (200 mm wide × 90 mm long × 325 mm high). After heating at solutionizing temperature of 1250°C for 60 min, these flat ingots were rolled into thick bars (220 mm wide × 250 mm long × 35 mm high) at temperatures higher than 1050°C. Subsequently, they were cut into three parts and rolled again at a temperature above Ar3

temperature after heating at 1250°C for 60 min. The coiling temperature of C6 was set to 550°C, which was the nose temperature of Cu precipitates in ferrite. After rolling, the plates with a size of 220 mm wide ×1500 mm long ×6 mm high were divided into two parts, and the specimens for tensile and fatigue tests were cut from these plates.

T6: The procedure followed for T6 was exactly the same as C6, except in the case of T6, the coiling temperature was set to 600°C, which is the nose temperature of TiC precipitates in ferrite. After rolling, the plates were air-cooled to 730°C to accelerate the separation of ferrite and austenite. Subsequently, they were cooled to room temperature to transform the austenite into martensite.

2.2.2. Specimen design

Tensile specimen geometry having a thickness 1 mm is shown in Fig. 2.1. Two fatigue specimen designs were selected each for rotating- bending (short crack) and tension-compression (long crack) fatigue test. The main emphasis was on carrying out the rotating - bending fatigue tests only, but since the long artificial defect design exceeds the limited dimensions of specimen for rotating- bending test, we had to opt for a new specimen design for a long artificial defect. The two designs of the specimen with short artificial defect (thickness 1 mm) and specimen with a long artificial defect (thickness 5 mm) are shown in Fig. 2.2 and Fig. 2.3 respectively. Figures 2.2 and 2.3 also show the artificial defect geometry [28-30]. The artificial defects were introduced by various diameter micro-drills. The specimen with the short artificial defect was tested on a rotating-bending fatigue testing machine, and the specimen with the long artificial defect was tested on the tension-compression fatigue testing machine. The specimen for the rotating-bending test was mounted on the surface of a jig subjected to cyclic rotating-bending thus applying cyclic tension-compression load to the specimen. Details of the test are shown elsewhere [42].

2.2.3. Designed stress amplitude and artificial defect geometry

Previous researchers [28-30] have suggested the transition from a short to a long crack region. The relative nature of a crack to be short or long depends on the stress amplitude, therefore it follows the following equation [43]:

$$\frac{\sigma_{\infty,\max}}{\sigma_Y} \leq 0.5 \sim 0.6 \quad \text{(for long crack, small scale yielding)} \tag{2.1}$$

where $\sigma_{\infty,\max}$ is maximum remote stress during the loading cycle, and σ_Y is yield strength.

Calculation from this equation yields the limiting stress amplitude for which crack can be considered as short or long. Thus, a stress amplitude ≥ 312 MPa corresponds to a short crack, and a stress amplitude ≤ 250 MPa corresponds to a long crack. The stress amplitude value was chosen to have a contrast between the stress amplitude for a short and a long crack. The stress amplitude decided for a short crack is 350 MPa, and the stress amplitude for a long crack is 200 MPa. The corresponding $\sqrt{area}$ calculation leads to the result that $\sqrt{area}$ ≥ 1000 μm results in a long crack condition, and $\sqrt{area}$ ≤ 1000 μm will satisfy the short crack condition [28]. Therefore, the design of the artificial defect was chosen to have a clear demarcation between the short and a long crack. The designed artificial defect size ($\sqrt{area}$) (Figs. 2.2(b) and 2.3(b)) for a short crack, and a long crack is 125 μm and 1253 μm respectively.

2.2.4 Experimental methodology

2.2.4.1. Microstructure observation

In order to understand the basic microstructure of the two materials used in the present study, we undertook microstructure observation studies. The part of the material was sliced and polished with the help of 240, 400, and 1200 grade emery sheets and then mirror polished with the help of colloidal silica. The polished material was then etched with the etchant. The etchant used here is Nital reagent (100 ml ethanol and 6 ml HNO_3). The etched surface was then observed under a digital microscope (VHX – 900F, Keyence, Japan).

2.2.4.2. Tensile test

The tensile test was performed to have an overview of material tensile properties like yielding, tensile strength and elongation. The tensile specimen was fabricated in Electric Discharge Machine (EDM). The specimen was then polished to mirror finish following the same procedure as before. The tensile test was carried on a tensile testing machine (AGS – X, Shimadzu, Japan) with a strain rate of 10^{-3} s^{-1} at room temperature (296 K).

2.2.4.3. Hardness test

The polished specimen was tested for Vickers hardness (HMV – G series, Shimadzu, Japan). As suggested by Murakami's equation [28], Vickers hardness has a direct relation with the fatigue limit. Therefore, it is an important parameter to access material fatigue behaviour. The load used for measuring hardness was 4.9 N. The indentation time was 20 s.

2.2.4.4. DIC analysis

DIC analysis was carried on the central notched specimen. The specimen for DIC analysis has a central hole with a slit on either side of the hole. DIC specimen was polished to mirror finish with the emery sheets (240, 400, 1200 grade) and subsequently with colloidal silica. The specimen was painted with white enamel paint, and a speckle pattern was made on the white background with the help of black spray. DIC test was performed on the tensile testing machine with a strain rate of 10^{-3} s^{-1} at room temperature (296 K). The pixel changes in this pattern were measured to get the strain data. DIC images were analyzed in commercial software (VIC- 2D, 2009, Correlated solutions).

2.2.4.5. Fatigue test

Fatigue specimens were fabricated (in EDM) and polished to mirror finish in the same way as tensile specimens. The artificial defect was then fabricated in the specimen, and the specimen is again polished to remove any burrs. The polished specimen was then tested in the fatigue testing machine. During the fatigue test, the machine was stopped after a predetermined number of cycles, then the crack growth was monitored using the replica (cellulose acetate film) technique [44] and with the help of an optical microscope (VHX – 900F, Keyence, Japan). The rotating- bending test was done on Ono – type

rotating bending fatigue testing machine at room temperature (296 K) (stress ratio $R = -1$ and frequency $f = 30$ Hz) and tension-compression test was done on servo– pulser fatigue testing machine (EHF – E series, Shimadzu, Japan) at room temperature (296 K) ($R = -1$ and $f = 30$ Hz).

2.3 Results

2.3.1. Microstructure observation

Figures 2.4(a) and (b) shows the underlying microstructure for C6 and T6, respectively [24]. The microstructure of C6 has a ferrite matrix structure with Cu precipitates. The microstructure of T6 has a ferrite matrix with TiC precipitates and pearlite content. C6 has a coarse grain structure, whereas T6 has a fine grain structure.

2.3.2. Tensile and hardness test

Figure 2.5 shows the stress-strain curve for C6 and T6. The tensile test result shows that the ultimate tensile strength (UTS) of C6 is 601 MPa, whereas the ultimate tensile strength (UTS) of T6 is 594 MPa. The yield strength (0.2% offset strain) shows a value of 515 MPa for C6 and 525 MPa for T6. The stress-strain curve of T6 shows serrations, and the steel is more susceptible to strain localization [45].

The measured metal hardness for C6 and T6 is 205 *HV* and 206 *HV* respectively, at 4.9 N indentation load.

2.3.3. DIC analysis

Figure 2.6 shows the specimen design (thickness 1 mm) and the result of DIC analysis. Correlation calculation was performed with respect to the initial virgin specimen without any loading. The result of DIC analysis is shown in Figs. 2.6 (a) and (b), where the longitudinal normal strain (ε_{yy}) map was measured along the notch tip. The figure shows the strain contour maps, $\varepsilon_{yy,}$ at the notch tip in C6 and T6 for the stroke displacement, δ, of 0.25 mm. The correlation study was carried out at $\delta = 0.25$ mm as it corresponds to stress near the yield strength of the material. We can observe that for the same initial

displacement, the strain is uniformly and symmetrically distributed in the case of C6 while it is highly localized and asymmetric for T6. The strain localization in the case of T6 resembles that of strain localization along the slip planes.

2.3.4. Fatigue test

The objective of this test is to find out the crack growth behaviour with the number of cycles for two materials, two artificial defect geometry, and also to find out the fatigue limit for each defect.

The crack length versus the number of cycles curve for both types of tests and for both materials is shown in Figs. 2.7 and 2.8. For the case of short crack, C6 in Fig. 2.7, shows a slower crack growth as compared to T6 and thus has better resistance to fatigue crack growth. The crack growth in T6 for the short crack region is relatively much faster. Figures 2.7 (b) and (c) shows the replica images taken for the case of short crack growth in C6 and T6. The crack growth in the case of C6 is tortious in nature. The amount of deflection during crack growth is considerable. On the other hand, for T6, the crack growth is relatively less prone to deflections.

The comparison of crack growth data for long crack is shown in Fig. 2.8. The plot shows that the growth of the fatigue crack in T6 is almost retarded throughout the initiation and propagation phase. Although the crack growth of C6 in the initial stage is even slower than that of T6, after around 5.6×10^5 cycles, there is a sudden increase in the crack growth rate of C6. At around 5.8×10^5 cycles, there is a cross-over between the crack growth rate of C6 and T6. After 5.8×10^5 cycles, the crack grows abruptly in the case of C6. Figures 2.8(b) and (c) shows the optical images of the crack growth for the case of long crack. Here we can see that both C6 and T6 shows almost straight path crack growth.

Figure 2.9 shows the *S-N* diagram for two materials and two artificial defects. For C6, the corresponding fatigue limits in the case of plain specimen, specimen with short crack and specimen with long crack are 238 MPa, 230 MPa and 132 MPa respectively. For T6, the corresponding fatigue limits in the case of plain specimen, specimen with short crack and specimen with long crack are 260 MPa, 225 MPa and 140 MPa respectively.

Figure 2.10 shows the non-propagating cracks. All the fatigue limits are defined by crack non-propagation. Therefore, it is confirmed that Murakami's prediction equation [28] can be applied to the tested materials.

Focusing on the non-propagating crack tip, it is not possible to determine the location of the crack tip in T6 due to the small grain size, however in C6 with large grain size, the crack tip is within the grain. This supports the fact that the cracks were arrested by the crack-closure phenomenon.

2.4 Discussion

Discussion will be based on the empirical rule established at classified regions by each initial crack length ($\sqrt{area}$). The regions are no-damage, short, and long crack regions. On the other hand, we discuss unifying way in the fatigue process through fatigue crack initiation and fatigue crack growth and the crack non-propagation due to strain localization and plasticity-induced-crack-closure (PICC). From the shape of the deflected non-propagation crack shown in Fig. 2.10(d), it can be considered as necessary to discuss the effect of roughness-induced-crack-closure (RICC) [46, 47] as well as PICC [48-50] on the crack closure. In this chapter, however, the non-propagation crack shape is a three-dimensional crack that initiated from small artificial defects, and it is not possible to determine the whole crack shape from the surface crack shape alone. Therefore, in this chapter, I discuss only the PICC effect, which is considered to exist with certainty.

2.4.1 Mechanism of strain localization effect

The grain size of T6 steel is relatively fine as compared to the grain size of C6 as shown in Fig. 2.4. The precipitates exhibited by T6 is relatively hard as compared to the soft precipitate exhibited by C6. Therefore, in the first case, it seems that T6 should have better fatigue crack growth resistance [51, 52] based on classical fracture mechanics theory. However, on evaluating the mechanical property of the two steels as shown in Fig. 2.5, we can conclude that both the steels have nearly same UTS, yield strength, and total elongation except for the dynamic strain aging (serrations) shown by T6. The same mechanical tensile properties of the two steels will contradict the previous statement in

which T6 seems to be superior ($\sigma_{wo} \cong 0.5\ \sigma_U$, σ_{wo} is fatigue limit of plain specimen and σ_U is tensile strength). Moreover, since UTS is same, fatigue crack resistance of both steels should also show a competing nature instead of being superior and inferior to each other [28, 53, 54]. For the competing nature, we focused on the mechanism of strain localization effects under each fatigue limit conditions. Since T6 bears hard TiC precipitates it can be pre-assumed that the affinity for strain localization will be more in T6 as compared to C6, though the strain localization not only depends on hardness of precipitates but also on their distribution. Study of TiC precipitation kinetics in ferritic steel by Kobayashi et al. [55] shows a non-uniform distribution of TiC precipitates in the pre-deformed steel. Since the present steel, T6, is also rolled (35 mm to 5.5 mm), it can be safely assumed as a pre-deformed steel. Thus, a strain localization is confirmed for T6 by conducting mechanical tests (tensile test and DIC test).

2.4.1.1. No-damage crack region

In this region, the initial crack length is so short to have any change in fatigue limit [56, 57]. Then the fatigue limit of the specimen with the crack is the same as that of the plain specimen. The fatigue limit does not depend on the initial crack length and shows a constant value in this region. The size of the region, i.e., the initial crack length at which the length of the initial crack affects the fatigue limit, depends on the material.

From Fig. 2.9, the fatigue limit of the plain specimen of T6 is superior to C6. In this region for plain specimen, crack initiates in the length of its grain size. As shown in Fig. 2.4, the grain size of T6 is quite smaller than C6. Therefore, at the fatigue limit condition, T6 shows smaller length initial crack than C6, and the crack shows non-propagation behaviour. For this reason, T6 shows a superior fatigue limit than C6 in this region.

2.4.1.2. Short crack region

In this region, the fatigue limit of the material depends on the Vickers hardness and initial crack length, as indicated by the following equation by Murakami [28].

$$\sigma_w = \frac{1.43(HV+120)}{(\sqrt{area})^{1/6}} \quad (2.2)$$

Therefore, it is important to study the hardness of two materials and their behaviour for the different initial crack length ($\sqrt{area}$). The hardness in a grain for the two steels show almost the same value, which concludes their neutrality for fatigue crack resistance based on the hardness of the two materials.

However, as shown in Fig. 2.7, the short crack growth behaviour for two steels shows that the fatigue crack resistance for T6 is highly deteriorated compared to C6. Figure 2.11(a) shows the relationship between the crack growth rate and crack length for the short cracks. This figure also shows the inferiority of T6 in the short crack region. The crack growth rate for C6 shows a periodic decrease in the short crack region, which should be the effect of crack deflection, as shown in Fig. 2.7(b). Furthermore, as shown in Fig. 2.9, the fatigue limit of T6 is lower than C6. It can be explained by focusing on the effect of strain localization and PICC as follows. As shown in Fig. 2.6, T6 shows severe strain localization than C6. As a result, the plastic deformation region near the crack tip, that produces the PICC in T6, is narrower, longer, and more asymmetric for the crack propagation surface than that in C6 [58]. Therefore, the shape of the plastic region formed in T6 is considered to be asymmetric rather than line-symmetric, as expected from the elastic solution. Therefore, the effect of the PICC produced by the plastic region in the wake of the same length of non-propagating crack for the short crack specimen is smaller for T6 than for C6. Then, T6 shows a lower fatigue limit than C6 in this region.

2.4.1.3. Long crack region

In this region, the threshold value of the stress intensity factor range ΔK_{th} is constant [35], independent of the initial crack size. Then the fatigue limit of the material with a crack is indicated as:

$$\sigma_w = \frac{\Delta K_{\text{th}}}{2\sqrt{\pi a}} \quad (\text{for } R = -1) \quad (2.3)$$

where a is the initial crack length

Therefore, the fatigue limit depends on the constant ΔK_{th} value.

In the long crack region, as shown in Fig. 2.8, fatigue crack growth resistance of T6 is better than C6, although C6 shows even better resistance up to a certain crack length. Figure 2.11(b) shows the relationship between the crack growth rate and crack length for the long crack. This figure also shows the superiority of T6 in the long crack region. It can also be explained by focusing on the effect of the strain localization and PICC as follows. As described in the previous sub-section, T6 shows narrower, longer, and more asymmetric plastic deformation region for the crack propagation surface than that in C6. However, in this region, the applied stress intensity factor range ΔK that reflect plastic region size is higher, because the threshold stress intensity factor ΔK_{th} for long crack is higher than that of short crack [28]. Additionally, as shown in Fig. 2.10, the length of the non-propagating crack is longer than the short crack region. The high cyclic ΔK and long crack length may break the asymmetry that occurs in the short crack wake for T6, and the shape of the plastic deformation that occurs in the crack wake is likely to be more symmetrical. Since the length of the plastic region obliquely interior to the crack tip is longer for T6 than in C6, the width of the plastic deformation area in the crack wake is considered to be wider in T6. Therefore, the effect of PICC is greater for T6. Then, T6 shows a higher fatigue limit than C6 in this region.

The crack non-propagation behaviour discussed in this sub-section is governed by the shape of the plastic region in the crack wake, which we have assumed. Experimental or analytical methods can verify the validity of these assumptions. The former is the measurement of plastic strain using the high-precision DIC method or the measurement of kernel-average-misorientation (KAM) value, which depends on the magnitude of plastic strain, which can be obtained using electron-back-scatter-diffraction (EBSD) method [59]. The latter is a crystal plasticity finite element method (CP-FEM) analysis [60] that can represent the localized behaviour of the strain [61]. These are our future tasks.

2.4.2. New finding of strain localization effect

By using Eqns. 2.2 and 2.3, we draw two lines consisting of three regions through data points of the results for each material. Figure 2.12 shows the lines, and the transition is confirmed by carrying out the fatigue test on the specimens with no-damage, short and long crack regions. The fatigue limits in this figure are obtained by Fig. 2.9; the plotted points show the fatigue limit in the respective regions. The intersection of the curve justifies our prediction of transition in fatigue property based on the initial crack length. Comparing T6 and C6, for T6 strain localization is likely to occur and the fatigue limit is less than C6 in the short crack regime.

2.5. Conclusions

As a result of carrying out fatigue tests using two precipitation-strengthened steels, that is, material susceptible to strain localization (T6) and material without such properties (C6), the following conclusions can be drawn from this chapter:

1. Although both materials have almost same yield strength, tensile strength, and total elongation, the fatigue crack propagation resistance in a short crack region is better for C6, and fatigue crack propagation resistance in a long crack region is better for T6.
2. The crack growth in T6 is almost abrupt in the short crack region. For long crack, the crack growth in C6 is although retarded up to a considerable crack length, after which there is an abrupt crack growth.
3. Comparing T6 and C6, for T6 strain localization is likely to occur, and the fatigue limit is less than C6 in the short crack regime.

The superiority of the fatigue limit of each precipitation-strengthened steel alters depending on the initial crack size.

References

[1] M. Kobayashi, M. Yamamoto, O. Miyagawa, Effect of precipitation hardening on the fatigue strength, Bull JSME 21(154) (1978) 554-560.

[2] Y. Furuya, S. Matsuoka, T. Abe, K. Yamaguchi, Gigacycle fatigue properties for high-strength low-alloy steel at 100 Hz, 600 Hz, and 20 kHz, Scripta Materialia 46(2) (2002) 157-162.

[3] C. Zhang, X. Song, P. Lu, X. Hu, Effect of microstructure on mechanical properties in weld-repaired high strength low alloy steel, Materials & Design (1980-2015) 36 (2012) 233-242.

[4] A.M. Sherman, Fatigue properties of high strength-low alloy steels, Metallurgical Transactions A 6(5) (1975) 1035.

[5] C.V. Cooper, Cyclic Deformation, Microcracks Initiation and the Effects of Surface Oxides in Polycrystalline - Iron, Ph.D. thesis, Northwestern University, Evanston, IL, 1983.

[6] W.J. Lee, Effects of Environments on Fatigue Properties of Iron and Steel, Ph.D. thesis, Northwestern University, Evanston, IL, 1987.

[7] C. Shin, M. Fivel, M. Verdier, C. Robertson, Dislocation dynamics simulations of fatigue of precipitation-hardened materials, Materials Science and Engineering: A 400 (2005) 166-169.

[8] R.W. Landgraf, Cyclic deformation and fatigue behavior of hardened steels, Department of Theoretical and Applied Mechanics (UIUC), 1968.

[9] Y. Hamano, M. Koyama, S. Hamada, H. Noguchi, Notch Sensitivity of the Fatigue Limit in High-Strength Steel, ISIJ International 56(8) (2016) 1480-1486.

[10] H. Itoga, K. Tokaji, M. Nakajima, H.-N. Ko, Effect of surface roughness on step-wise S–N characteristics in high strength steel, International Journal of fatigue 25(5) (2003) 379-385.

[11] C.M. Carman, J.M. Katlin, Low cycle fatigue crack propagation characteristics of high strength steels, FRANKFORD ARSENAL PHILADELPHIA PA PITMAN-DUNN RESEARCH LABS, 1966.

[12] B.M. Schönbauer, K. Yanase, M. Endo, VHCF properties and fatigue limit prediction of precipitation hardened 17-4PH stainless steel, Int. J. Fatigue 88 (2016) 205-216.

[13] D. Greitemeier, C. Dalle Donne, F. Syassen, J. Eufinger, T. Melz, Effect of surface roughness on fatigue performance of additive manufactured Ti–6Al–4V, Materials Science and Technology 32(7) (2016) 629-634.

[14] B.M. Schönbauer, K. Yanase, M. Endo, The influence of various types of small defects on the fatigue limit of precipitation-hardened 17-4PH stainless steel, Theoretical and Applied Fracture Mechanics 87 (2017) 35-49.

[15] E. Wycisk, A. Solbach, S. Siddique, D. Herzog, F. Walther, C. Emmelmann, Effects of defects in laser additive manufactured Ti-6Al-4V on fatigue properties, Physics Procedia 56 (2014) 371-378.

[16] H. Wu, S. Hamada, H. Noguchi, Pre-strain effect on fatigue strength characteristics of SUH660 plain specimens, International Journal of Fatigue 55 (2013) 291-298.

[17] H. Wu, S. Hamada, H. Noguchi, Fatigue strength characteristics evaluation of SUH660 considering small fatigue crack propagation behavior and hardness distribution, International Journal of Fatigue 63 (2014) 1-11.

[18] M.D. Sangid, H.J. Maier, H. Sehitoglu, A physically based fatigue model for prediction of crack initiation from persistent slip bands in polycrystals, Acta Materialia 59(1) (2011) 328-341.

[19] I. Picas, N. Cuadrado, D. Casellas, A. Goez, L. Llanes, Microstructural effects on the fatigue crack nucleation in cold work tool steels, Procedia Engineering 2(1) (2010) 1777-1785.

[20] M. Fine, D. Isheim, Origin of copper precipitation strengthening in steel revisited, Scripta materialia 53(1) (2005) 115-118.

[21] D.C. William, Materials science and engineering: an introduction, John wiley2014.

[22] D.D. Krueger, S.D. Antolovich, R.H. Van Stone, Effects of grain size and precipitate size on the fatigue crack growth behavior of alloy 718 at 427 C, Metallurgical transactions A 18(8) (1987) 1431-1449.

[23] A. McEvily, R. Snyder, J. Clark, The effect of nonuniform precipitation on the fatigue properties of an age hardening alloy, Trans TMS-AIME 227 (1963) 452-458.

[24] S. Hamada, J. Zhang, K. Zhang, M. Koyama, T. Tsuchiyama, T. Yokoi, H. Noguchi, Ductile-to-brittle transition in tensile failure due to shear-affected zone with a stress-concentration source: a comparative study on punched-plate tensile-failure characteristics of precipitation-hardened and dual-phase steels, International Journal of Fracture 212(2) (2018) 237-248.

[25] K. Tanaka, Y. Nakai, M. Yamashita, Fatigue growth threshold of small cracks, International Journal of fracture 17(5) (1981) 519-533.

[26] Y. Murakami, S. Kodama, S. Konuma, Quantitative evaluation of effects of non-metallic inclusions on fatigue strength of high strength steels. I: Basic fatigue mechanism and evaluation of correlation between the fatigue fracture stress and the size and location of non-metallic inclusions, International Journal of Fatigue 11(5) (1989) 291-298.

[27] S. Suresh, Fatigue of Materials, 2 ed., Cambridge University Press, Cambridge, 1998.

[28] Y. Murakami, Metal fatigue: effects of small defects and nonmetallic inclusions, 2nd ed., Academic Press, London, 2019.

[29] H. Nisitani, M. Goto, N. Kawagoishi, A small-crack growth law and its related phenomena, Eng. Fract. Mech. 41(4) (1992) 499-513.

[30] American Society for Testing and Materials, ASTM E647-13e1, Standard Test Method for Measurement of Fatigue Crack Growth Rates, ASTM International, West Conshohocken, PA, 2013.

[31] Y. Murakami, M. Endo, Effects of hardness and crack geometries on DK_{th} of small cracks emanating from small defects, in: K.J. Miller, E.R. de los Rios (Eds.), The Behaviour of Short Fatigue Cracks, Mechanical Engineering Publications, London, 1986, pp. 275-293.

[32] P. Lukáš, M. Klesnil, Fatigue limit of notched bodies, Materials Science and Engineering 34(1) (1978) 61-66.

[33] M. El Haddad, T. Topper, K. Smith, Prediction of non propagating cracks, Engineering fracture mechanics 11(3) (1979) 573-584.

[34] W. Elber, Fatigue crack closure under cyclic tension, Eng. Fract. Mech. 2(1) (1970) 37-45.

[35] S. Hamada, T. Kinoshita, K. Morishige, K. Hayashi, T. Ishina, H. Noguchi, Engineering definitions of small crack and long crack at fatigue limit under tensile mean stress and a prediction method for determining the fatigue limit of a cracked Mg alloy, Int. J. Fatigue 56 (2013) 86-94.

[36] M.D. Chapetti, Fatigue propagation threshold of short cracks under constant amplitude loading, International Journal of Fatigue 25(12) (2003) 1319-1326.

[37] R.C. McClung, Crack closure and plastic zone sizes in fatigue, Fatigue & fracture of engineering materials & structures 14(4) (1991) 455-468.

[38] H.-B. Park, K.-M. Kim, B.-W. Lee, Plastic zone size in fatigue cracking, International journal of pressure vessels and piping 68(3) (1996) 279-285.

[39] J. Vasco-Olmo, M. James, C. Christopher, E. Patterson, F. Díaz, Assessment of crack tip plastic zone size and shape and its influence on crack tip shielding, Fatigue & Fracture of Engineering Materials & Structures 39(8) (2016) 969-981.

[40] V. Tarigopula, O. Hopperstad, M. Langseth, A. Clausen, F. Hild, A study of localisation in dual-phase high-strength steels under dynamic loading using digital image correlation and FE analysis, International Journal of Solids and Structures 45(2) (2008) 601-619.

[41] H. Munoz, A. Taheri, E. Chanda, Pre-peak and post-peak rock strain characteristics during uniaxial compression by 3D digital image correlation, Rock Mechanics and Rock Engineering 49(7) (2016) 2541-2554.

[42] K. Habib, M. Koyama, H. Noguchi, Impact of Mn–C couples on fatigue crack growth in austenitic steels: Is the attractive atomic interaction negative or positive?, Int. J. Fatigue 99 (2017) 1-12.

[43] H. Nishitani, N. Kawagoishi, Fatigue crack growth laws in small and large cracks and their physical background, JSME International Journal, Series 1: Solid Mechanics, Strength of Materials 35(1) (1992) 1-11.

[44] S. Hamada, T. Fujisawa, M. Koyama, N. Koga, N. Nakada, T. Tsuchiyama, M. Ueda, H. Noguchi, Strain mapping with high spatial resolution across a wide observation range by digital image correlation on plastic replicas, Materials Characterization 98 (2014) 140-146.

[45] S. Graff, S. Forest, J.L. Strudel, C. Prioul, P. Pilvin, J.L. Béchade, Strain localization phenomena associated with static and dynamic strain ageing in notched specimens: Experiments and finite element simulations, Materials Science and Engineering A 387-389(1-2 SPEC. ISS.) (2004) 181-185.

[46] S. Kumai, A. Sekikawa, J. Hu, Y. Higo, S. Nunomura, Effects of roughness-induced crack closure on fatigue crack growth in AC4CH cast aluminum alloys, Keikinzoku 45(4) (1995) 204-206.

[47] S. Kumai, A. Sekikawa, J. Hu, Y. Higo, S. Nunomura, Effects of roughness-induced crack closure on fatigue crack growth in AC4CH cast aluminium alloys, International Journal of Fatigue 2(19) (1997) 184.

[48] Y. Jiang, M. Feng, F. Ding, A reexamination of plasticity-induced crack closure in fatigue crack propagation, International Journal of Plasticity 21(9) (2005) 1720-1740.

[49] K. Solanki, S. Daniewicz, J. Newman Jr, Finite element modeling of plasticity-induced crack closure with emphasis on geometry and mesh refinement effects, Engineering Fracture Mechanics 70(12) (2003) 1475-1489.

[50] P. De Matos, D. Nowell, Experimental and numerical investigation of thickness effects in plasticity-induced fatigue crack closure, International Journal of Fatigue 31(11-12) (2009) 1795-1804.

[51] G.E. Dieter, Mechanical metallurgy, SI metric ed. / adapted by David Bacon ed., McGraw-Hill Book Company, London, UK, 1988.

[52] K. Tokaji, K. Ohya, H. Kariya, Effect of grain size on fatigue strength and subsurface crack initiation in beta Ti-22V-4Al alloy, Zairyo/Journal of the Society of Materials Science, Japan 49(9) (2000) 994-1001.

[53] J. Pang, S. Li, Z. Wang, Z. Zhang, General relation between tensile strength and fatigue strength of metallic materials, Materials Science and Engineering: A 564 (2013) 331-341.

[54] J. Gayda, R. Miner, The effect of microstructure on 650° C fatigue crack growth in P/M astroloy, Metallurgical Transactions A 14(11) (1983) 2301.

[55] Y. Kobayashi, J. Takahashi, K. Kawakami, Effects of dislocations on the early stage of TiC precipitation kinetics in ferritic steel: A comparative study with and without a pre-deformation, Acta Materialia 176 (2019) 145-154.

[56] P. Lukáš, L. Kunz, B. Weiss, R. Stickler, Non-damaging notches in fatigue, Fatigue & fracture of engineering materials & structures 9(3) (1986) 195-204.

[57] D. Kujawski, F. Ellyin, A cumulative damage theory for fatigue crack initiation and propagation, International Journal of Fatigue 6(2) (1984) 83-88.

[58] A. Gonzalez-Herrera, J. Zapatero, Numerical study of the effect of plastic wake on plasticity-induced fatigue crack closure, Fatigue & Fracture of Engineering Materials & Structures 32(3) (2009) 249-260.

[59] N. Nakada, K. Ikeda, H. Shuto, T. Yokoi, T. Tsuchiyama, S. Hata, H. Nakashima, S. Takaki, Quantification of large deformation with punching in dual phase steel and change of its microstructure –Part II: Local strain mapping of dual phase steel by a combination technique of electron backscatter diffraction and digital image correlation methods, ISIJ International 56(11) (2016) 2077-2083.

[60] R.J. Asaro, Geometrical effects in the inhomogeneous deformation of ductile single crystals, Acta Metall. 27(3) (1979) 445-453.

[61] F. Roters, M. Diehl, P. Shanthraj, P. Eisenlohr, C. Reuber, S.L. Wong, T. Maiti, A. Ebrahimi, T. Hochrainer, H.O. Fabritius, S. Nikolov, M. Friák, N. Fujita, N. Grilli, K.G.F. Janssens, N. Jia, P.J.J. Kok, D. Ma, F. Meier, E. Werner, M. Stricker, D. Weygand, D. Raabe, DAMASK – The Düsseldorf Advanced Material Simulation Kit for modeling multi-physics crystal plasticity, thermal, and damage phenomena from the single crystal up to the component scale, Computational Materials Science 158 (2019) 420-478.

List of tables and figures

Table 2.1. Chemical composition of C6 and T6 (wt.%)

	C	Si	Mn	P	S	T. Al	N	Ti	Cu
C6	0.0016	0.032	0.20	<0.002	0.0007	0.020	0.0030	0.046	1.60
T6	0.089	0.19	0.79	<0.002	0.0005	0.024	0.0030	0.079	-

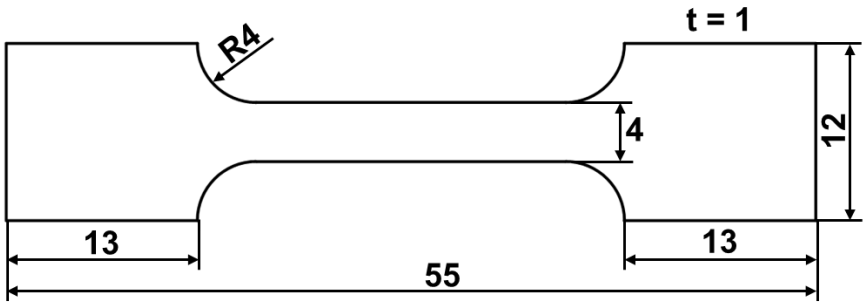

Fig. 2.1. Tensile specimen geometry (all dimensions in mm).

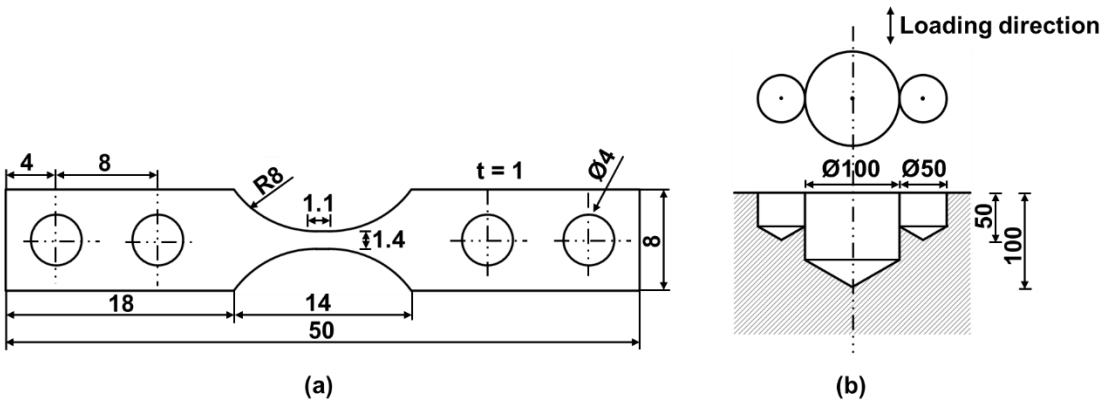

Fig. 2.2. (a) Specimen geometry for rotating bending test (all dimensions in mm), (b) artificial defect geometry for short crack (all dimensions in μm).

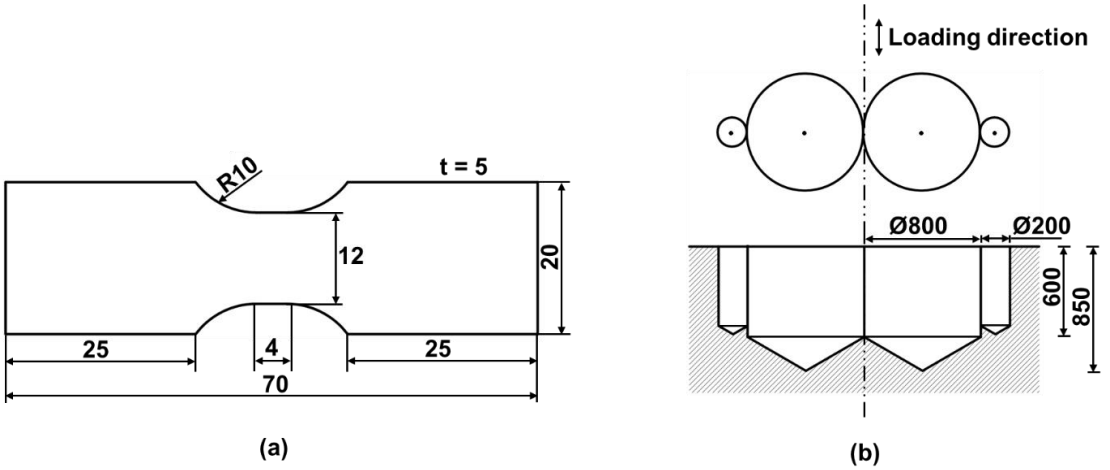

Fig. 2.3. (a) Tension- compression test specimen geometry for long crack (all dimensions in mm), (b) artificial defect geometry for long crack (all dimensions in μm).

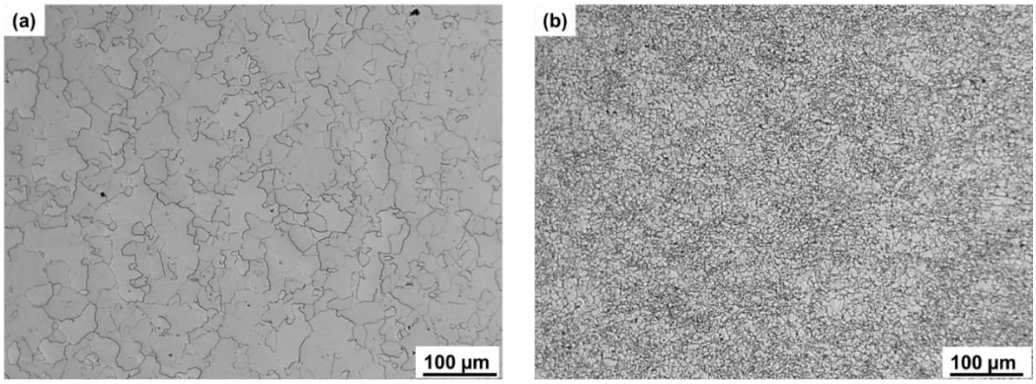

Fig. 2.4. Microstructure of the steels used in this chapter (a) C6, (b) T6.

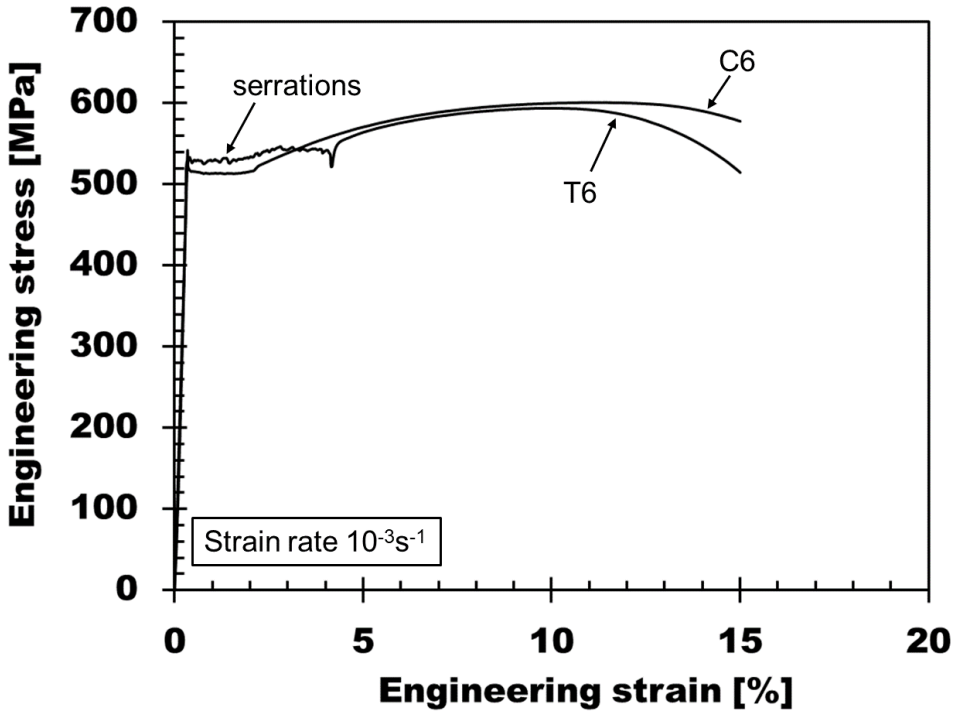

Fig. 2.5. Engineering stress-strain curves for C6 and T6.

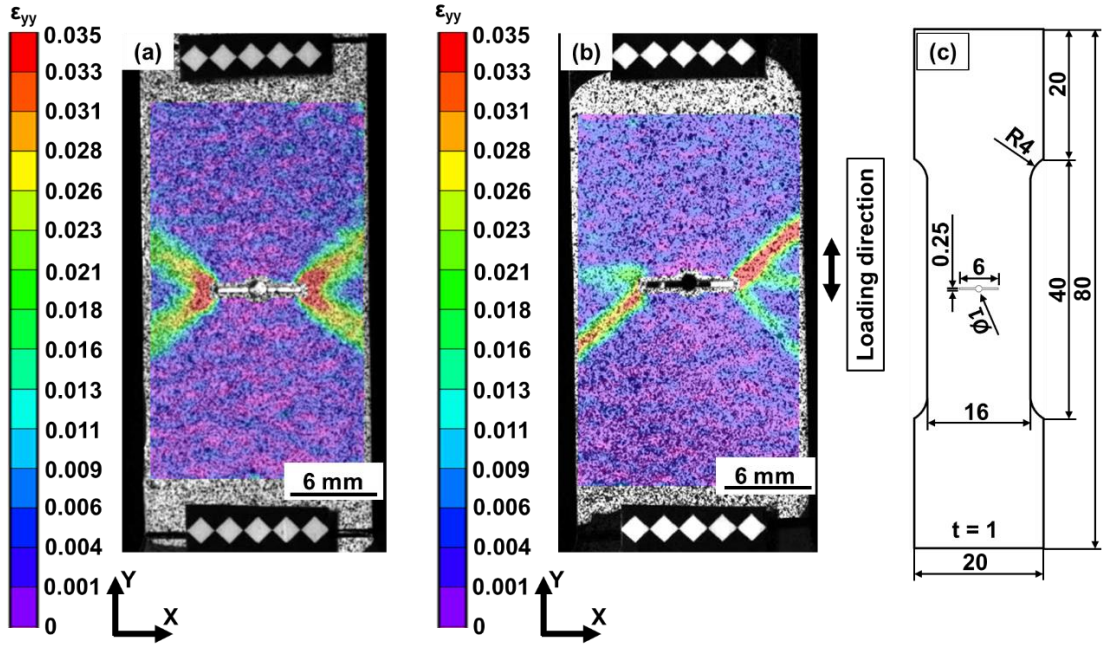

Fig. 2.6. DIC strain measurement analysis (a) C6 (b) T6, (c) DIC specimen geometry (all dimensions in mm).

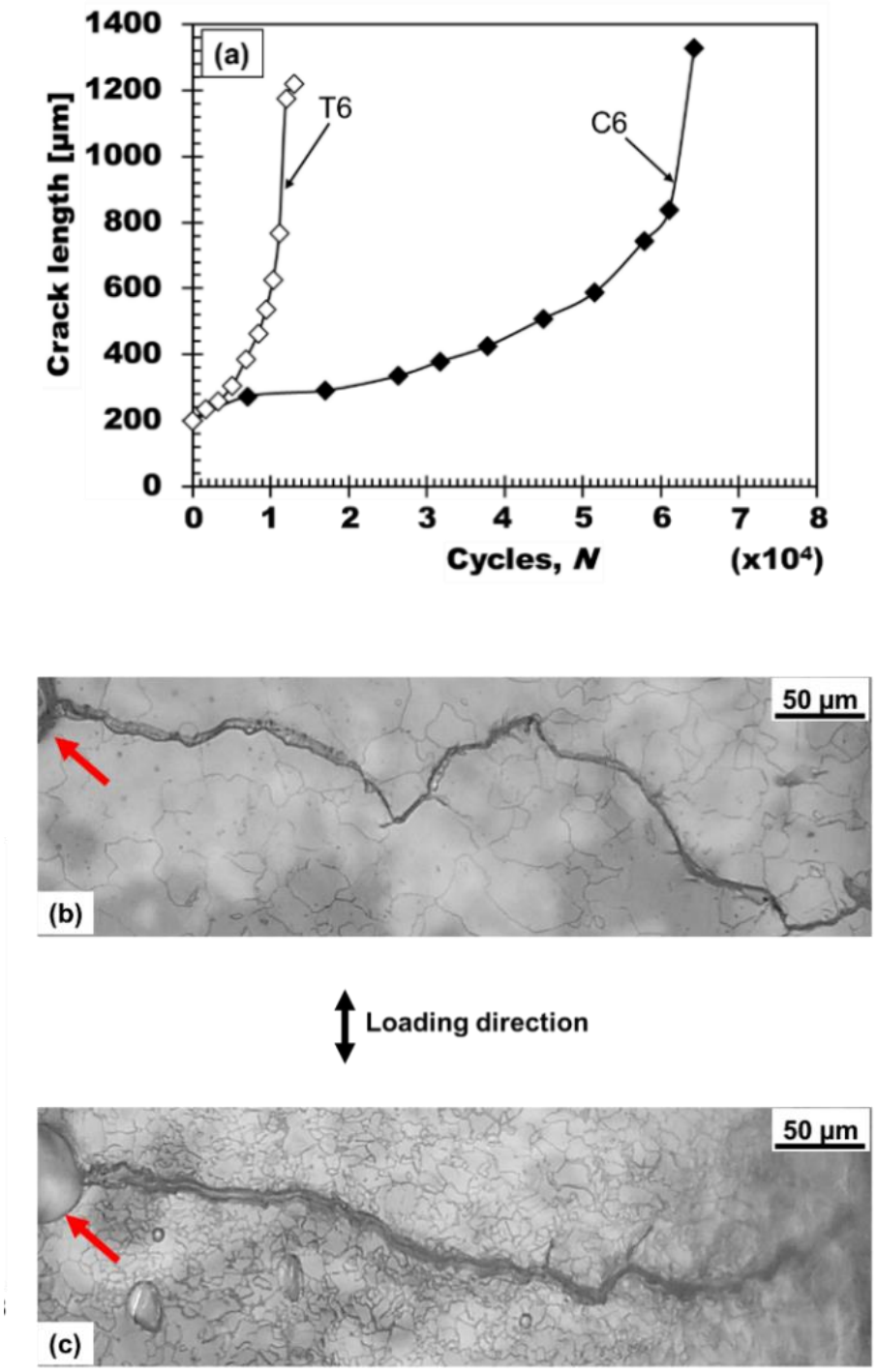

Fig. 2.7. (a) Plot of crack length vs. number of cycles for C6 and T6 (short crack), σ_a = 350 MPa, replica images for crack growth monitoring (b) C6 at N= 6.4 × 10^4 cycles (c) T6 at N= 1.3 × 10^4 cycles. The red arrow represents the artificial notch.

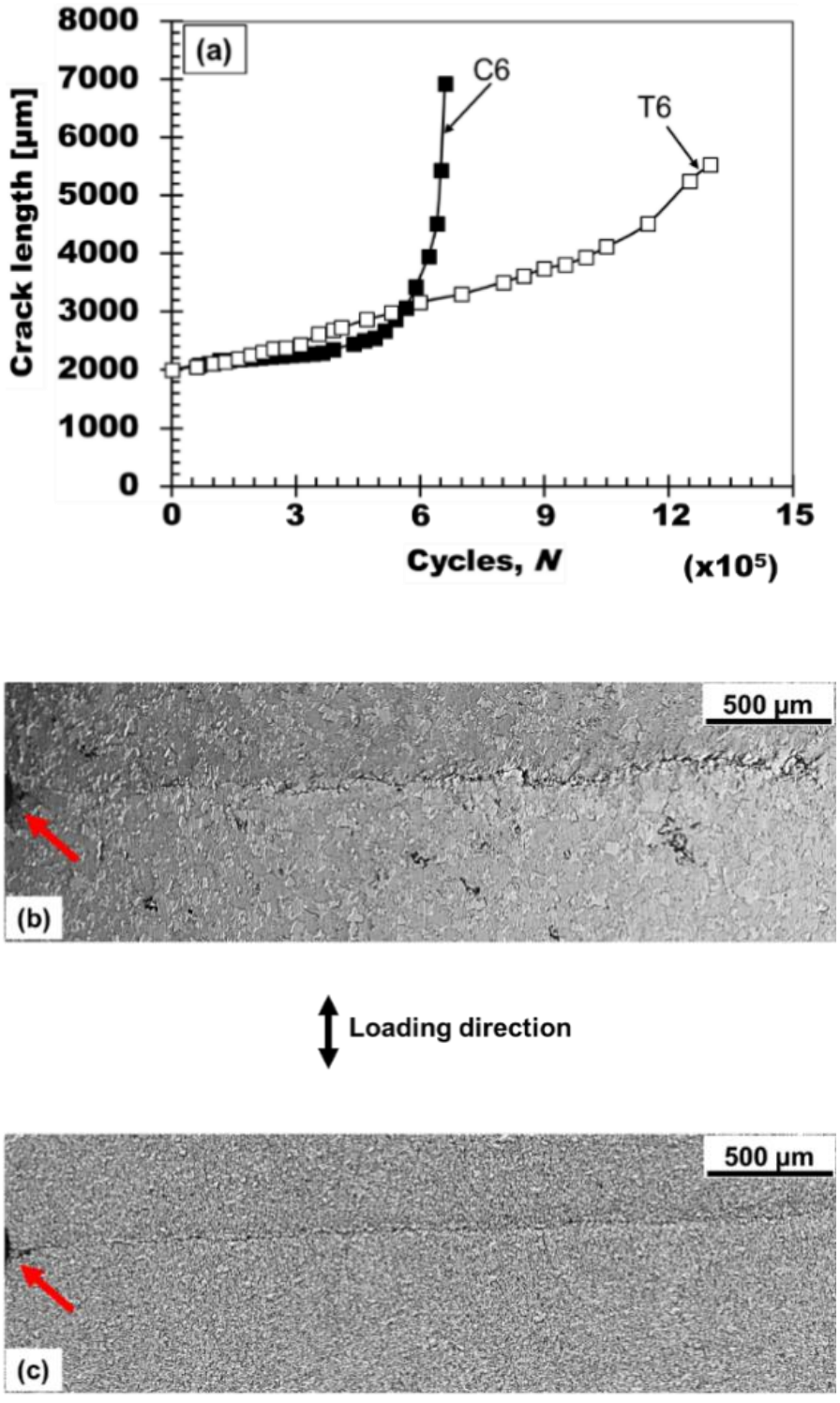

Fig. 2.8. (a) Plot of crack length vs number of cycles for C6 and T6 (long crack), σ_a = 200 MPa, optical images for crack growth monitoring (b) C6 at N= 6.6 × 10^5 cycles (c) T6 at N= 13 × 10^5 cycles. The red arrow represents the artificial notch.

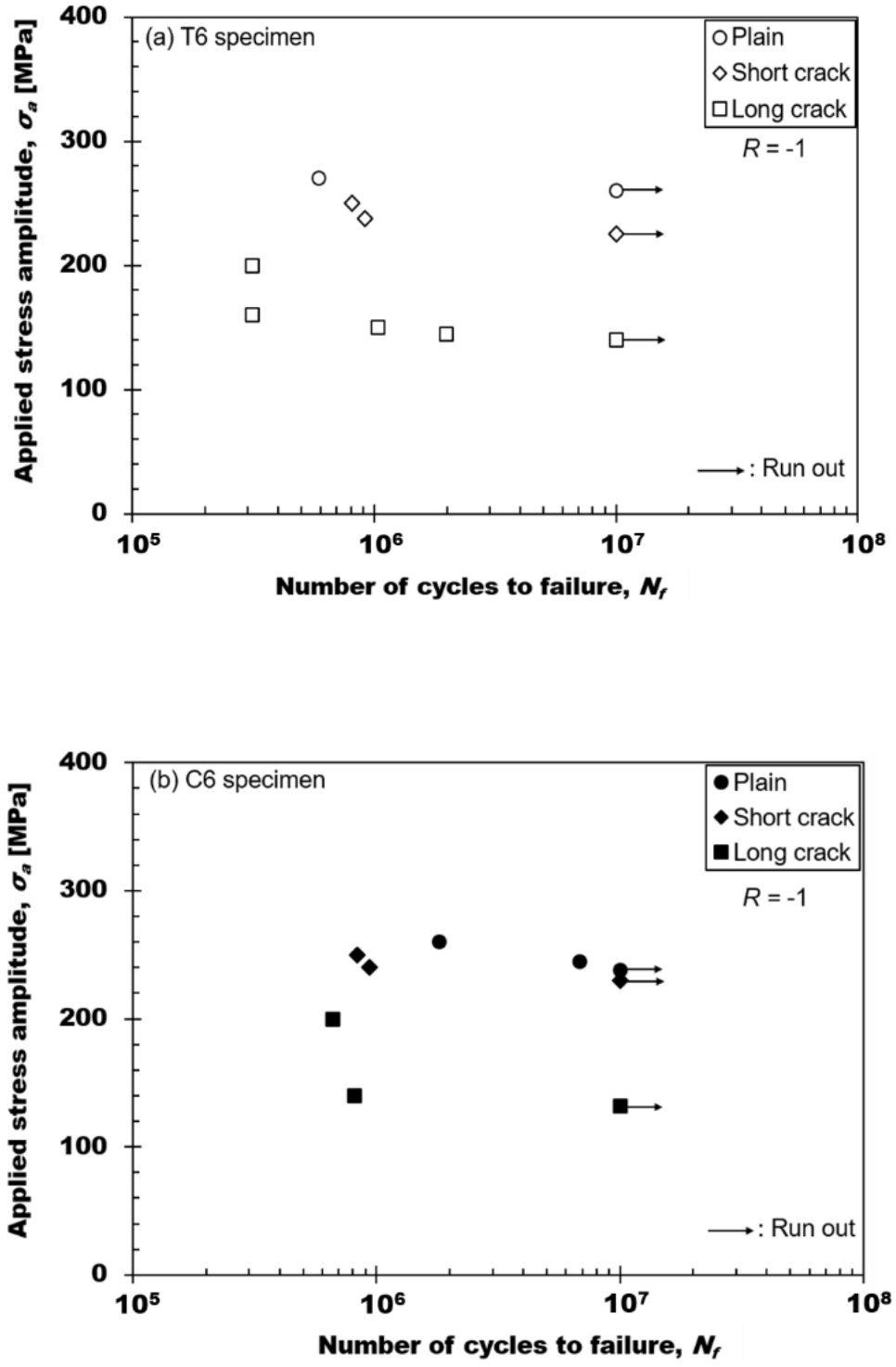

Fig. 2.9. *S-N* diagrams for (a) T6 specimen (b) C6 specimen.

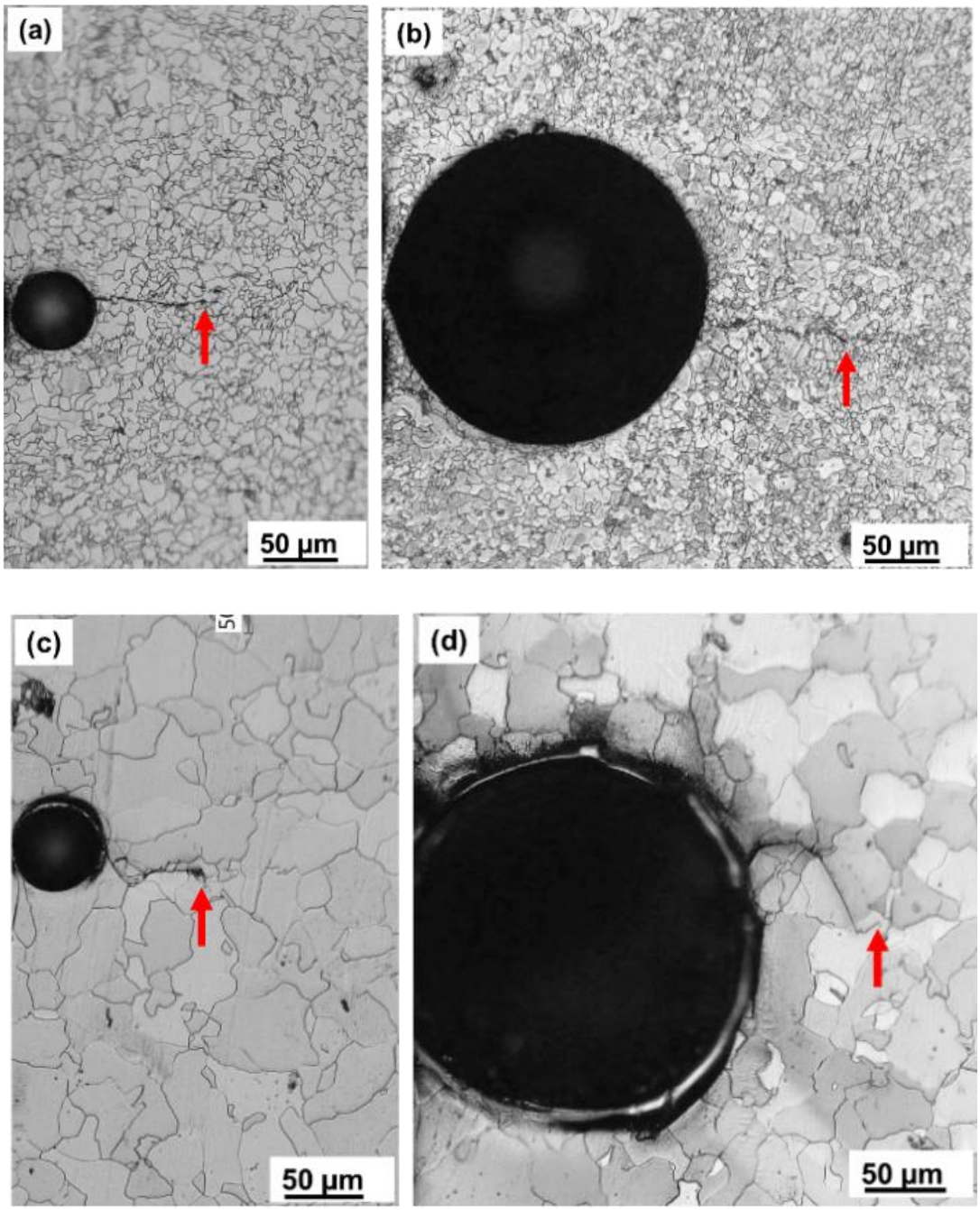

Fig. 2.10. Non-propagating cracks at fatigue limit loading after $N = 10^7$ cycles, the arrows indicate non-propagating crack tips; (a) T6, short crack specimen, σ_a = 225 MPa, (b) T6, long crack specimen, σ_a = 140 MPa, (c) C6, short crack specimen, σ_a = 230 MPa, (d) C6, long crack specimen, σ_a = 132 MPa.

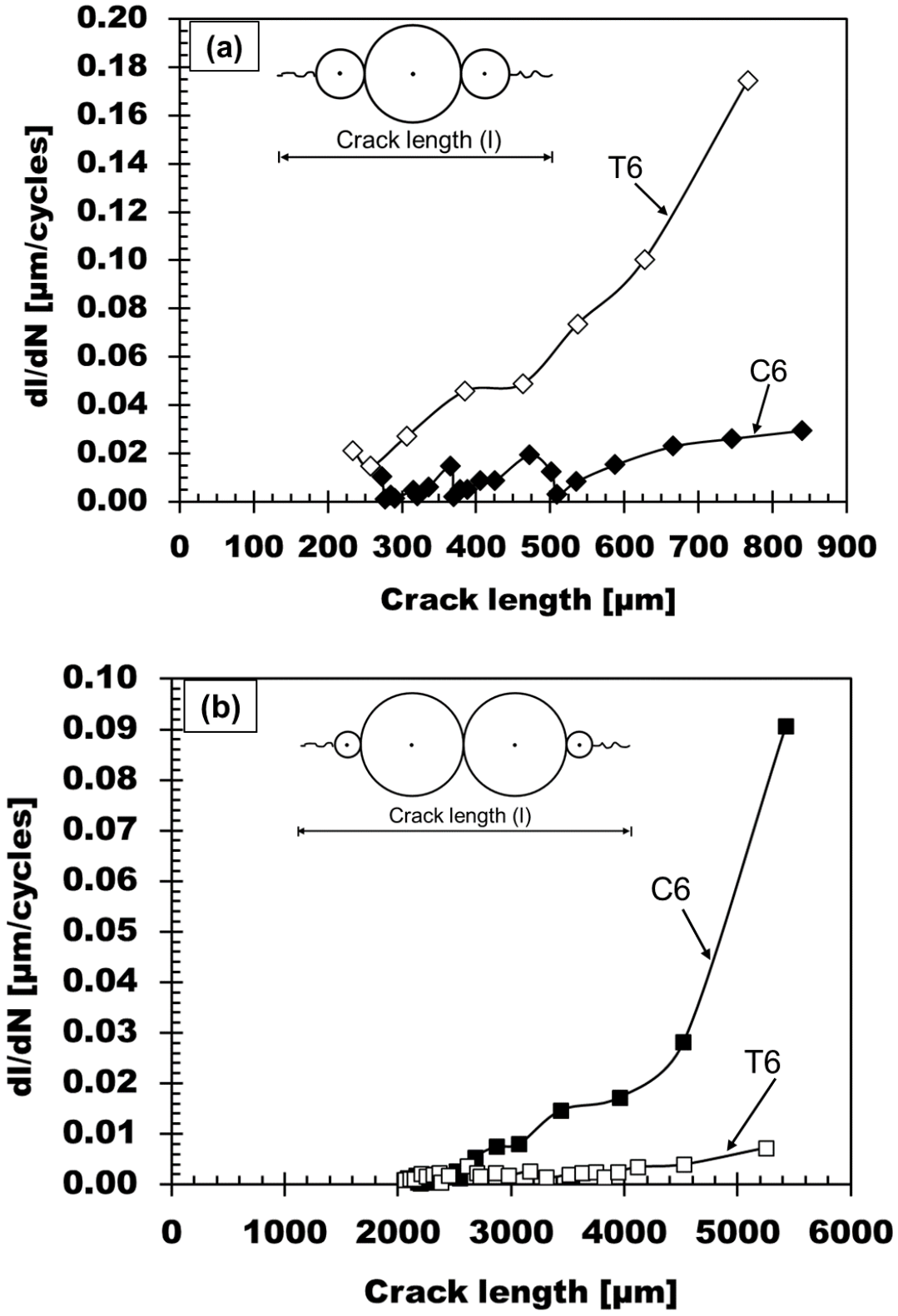

Fig. 2.11. Relationship between crack growth rate and crack length for C6 and T6 (a) short crack ($\sigma_a = 350$ MPa) (b) long crack ($\sigma_a = 200$ MPa).

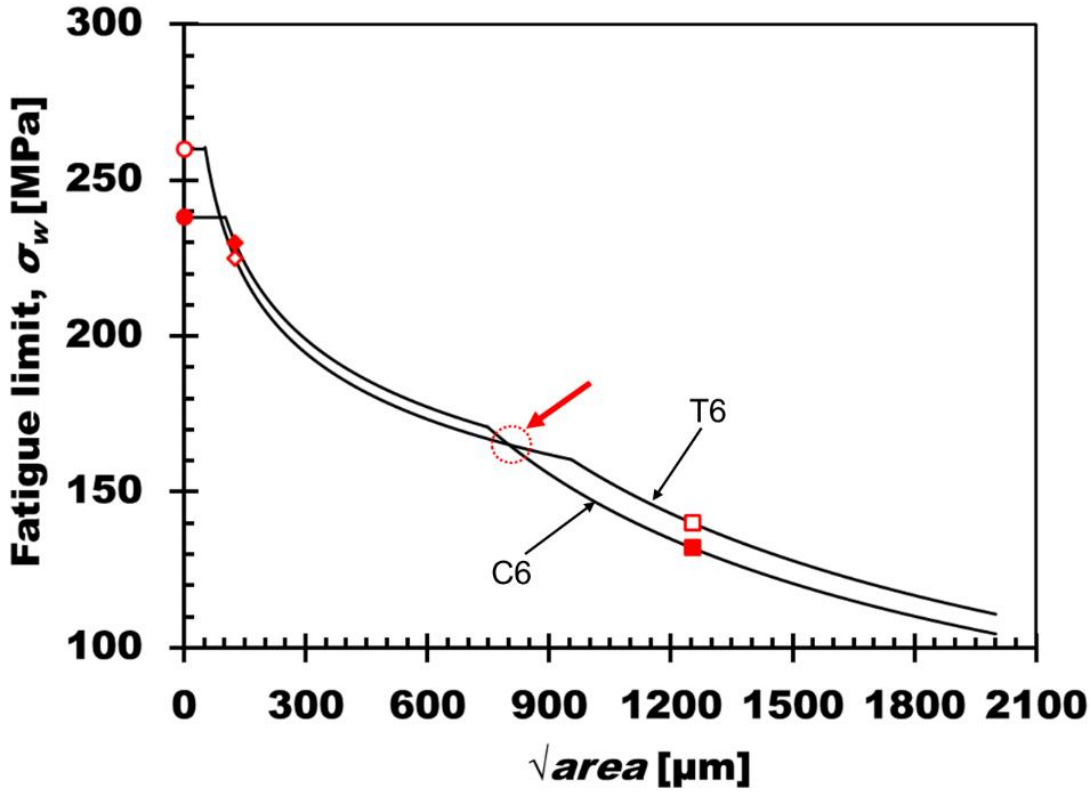

Fig. 2.12. Plot of fatigue limit (σ_w) vs $\sqrt{area}$ for C6 and T6 in different crack regimes showing the transition in fatigue property (encircled region indicated by arrow).

Chapter 3 Multiple damage mechanisms facilitated by planar dislocation glide in a commercial grade precipitation-strengthened Fe–Ni–Cr-based steel

3.1. Introduction

The importance of austenitic steels has increased recently because of their high work hardenability and associated uniform elongation [1-3]. Key factors endowing the work hardenability are planar dislocation glide and subsequent deformation twinning. Actually, twinning-induced plasticity steels and some precipitation-strengthened steels realize their superior strength–ductility balance related to planar dislocation glide [4, 5]. However, in terms of post-uniform elongation, the planar dislocation glide assists the evolution of microstructural damage (nm- or μm-scale cracks or voids), which accelerates final failure [6-8]. Even in an early stage of deformation, the damage evolution can occur in steels with high dislocation planarity, in which the character degrades failure resistance when coupled with cyclic loading [9, 10] and a hydrogen environment [11, 12].

In this context, Fe–Cr–Ni austenitic steel strengthened by γ′ [$Ni_3(Al,Ti)$] precipitates [13] also shows planar dislocation glides during room temperature deformation because of the formation of an anti-phase boundary (APB) [14-16]. This APB is a result of primary dislocation cutting ordered γ′ phase. Formation of the APB enhances further dislocation movement on the same slip plane [17] and supresses the cross-slip phenomenon [18, 19]. The reluctance of cross-slip will result in the strain localization on the microstructural entities. The high strength and deformability of this steel have been noted recently because the uniform elongation and tensile strength remain even after hydrogen uptake; accordingly, the steel is considered a potential candidate material for the hydrogen environment [12, 20, 21]. However, it is also noteworthy that the post-uniform elongation was reduced by the hydrogen uptake, which is associated with dislocation planar glide

and deformation twinning [22-24]. Therefore, similar to the case of the other austenitic steels mentioned above, microstructural damage evolution would play an important role in resistance to failure. In particular, we first must understand the basic behaviour of damage evolution in precipitation-strengthened Fe–Cr–Ni austenitic steels, i.e., under monotonic tensile deformation in air at room temperature.

In γ′-precipitation-strengthened austenitic steels, the chemical composition has a great influence on the damage characteristics [25, 26] as the deformation behaviour is strongly dependent on interaction between γ′ and dislocations. Other previous studies have pointed out the role of interactions between grain boundaries, twin boundaries, and slip bands [27-29] in the damage characteristics. Takakuwa et al. [12] reported that small voids developed at the specific locations where the deformation twinning impinged [30-32]. The key concept for damage evolution in the steel is always "planar dislocation glide," or the associated microstructure evolution. However, in precipitation-strengthened austenitic steels, various microstructures, such as inclusions and grain boundaries, act as damage initiation sites [11, 12, 33]. Accordingly, we must clarify the underlying mechanism and propose specific roles of the planar dislocation glide in damage evolution.

The present study aims to characterize the damage evolution behaviour in a precipitation-strengthened austenitic steel (SUH 660) in air through damage quantification [34, 35] and site-specific microstructure characterization [36]. The damage evolution characteristics first quantified are fraction, number density of damage, and average damage size. Then, we present multiple damage mechanisms and the roles of the planar dislocation glide on the damage evolution.

3.2 Experimental procedure

3.2.1. Material

We received a commercial grade γ′-precipitation-strengthened austenitic steel. The chemical composition of the material is shown in Table 3.1. The shape of the as-received material was cylindrical bars with a diameter of 120 mm. The as-received material had already been aged at 1003 K for 16 h and then air cooled to induce precipitation of γ′

[Ni_3(Al,Ti)]. The precipitate size in an equivalent material that heat-treated with a similar condition has been reported to be below 50 nm [37]. Figure 3.1(a) shows the initial microstructure acquired by optical microscopy. The specimens for the microstructure observation were mechanically polished and subsequently etched with Kroll's reagent (98 ml distilled water, 6 ml HNO_3, 2 ml HF). The average grain size was measured to be 58 ± 4 μm. Also, note that a considerable amount of inclusions existed in the as-aged specimens. Figure 3.1(b) shows average and distribution of the inclusion size. Spacing of the inclusions along horizontal and vertical directions direction is also exhibited in Fig. 3.1(c) (The horizontal direction corresponds to the tensile direction).

3.2.2. Mechanical characterization

Vickers hardness was measured at an indentation load of 0.5 kgf with a holding time of 20 s. The Vickers hardness value for the present steel was measured to be 316 ± 3 HV.

Plate specimens in the shape of a "dog bone" were fabricated along longitudinal direction of the bar for tensile testing. The gauge dimension of the specimens was 4 mm in width, 1.2 mm in thickness, 10 mm in length (Fig. 3.2). The specimens were mechanically polished with emery papers (grades 320, 600), diamond suspension, and finally colloidal silica. Afterward, the specimens were electrochemically polished. The tensile test was performed at room temperature (296 K) at an initial strain rate of 10^{-3} s^{-1}.

3.2.3. Microstructure characterization

After tensile testing, the fracture surface was observed with a scanning electron microscope (SEM: Hitachi TM4000) operated at an acceleration voltage of 15 kV. Surface damage and internal damage were also characterized by SEM using the post-mortem specimen. For the characterization of internal damage morphology and their cross-sectional distribution, the specimen was cut along the transverse plane and mechanically polished. Then, the cross section was observed by SEM. In addition, to characterize the microstructure at a well-defined condition, a tensile test was interrupted

at 5 % strain. Then, the surface relief and internal microstructures were observed by SEM. In the 5%-strained specimen, we observed the normal plane of the tensile specimen.

3.2.4. Damage quantification

The tensile tested sample was sliced along the transverse plane. Then, the cross section obtained was polished with the emery papers, diamond suspension, and colloidal silica to obtain a mirror finish. The cross section was observed under the SEM. The amount of damage, which includes both void and crack, was quantified along 3-lines, i.e., center line and the frame above and below it at 0.2 mm from the center line. The three parameters considered for damage evaluation were damage area fraction, average damage size, and the number of damages per unit area [35, 38, 39]. Damage area fraction D was defined as

$$D = A_d/A_a \ , \tag{3.1}$$

where A_d and A_a are the area of damage and the area of the entire region of each image observed, respectively. The number of damages per unit area n was defined as

$$n = N/A_a \ , \tag{3.2}$$

where N is the number of damages for each region. The average damage size d_{ave} was defined as

$$d_{ave} = D/n. \tag{3.3}$$

3.3 Results

3.3.1. Deformation characteristics

Figure 3.3 shows engineering stress–strain curves. The stress–strain response of an Fe–18Cr–14Ni steel, which is a stable austenitic steel without precipitate [40], was also plotted for comparison. As expected, the yield strength of the present steel was higher than that of the Fe–18Cr–14Ni steel because of the precipitation-strengthening. In contrast, the post-uniform elongation of the present steel (5%) was lower than that of the Fe–18Cr–14Ni steel (19%). The low post-uniform elongation indicates low plastic deformation limit.

3.3.2. Microstructure evolution behaviour

Figure 3.4 shows the surface relief morphology of the 5%-strained specimen. It shows the deformation-induced surface relief on the surface of the specimen. The slip lines were sharp and straight. Because the height of the surface relief corresponds to the number of dislocations emitted from the surface, the sharp and straight slip lines indicate that the dislocation motion in the precipitation-strengthened steel was highly planar. Figure 3.5 shows electron channelling contrast (ECC) images after mechanical polishing [41, 42], which exhibit the internal microstructures of the 5%-strained specimen. The line patterns in the ECC images correspond to planar dislocation arrays [11]. Figure 3.5(a) shows an obvious contrast change near grain-boundary triple junctions. The contrast change indicates lattice distortion, which corresponds to stress concentration. It is also noteworthy that nano-scale voids, as shown in Fig. 3.5(b), were observed. In particular, a portion of the nano-voids formed along grain boundaries.

3.3.3. Macroscopic damage evolution behaviour

Figure 3.6 shows an overview of the cross section of the fractured specimen. The black portions correspond to damage, such as cracks and voids. Because the specimen was fractured after necking, the thickness was lowest near the fracture surface and increased

with increasing distance from the fracture surface. The local reduction in thickness Δt was defined as follows:

$$\Delta t = \frac{t_0 - t_l}{t_0} \times 100 \,, \tag{3.4}$$

where t_0 is the initial thickness before the plastic deformation and t_l is the local thickness at the point of observation. The local reduction in thickness corresponds to local plastic strain. Figure 3.7 shows the local reduction in thickness plotted against distance from the fracture surface. The relationship between local reduction in thickness and distance from the fracture surface is classified into three parts: a necked part near the fracture surface, a uniformly deformed part, and a low-strain part near the grip section. The inset shows an enlargement of the portion of the graph corresponding to the necked region of the specimen. As shown in the inset, the relationship between local reduction in thickness and distance from the fracture surface in the necked region was approximated by the second-order polynomial function, which was actually used to estimate local reduction in thickness for the following damage quantification.

Figure 3.8 shows a set of damage quantification results: damage area fraction, number of damages per unit area, and average damage size. In Fig. 3.8(a), except at the value of 21%, where damage was localized due to the presence of a relatively high amount of inclusions, the damage area fraction increases with local reduction in thickness. The reason for the increase in damage area fraction is an increase in the number of damages per unit area, rather than increasing average damage size as demonstrated in Figs. 3.8(b) and (c). Specifically, the average damage size did not increase significantly with reduction in thickness.

3.3.4. Microstructural damage evolution behaviour

Figure 3.9 shows the primary damage initiation site, namely, damage formed at inclusions. Another damage initiation site was grain boundaries. First, the inter-granular damage appeared as nano-voids (Fig. 3.5(b)), and the number of inter-granular damage

increased with plastic strain evolution, as compared with Fig. 3.10(a). Furthermore, the inter-granular damages near grain-boundary triple junctions were observed to be relatively large compared to the other nano-scale inter-granular damages. The inter-granular damage propagated via coalescence along grain boundaries (Fig. 3.10(b)).

When multiple micrometer-scale damages formed in a confined region, the damages coalesced through shear deformation of the ligaments, as shown in Fig. 3.11. It is also noteworthy that some damages propagated along slip lines, as indicated by the white arrow in Fig. 3.11.

3.3.5. Fractographic features

Figure 3.12 shows the fracture surface morphology. The imaging position is the center of the fractured surface. The predominant feature of the fracture surface is dimples (Fig. 3.12 (a)), which indicate the occurrence of ductile failure. Specifically, a major portion of the dimples contains inclusions (Fig. 3.12(b)). In addition to the dimples containing inclusions, we observed two other fractographic features. The first feature was a quasi-cleavage fracture surface, as highlighted by the dashed yellow line in Fig. 3.12(c). The second feature was nano-scale dimples without inclusions, as highlighted by the dashed white line.

3.4 Discussion

3.4.1. Damage initiation mechanism

As average behaviours, the number of damages per unit area showed a clear trend against plastic strain evolution (Fig. 3.8(b)), and the average damage size did not (Fig. 3.8(c)). These facts indicate that damage initiation behaviour that controls number of damage is primarily important compared to damage growth, before occurrence of unstable damage growth. Also, note that the number of damages per unit area near the fracture surface was lower than that of the region slightly distant from the fracture surface, which implies that the number of damages was decreased by damage coalescence and

growth to failure (e.g., Fig. 3.10(b) and Fig. 3.11) [43-45]. Therefore, we must first discuss damage initiation mechanisms.

In the present steel, two damage initiation sites were observed: (1) inclusions (Fig. 3.9) and (2) grain boundaries (Fig. 3.10) [46, 47]. Specifically, the inclusions were the primary damage initiation site, which is consistent with the fractographic feature, i.e., most dimples contained inclusions (Fig. 3.12(b)). The inter-granular damage remained nano-size before damage coalescence, and its number increased on the specific grain boundaries (Fig. 3.10(a)). The damage initiation behaviour corresponded to the presence of nano-scale dimples without inclusions (highlighted by the white dashed line in Fig. 3.12(c)). Because the fracture surface contained both features, damage initiation at inclusions and damage initiation at grain boundaries were both significant for final failure.

Additionally, note that the damage initiation occurred even at an early deformation stage (Fig. 3.5(b). In general, ductile damage initiation occurs after necking, because stress triaxiality in a necking portion of the specimen supresses shear deformation [48]. Hydrostatic stress increases instead. The increase in hydrostatic stress causes inclusion/matrix interface cracking, which subsequently forms voids [49]. However, in the present steel, remarkable damage evolution occurs even in the uniform deformation stage (e.g., Figs. 3.5 and 3.10) and also in the specimen surface (e.g., Fig. 3.9) where the plain stress condition exists. The early damage initiation without the aid of stress triaxiality can be explained in terms of planar slip effects. As schematically shown in Fig. 3.13(a), planar dislocation slip causes stress or plastic strain concentration at microstructures blocking the dislocation motion, which results in damage evolution [50, 51]. Moreover, the lower frequency of cross slip implies a low stress accommodation capability at microstructural stress concentration sites, such as grain-boundary triple junctions [52], where the elastic misfit is maximum (Fig. 3.5(a)). This effect of the planar slip also can assist damage evolution. Assuming that the damage initiation is a stress-controlled phenomenon, the dislocation-planarity-enhanced stress concentration acts as the primary factor causing damage formation. In the present case, the microstructures suffering from the dislocation-planarity-enhanced stress concentrations are inclusions and grain boundaries. In the late deformation stage, group motion of the planar dislocation arrays results in mechanical twinning, which further accelerates the damage initiation [53,

54]. The planar slip-activated multi-mechanisms of damage evolution cause the early damage initiation and the subsequent increase in the number density of damage [55].

Having considered damage initiation, we next discuss damage growth behaviour. Because the average damage size did not increase significantly with strain, we must consider only well-grown damage, rather than the average value. In terms of damage growth, we found two scales: nano-scale growth and micrometer-scale growth as illustrated in Figs. 3.13(a) and (b), respectively [56, 57]. Regarding the nano-scale growth, the inter-granular damage evolves via coalescence of nano-scale voids, and then the damage length increases until near-grain-size (Fig. 3.10(a)) [58-60]. In addition, the planar slip at damage tips results in damage growth along slip lines, which increases the damage length to the micrometer scale, as indicated by the white arrow in Fig. 3.11. After the damage growth from the nano- to the micro-scale, coalescence of micrometer-scale damages occurs through localized shear in the ligaments of the damages, as shown in Fig. 3.11. The localized shear becomes intensive when the frequency of cross slip is low, which is the final role of the planar dislocation slip. The planar slip-assisted nano-scale and micro-scale damage growth results in the quasi-cleavage fracture surface, highlighted by the dashed yellow line in Fig. 3.12(c).

In summary, here, an important difference from the conventional ductile failure mechanism is the significant contribution of planar slip. Specifically, the planar slip acts as a direct cause of damage initiation. Therefore, a considerable amount of damage can initiate in an early deformation stage, even without the help of the macroscopic stress triaxiality effect. Hence, the effect of dislocation planarity in the commercial-grade precipitation-strengthened Fe–Cr–Ni austenitic steel directly affects the plastic deformation limit, and the degree of the dislocation planarity effect is dependent on the inclusion size and density. Moreover, the characteristics associated with damage evolving even in a uniform deformation stage play a disadvantageous role in fatigue for the following three reasons: (1) fatigue damage evolution is a plasticity-induced phenomenon, (2) it occurs without necking of specimens, and (3) it is sensitive to planar slip. Therefore, the detailed role of dislocation planarity on the fatigue of the present steel is additional interest for future work.

3.5. Conclusions

Numerous microstructural damages were observed in the precipitation-strengthened Fe–Cr–Ni steel. The predominant damage initiation site was inclusions. In addition, grain boundaries impinging dislocation slip also acted as nano-scale damage initiation sites, and subsequently the nano-voids grew to micrometer scale via nano-void coalescence and slip plane cracking. These damage evolution mechanisms occurred even in the uniform deformation stage, which indicates that the damage evolution can occur even without the help of macroscopic stress triaxiality, perhaps due to the highly planar slip. The micrometer-scale damages coalesce through localized shear in the ligaments of the damages. These damage evolution behaviours observed in the post-mortem specimen were fully consistent with the fractographic characteristics. The microstructural damage evolution is a cause of the low post-uniform elongation.

References

[1] C. Scott, S. Allain, M. Faral, N. Guelton, The development of a new Fe-Mn-C austenitic steel for automotive applications, Revue de Métallurgie–International Journal of Metallurgy 103(6) (2006) 293-302.

[2] M.O. Speidel, P.J. Uggowitzer, G. Stein, J. Menzel, Austenitic steel alloy, Google Patents, 1998.

[3] V.G. Gavriljuk, B.D. Shanina, H. Berns, Ab initio development of a high-strength corrosion-resistant austenitic steel, Acta Materialia 56(18) (2008) 5071-5082.

[4] P. Kusakin, A. Belyakov, C. Haase, R. Kaibyshev, D.A. Molodov, Microstructure evolution and strengthening mechanisms of Fe–23Mn–0.3 C–1.5 Al TWIP steel during cold rolling, Materials Science and Engineering: A 617 (2014) 52-60.

[5] S.-D. Kim, J.Y. Park, S.-J. Park, J. hoon Jang, J. Moon, H.-Y. Ha, C.-H. Lee, J.-Y. Kang, J.-H. Shin, T.-H. Lee, Direct observation of dislocation plasticity in high-Mn lightweight steel by in-situ TEM, Scientific reports 9(1) (2019) 1-13.

[6] H.-Y. Yu, S.-M. Lee, J.-H. Nam, S.-J. Lee, D. Fabrègue, M.-h. Park, N. Tsuji, Y.-K. Lee, Post-uniform elongation and tensile fracture mechanisms of Fe-18Mn-0.6 C-xAl twinning-induced plasticity steels, Acta Materialia 131 (2017) 435-444.

[7] E.H. Lee, T.S. Byun, J.D. Hunn, K. Farrell, L.K. Mansur, Origin of hardening and deformation mechanisms in irradiated 316 LN austenitic stainless steel, Journal of Nuclear Materials 296(1) (2001) 183-191.

[8] T.H. Lee, C.S. Oh, S.J. Kim, S. Takaki, Deformation twinning in high-nitrogen austenitic stainless steel, Acta Materialia 55(11) (2007) 3649-3662.

[9] K. Habib, M. Koyama, T. Tsuchiyama, H. Noguchi, Dislocation motion at a fatigue crack tip in a high-nitrogen steel clarified through in situ electron channeling contrast imaging, Materials Characterization 158 (2019) 109930.

[10] K. Suzuki, M. Koyama, S. Hamada, K. Tsuzaki, H. Noguchi, Planar slip-driven fatigue crack initiation and propagation in an equiatomic CrMnFeCoNi high-entropy alloy, International Journal of Fatigue 133 (2020) 105418.

[11] M. Koyama, H. Springer, S.V. Merzlikin, K. Tsuzaki, E. Akiyama, D. Raabe, Hydrogen embrittlement associated with strain localization in a precipitation-

hardened Fe–Mn–Al–C light weight austenitic steel, international journal of hydrogen energy 39(9) (2014) 4634-4646.

[12] O. Takakuwa, Y. Ogawa, J. Yamabe, H. Matsunaga, Hydrogen-induced ductility loss of precipitation-strengthened Fe-Ni-Cr-based superalloy, Materials Science and Engineering: A 739 (2019) 335-342.

[13] J. Nakamura, M. Miyahara, T. Omura, H. Semba, M. Wakita, Y. Otome, Degradation of fatigue properties in high pressure gaseous hydrogen environment evaluated by cyclic pressurization tests, Procedia Engineering 2(1) (2010) 1235-1241.

[14] R. Oshima, C.M. Wayman, Fine structure in quenched Fe-Al-C steels, Metallurgical Transactions 3(8) (1972) 2163-2169.

[15] M.C. Ha, J.-M. Koo, J.-K. Lee, S.W. Hwang, K.-T. Park, Tensile deformation of a low density Fe–27Mn–12Al–0.8C duplex steel in association with ordered phases at ambient temperature, Materials Science and Engineering: A 586 (2013) 276-283.

[16] D. Raynor, Dislocation Precipitation in γ'-Forming Steels, Metal Science Journal 5(1) (1971) 161-165.

[17] V. Gerold, H. Karnthaler, On the origin of planar slip in fcc alloys, Acta Metallurgica 37(8) (1989) 2177-2183.

[18] S. Heino, B. Karlsson, Cyclic deformation and fatigue behaviour of 7Mo–0.5N superaustenitic stainless steel—slip characteristics and development of dislocation structures, Acta Materialia 49(2) (2001) 353-363.

[19] Z.Y. Liang, W. Huang, M.X. Huang, Suppression of dislocations at high strain rate deformation in a twinning-induced plasticity steel, Materials Science and Engineering: A 628 (2015) 84-88.

[20] T. Michler, J. Naumann, Hydrogen embrittlement of Cr-Mn-N-austenitic stainless steels, International Journal of Hydrogen Energy 35(3) (2010) 1485-1492.

[21] T. Michler, J. Naumann, M. Hock, K. Berreth, M.P. Balogh, E. Sattler, Microstructural properties controlling hydrogen environment embrittlement of cold worked 316 type austenitic stainless steels, Materials Science and Engineering: A 628 (2015) 252-261.

[22] G.P. Tiwari, A. Bose, J.K. Chakravartty, S.L. Wadekar, M.K. Totlani, R.N. Arya, R.K. Fotedar, A study of internal hydrogen embrittlement of steels, Materials Science and Engineering: A 286(2) (2000) 269-281.

[23] R.G. Davies, Hydrogen embrittlement of dual-phase steels, Metallurgical Transactions A 12(9) (1981) 1667-1672.

[24] M. Koyama, E. Akiyama, K. Tsuzaki, Hydrogen embrittlement in a Fe–Mn–C ternary twinning-induced plasticity steel, Corrosion Science 54 (2012) 1-4.

[25] S. Chen, M. Zhao, L. Rong, Hydrogen-induced cracking behavior of twin boundary in γ′ phase strengthened Fe−Ni based austenitic alloys, Materials Science and Engineering: A 561 (2013) 7-12.

[26] S. Chen, M. Zhao, L. Rong, Role of γ′ characteristic on the hydrogen embrittlement susceptibility of Fe–Ni–Cr alloys, Corrosion Science 101 (2015) 75-83.

[27] P. Hicks, C. Altstetter, Internal hydrogen effects on tensile properties of iron-and nickel-base superalloys, Metallurgical Transactions A 21(1) (1990) 365-372.

[28] Z. Guo, M. Zhao, C. Li, S. Chen, L. Rong, Mechanism of hydrogen embrittlement in a gamma-prime phase strengthened Fe–Ni based austenitic alloy, Materials Science and Engineering: A 555 (2012) 77-84.

[29] S. Chen, M. Zhao, L. Rong, Effect of grain size on the hydrogen embrittlement sensitivity of a precipitation strengthened Fe–Ni based alloy, Materials Science and Engineering: A 594 (2014) 98-102.

[30] H.D. Carlton, A. Haboub, G.F. Gallegos, D.Y. Parkinson, A.A. MacDowell, Damage evolution and failure mechanisms in additively manufactured stainless steel, Materials Science and Engineering: A 651 (2016) 406-414.

[31] D. Fabrègue, C. Landron, O. Bouaziz, E. Maire, Damage evolution in TWIP and standard austenitic steel by means of 3D X ray tomography, Materials Science and Engineering: A 579 (2013) 92-98.

[32] D.-F. Li, C.M. Davies, S.-Y. Zhang, C. Dickinson, N.P. O'Dowd, The effect of prior deformation on subsequent microplasticity and damage evolution in an austenitic stainless steel at elevated temperature, Acta Materialia 61(10) (2013) 3575-3584.

[33] T. Magnin, L. Coudreuse, J.M. Lardon, A quantitative approach to fatigue damage evolution in FCC and BCC stainless steels, Scripta Metallurgica 19(12) (1985) 1487-1490.

[34] C. Tasan, J. Hoefnagels, M. Geers, Identification of the continuum damage parameter: An experimental challenge in modeling damage evolution, Acta Materialia 60(8) (2012) 3581-3589.

[35] M. Koyama, C.C. Tasan, E. Akiyama, K. Tsuzaki, D. Raabe, Hydrogen-assisted decohesion and localized plasticity in dual-phase steel, Acta Materialia 70 (2014) 174-187.

[36] T. Kaneko, M. Koyama, T. Fujisawa, K. Tsuzaki, Combined multi-scale analyses on strain/damage/microstructure in steel: Example of damage evolution associated with ε-martensitic transformation, ISIJ International 56(11) (2016) 2037-2046.

[37] J.A. Brooks, A.W. Thompson] Microstructure and hydrogen effects on fracture in the alloy A-286, Metallurgical Transactions A 24(9) (1993) 1983-1991.

[38] M. Koyama, T. Kaneko, T. Sawaguchi, K. Tsuzaki, Microstructural damage evolution and arrest in binary Fe–high-Mn alloys with different deformation temperatures, International Journal of Fracture 213(2) (2018) 193-206.

[39] T. Kumamoto, M. Koyama, K. Sato, K. Tsuzaki, Evolution of quasi-brittle hydrogen-assisted damages in a dual-phase steel, Materials transactions 60(11) (2019) 2368-2377.

[40] K. Suzuki, M. Koyama, H. Noguchi, Small fatigue crack growth in a high entropy alloy, Procedia Structural Integrity 13 (2018) 1065-1070.

[41] I. Gutierrez-Urrutia, S. Zaefferer, D. Raabe, Electron channeling contrast imaging of twins and dislocations in twinning-induced plasticity steels under controlled diffraction conditions in a scanning electron microscope, Scripta Materialia 61(7) (2009) 737-740.

[42] S. Zaefferer, N.-N. Elhami, Theory and application of electron channelling contrast imaging under controlled diffraction conditions, Acta Materialia 75 (2014) 20-50.

[43] A.A. Benzerga, J.-B. Leblond, Ductile Fracture by Void Growth to Coalescence, in: H. Aref, E.v.d. Giessen (Eds.), Advances in Applied Mechanics, Elsevier2010, pp. 169-305.

[44] T. Pardoen, J.W. Hutchinson, An extended model for void growth and coalescence, Journal of the Mechanics and Physics of Solids 48(12) (2000) 2467-2512.

[45] X. Gao, J. Kim, Modeling of ductile fracture: Significance of void coalescence, International Journal of Solids and Structures 43(20) (2006) 6277-6293.

[46] H.U. Hong, B.S. Rho, S.W. Nam, A study on the crack initiation and growth from δ-ferrite/γ phase interface under continuous fatigue and creep-fatigue conditions in type 304L stainless steels, International Journal of Fatigue 24(10) (2002) 1063-1070.

[47] A. Stratulat, J.A. Duff, T.J. Marrow, Grain boundary structure and intergranular stress corrosion crack initiation in high temperature water of a thermally sensitised austenitic stainless steel, observed in situ, Corrosion Science 85 (2014) 428-435.

[48] K.J. Kurzydlowski, R.A. Varin, W. Zielinski, In situ investigation of the early stages of plastic deformation in an austenitic stainless steel, Acta Metallurgica 32(1) (1984) 71-78.

[49] J.R. Rice, D.M. Tracey, On the ductile enlargement of voids in triaxial stress fields∗, Journal of the Mechanics and Physics of Solids 17(3) (1969) 201-217.

[50] Z. Shen, R. Wagoner, W. Clark, Dislocation and grain boundary interactions in metals, Acta metall. 36(12) (1988) 3231-3242.

[51] K. Nibur, B. Somerday, D. Balch, C. San Marchi, The role of localized deformation in hydrogen-assisted crack propagation in 21Cr–6Ni–9Mn stainless steel, Acta Materialia 57(13) (2009) 3795-3809.

[52] T. Tsuru, Y. Kaji, T. Tsukada, Y. Shibutani, Atomistic Simulations of Stress Concentration and Dislocation Nucleation at Grain Boundaries, Progress in Nuclear Science and Technology 2 (2011) 20-23.

[53] P. Müllner, C. Solenthaler, P. Uggowitzer, M. Speidel, Brittle fracture in austenitic steel, Acta metallurgica et materialia 42(7) (1994) 2211-2217.

[54] M. Koyama, E. Akiyama, K. Tsuzaki, D. Raabe, Hydrogen-assisted failure in a twinning-induced plasticity steel studied under in situ hydrogen charging by electron channeling contrast imaging, Acta Materialia 61(12) (2013) 4607-4618.

[55] Z.G. Zhou, H. Kuwamura, A. Nishida, Effect of micro voids on stress triaxiality-plastic strain states of notched steels, Procedia Engineering 10 (2011) 1433-1439.

[56] P.S. Volegov, D.S. Gribov, P.V. Trusov, Damage and fracture: Review of experimental studies, Physical Mesomechanics 19(3) (2016) 319-331.

[57] M. Salviato, M. Zappalorto, M. Quaresimin, Plastic Yielding Around Nanovoids, Procedia Engineering 10 (2011) 3316-3321.

[58] S. Kobayashi, T. Inomata, H. Kobayashi, S. Tsurekawa, T. Watanabe, Effects of grain boundary- and triple junction-character on intergranular fatigue crack nucleation in polycrystalline aluminum, Journal of Materials Science 43(11) (2008) 3792-3799.

[59] G.S. Was, Grain-boundary chemistry and intergranular fracture in austenitic nickel-base alloys. A review, Corrosion 46(4) (1990) 319-330.

[60] S.K. Banerji, C.J. McMahon, H.C. Feng, Intergranular fracture in 4340-type steels: Effects of impurities and hydrogen, Metallurgical Transactions A 9(2) (1978) 237-247.

List of tables and figures

Table 3.1. Chemical composition of the steel used (wt. %).

C	Si	Mn	P	S	Ni	Cr	Mo	V	Al	B	Ti
0.05	0.12	0.11	0.006	0.001	24.16	13.76	1.11	0.34	0.17	0.0041	2.04

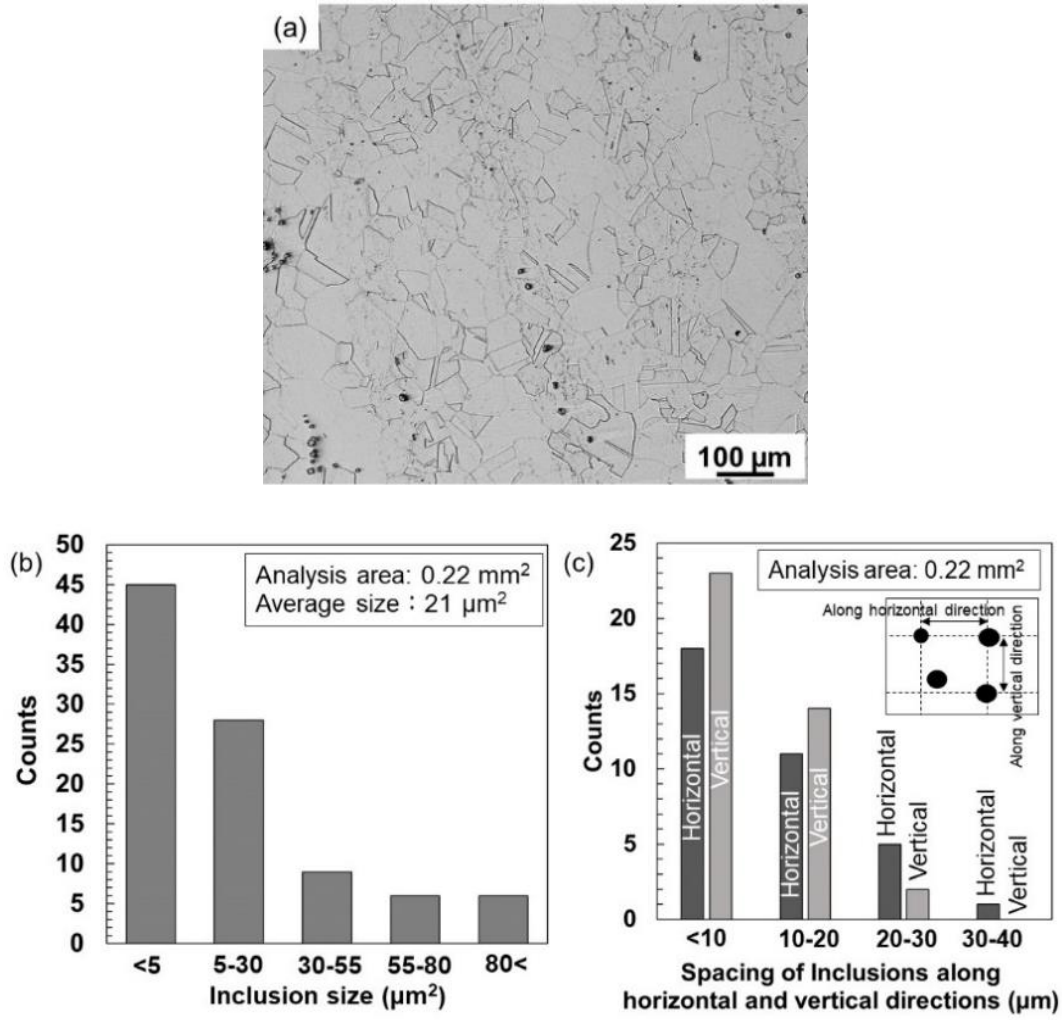

Fig. 3.1. (a) Optical micrograph of the steel before the tensile test. (b) Size (area) and (c) spacing distributions of inclusions.

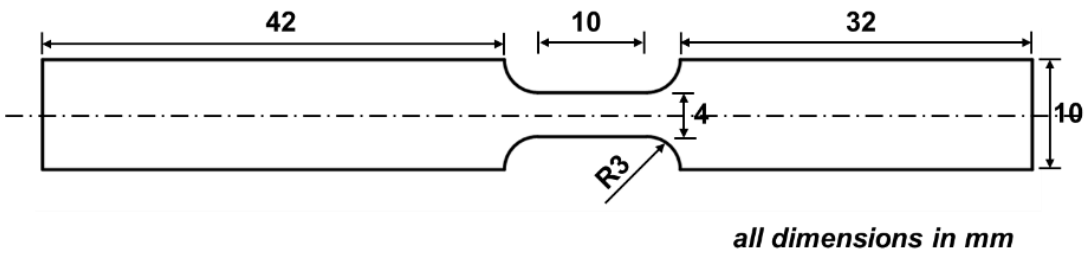

Fig. 3.2. Tensile specimen geometry.

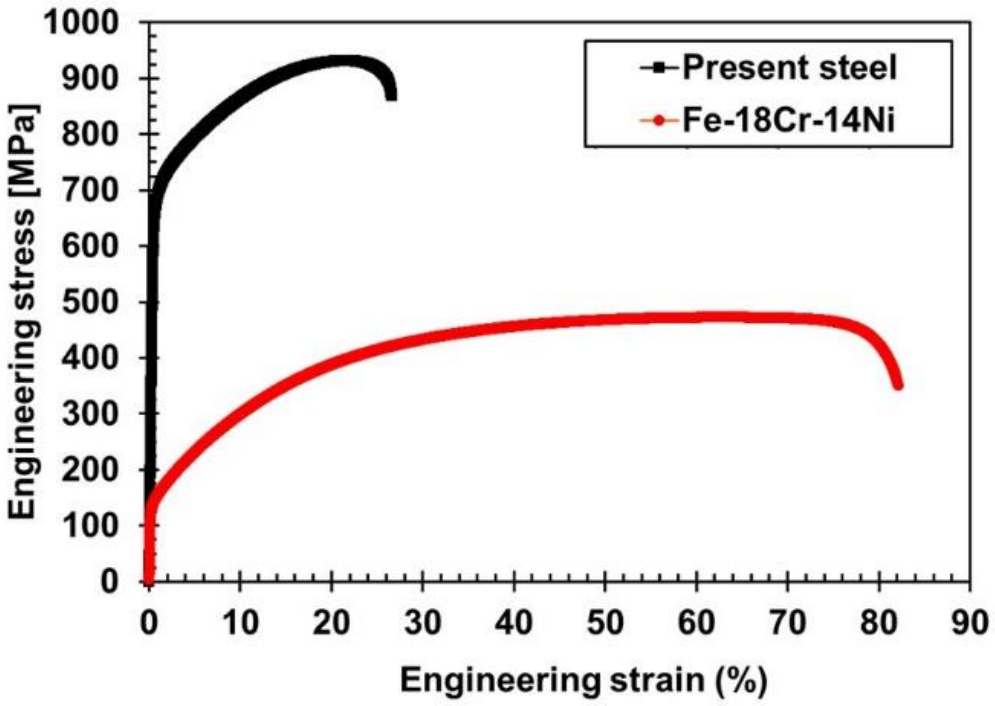

Fig. 3.3. Engineering stress–strain curves.

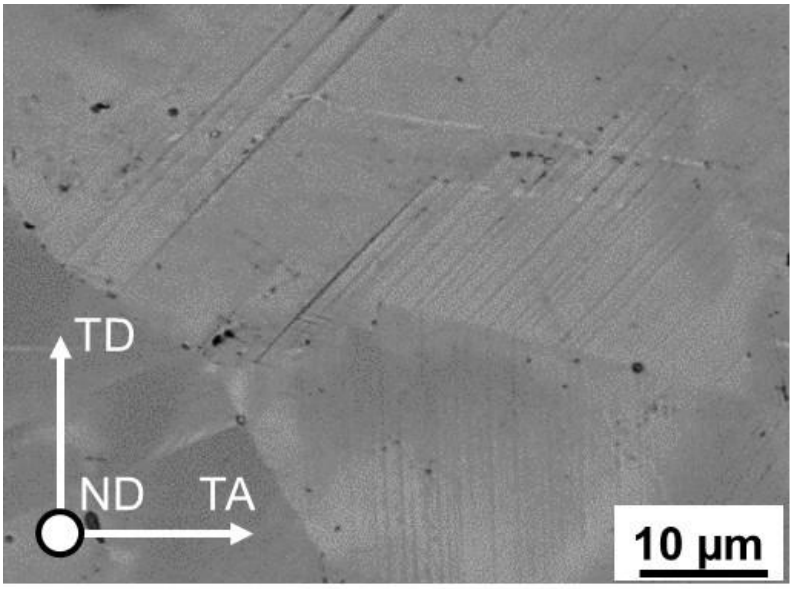

Fig. 3.4. Surface relief of the specimen after 5% straining. ND: Normal direction of the tensile specimen. TA: Tensile axis. TD: Transverse direction. This image shows the surface topography.

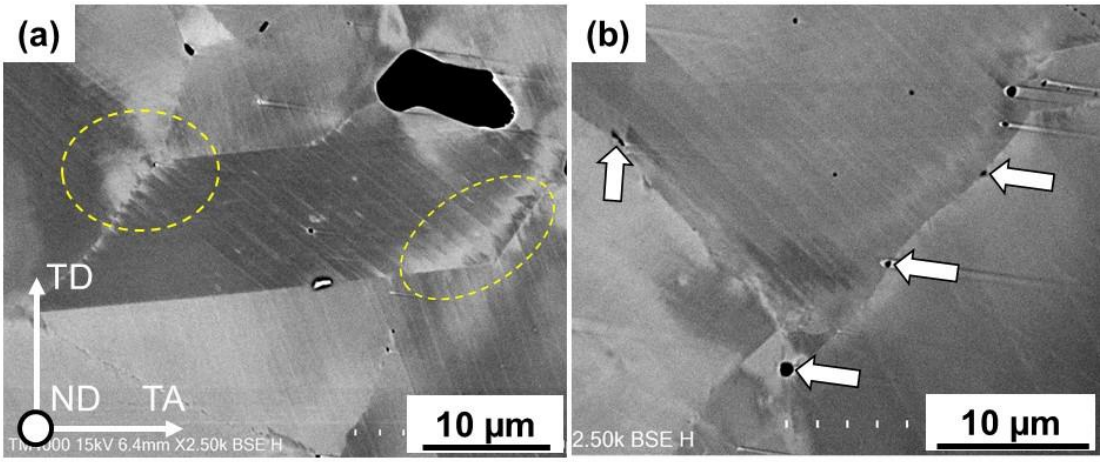

Fig. 3.5. ECC image showing planar dislocation microstructure at 5% strain after mechanical polishing. (a) Planar dislocation array and associated stress concentration around grain-boundary triple junctions, as highlighted by the dashed yellow circles. (b) Formation of nano-voids, particularly on grain boundaries, as indicated by the white arrows. This is an ECC image of the polished surface.

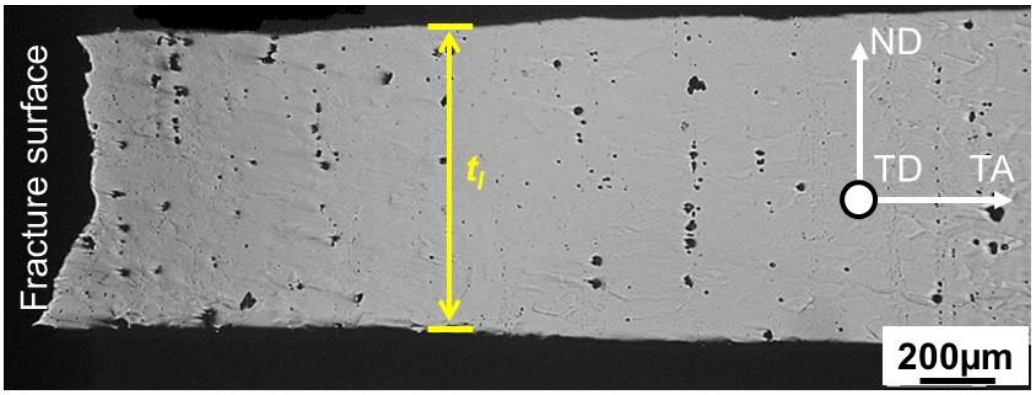

Fig. 3.6. Overview of the fractured specimen containing numerous damages.

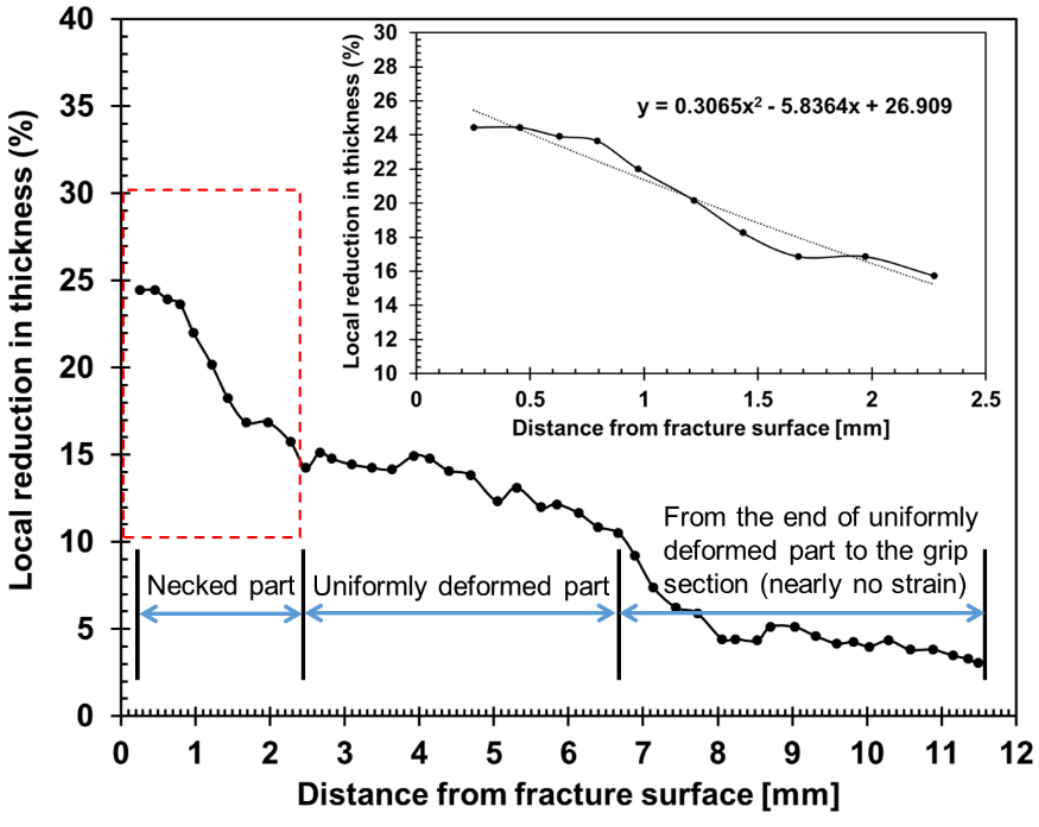

Fig. 3.7. Local reduction in thickness plotted against horizontal distance from the central point of the fracture surface.

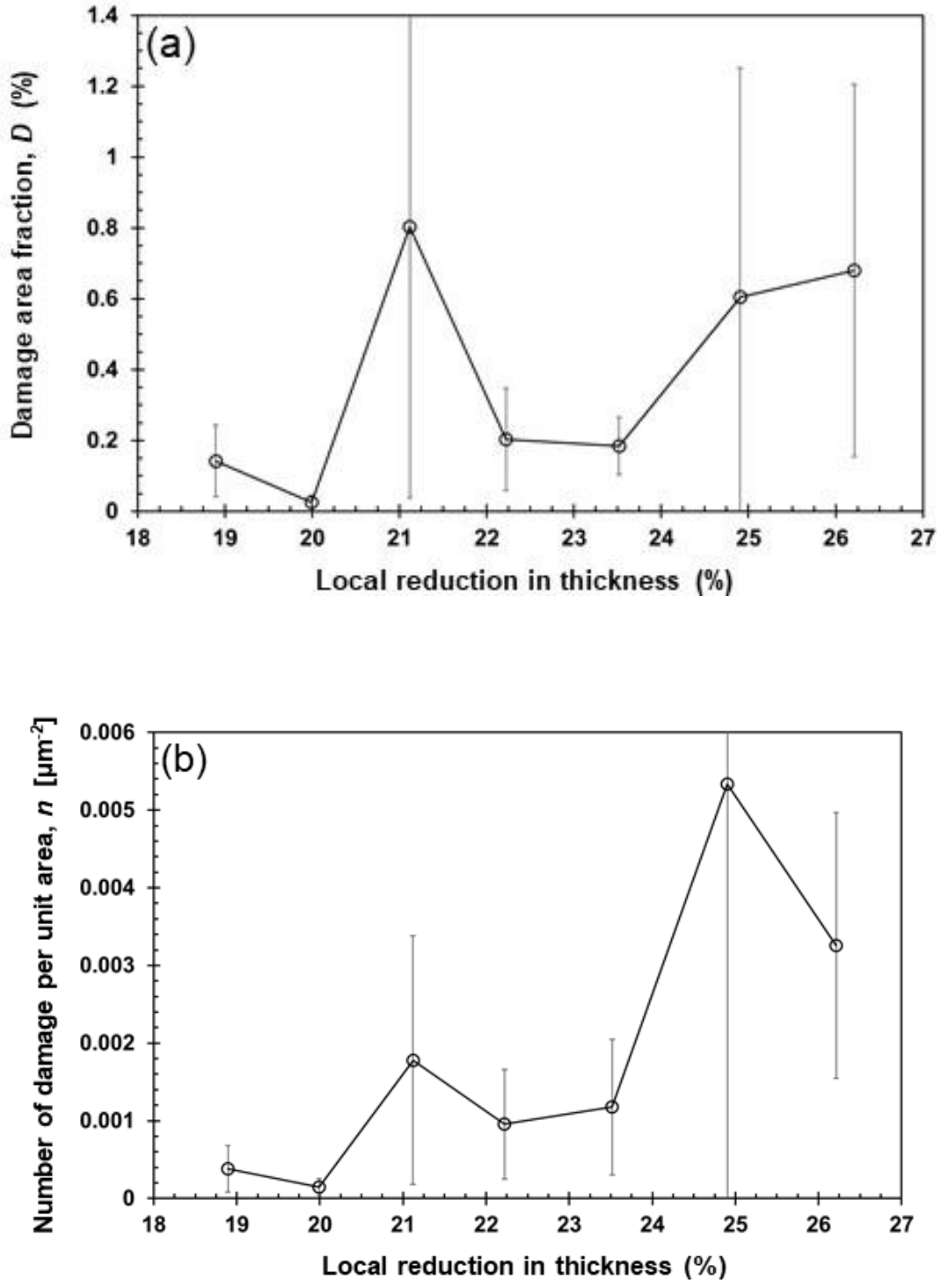

Fig. 3.8. Damage evolution curves of (a) damage area fraction, (b) number of damage per unit area, and (c) average damage size.

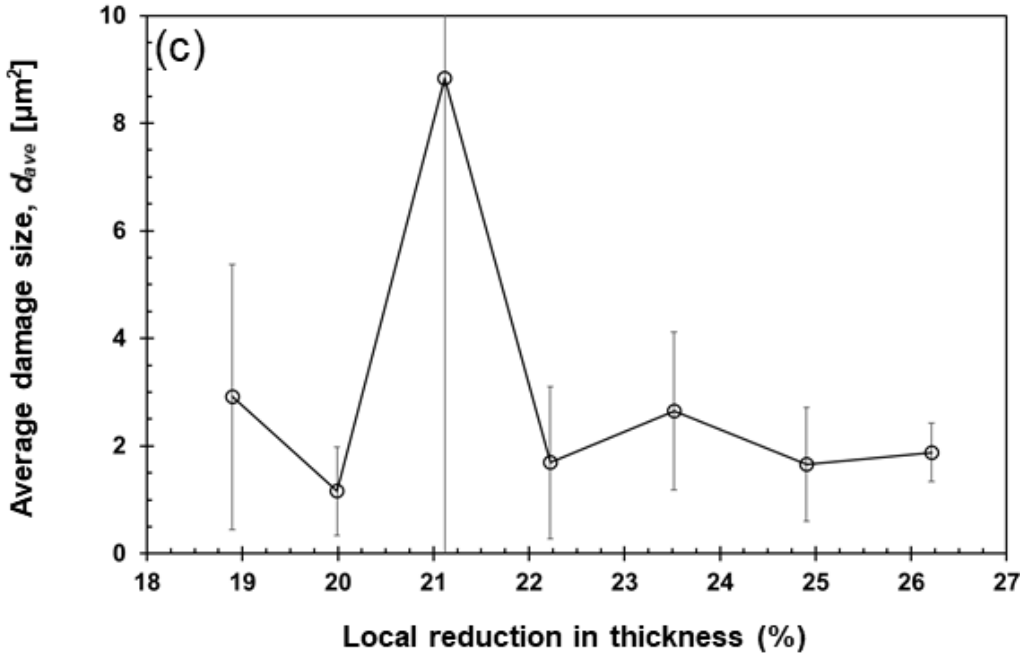

Fig. 3.8. Damage evolution curves of (a) damage area fraction, (b) number of damage per unit area, and (c) average damage size. (continued)

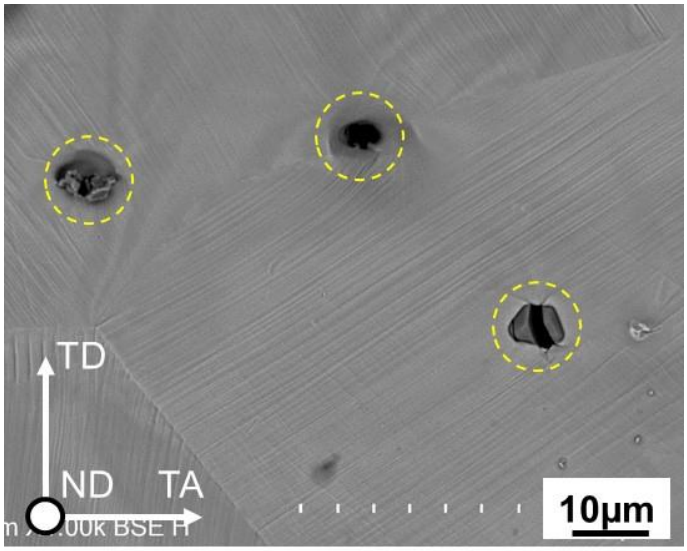

Fig. 3.9. Damage initiation from inclusions, observed at a distance of 5.25 mm from the fracture surface. The dashed circles highlight the damages at the inclusions. This image shows the surface topography.

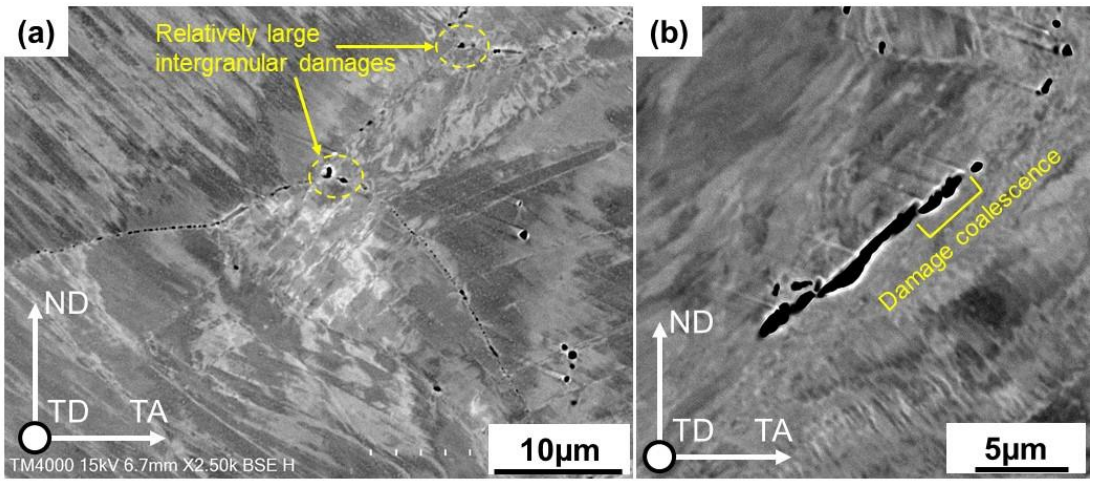

Fig. 3.10. (a) Nano-void formation and (b) coalescence along grain boundaries, observed in the uniformly deformed region of the fractured specimen. This is an ECC image of the polished surface.

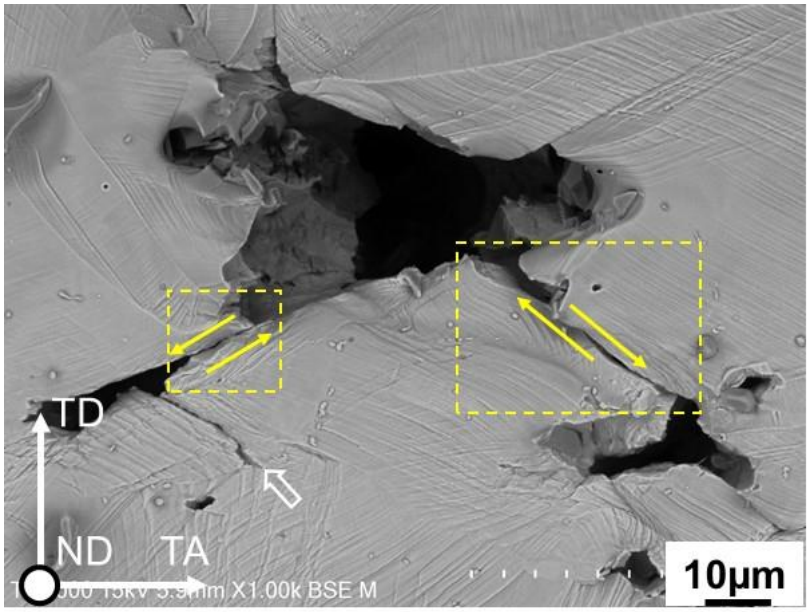

Fig. 3.11. Coalescence of damages via shear deformation (highlighted by the dashed yellow squares) and damage growth along slip lines (indicated by the white arrow.). This image was taken on the as-deformed surface at a distance of 1.06 mm from the fracture surface. The yellow arrows indicate shear deformation of the ligaments between damages. This image shows the surface topography.

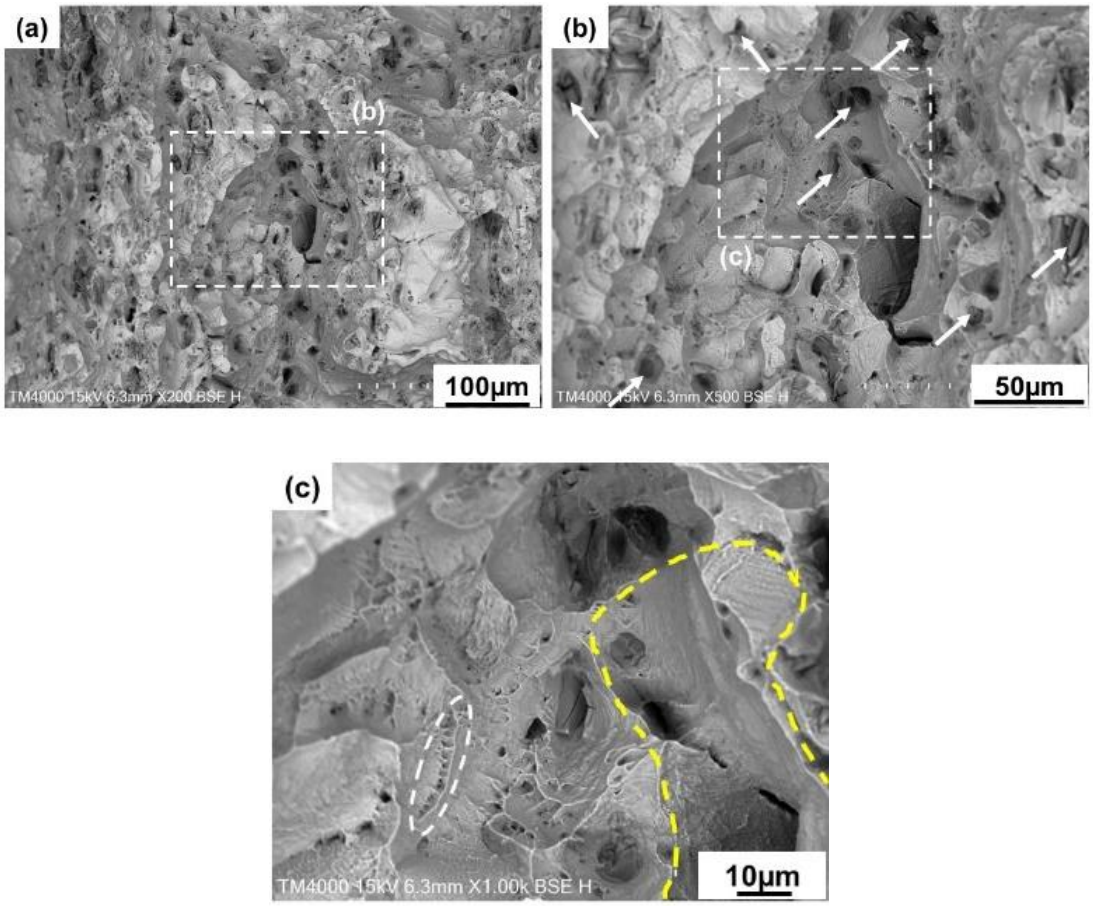

Fig. 3.12. (a) Low-magnification fractograph and (b, c) higher magnifications of the areas shown by dashed white boxes. The white arrows in (b) indicate inclusions in dimples.

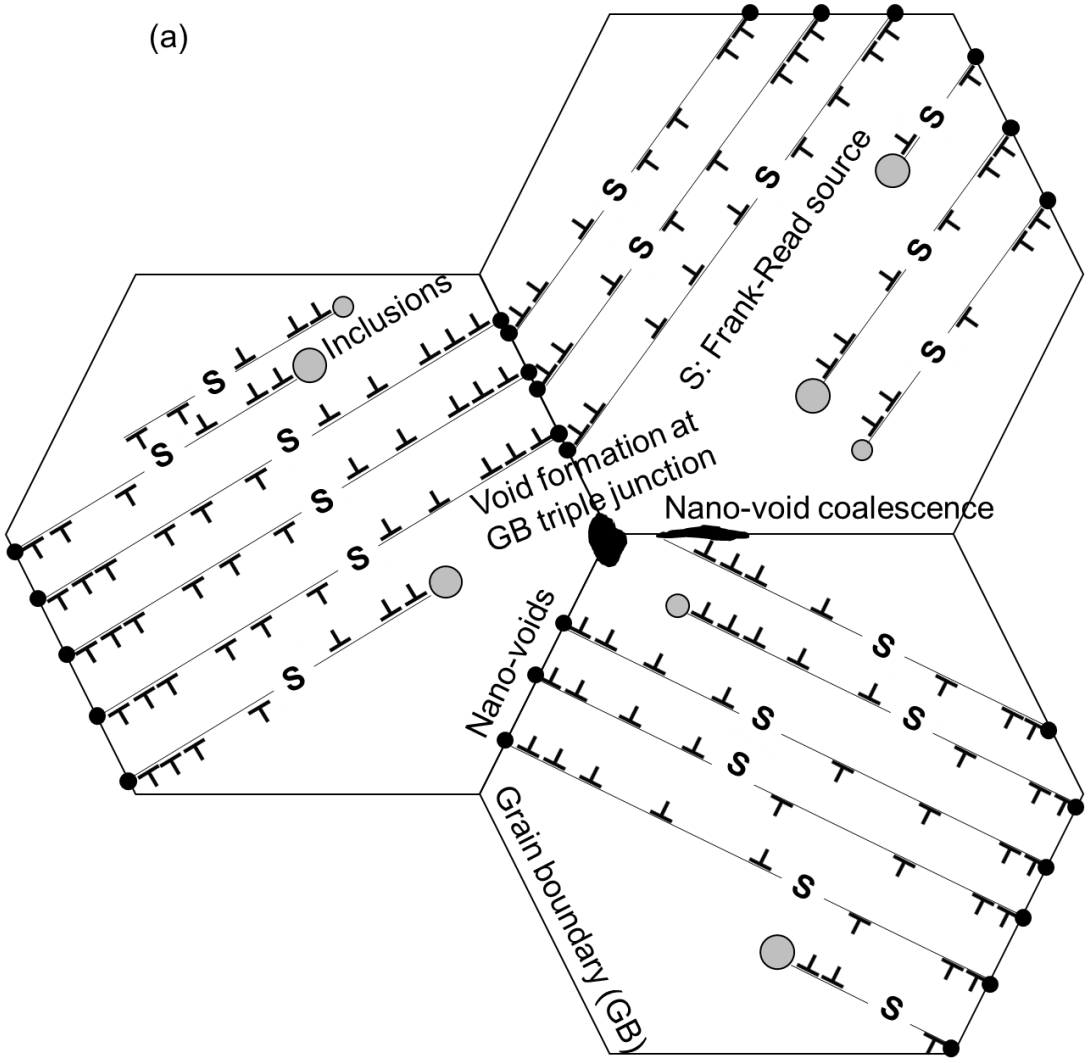

Fig. 3.13. Schematic of damage evolution mechanisms: (a) dislocation pile-up and intergranular nano-void formation/coalescence and (b) damage initiation at inclusions, slip plane cracking, and micrometer-scale damage coalescence. The dislocation emission is from the frank-reid source represented by S.

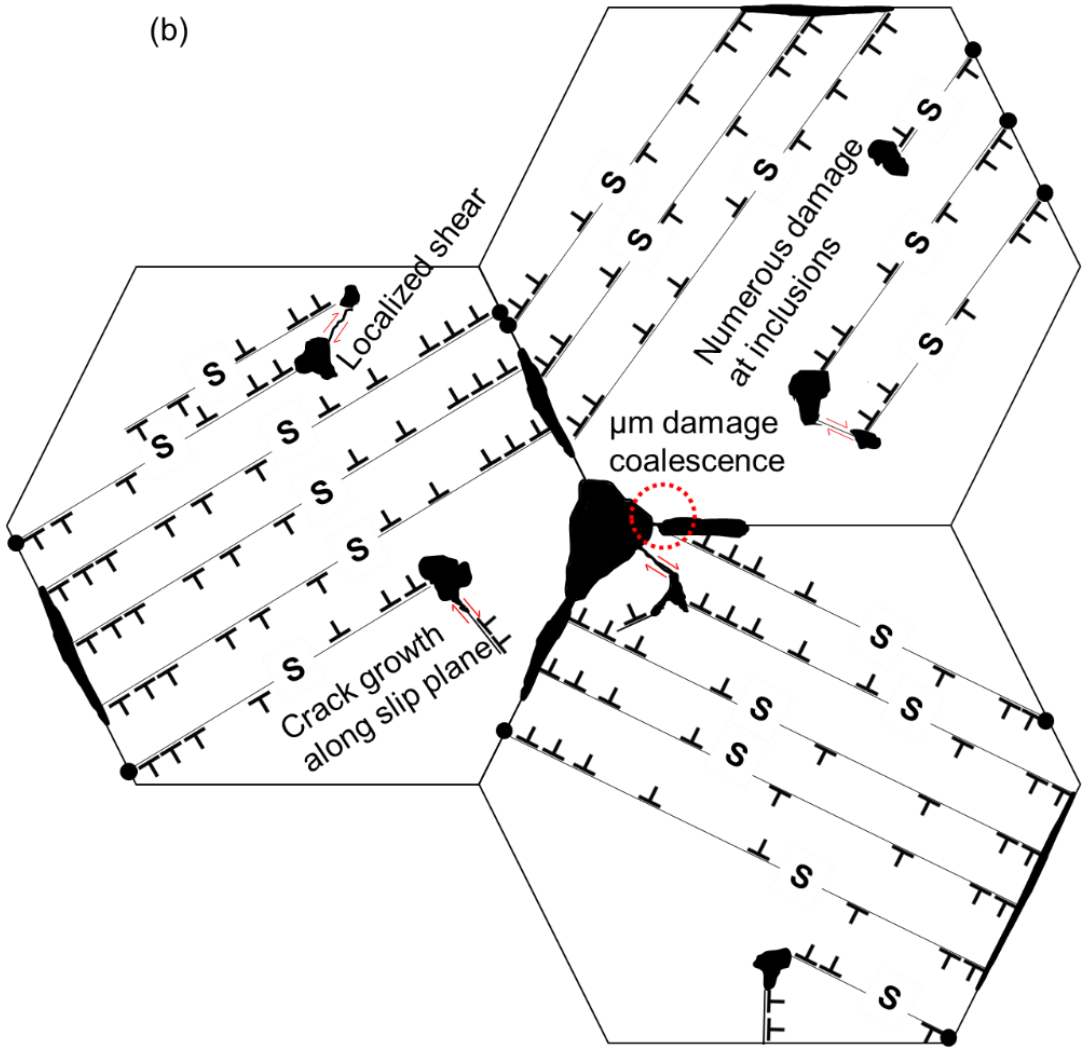

Fig. 3.13. Schematic of damage evolution mechanisms: (a) dislocation pile-up and intergranular nano-void formation/coalescence and (b) damage initiation at inclusions, slip plane cracking, and micrometer-scale damage coalescence. The dislocation emission is from the frank-reid source represented by S. (continued)

Chapter 4 Effects of hydrogen content that alter damage evolution mechanisms in a precipitation-strengthened Fe-Cr-Ni steel

4.1. Introduction

Austenitic steels have been used for hydrogen-energy-related infrastructures, because of their resistance to hydrogen embrittlement [1-3]. Specifically, the austenite phase intrinsically exhibits low diffusivity of hydrogen [4, 5], which suppresses hydrogen segregation and hydrogen effects on dislocation motion [6, 7]. However, the strength of austenitic steels is relatively low compared with those of other commercially available steels, such as martensitic steels.

Given this background, precipitation-strengthened austenitic steels are being promoted as the next generation structural materials for the hydrogen environment [8-10]. For instance, the Fe-Cr-Ni precipitation-strengthened steel SUH 660, whose strength is almost twice than of its solution-treated counterpart because of the presence of γ′ [Ni_3(Al,Ti)] precipitates [11], shows high strength as well as high resistance to hydrogen embrittlement [12]. However, there is a significant loss in the ductility of these steels when they are subjected to hydrogen charging for longer durations at elevated temperatures [13-15]. Although SUH 660 shows high resistance to embrittlement by external hydrogen at slow-strain-rate tensile conditions [16-18], it should also be note that solution-treated SUH 660 shows even higher resistance to hydrogen embrittlement than its precipitation-strengthened counterpart [19]. Hence, understanding the underlying mechanism of the slight hydrogen-induced loss in ductility, which is associated with precipitation, is important for the development of high-strength hydrogen-resistant steels for even more severe hydrogen environments.

To understand the effects of precipitates on the susceptibility of austenitic steels to hydrogen embrittlement, we must first elucidate the evolution of the microstructural defects. In the previous studies [20, 21], we found that damages such as voids and cracks formed even before necking, which is related to planar dislocation glide and associated

deformation twinning [22-24]. The dislocation planarity has been reported to arise from a high amount of γ′ phase [25, 26] and thus the ease of microstructural damage evolution is an unavoidable phenomenon in the precipitation-strengthened austenitic steels. In a commercial Fe-Cr-Ni precipitation-strengthened steel without hydrogen effects, the predominant damage initiation site is inclusions, with the grain boundaries acting as secondary damage initiation site [21, 24]. The growth and coalescence of the damages, which are facilitated by planar dislocation glide, causes the final failure [21]. Hydrogen has been reported to change the predominant damage initiation site from inclusion to grain boundary [24, 27, 28]. Many previous researchers reported that the faceted fracture surface coincides with the grain boundary [29-31].

According to the previous studies, the plasticity-induced nm-scale damage formation on grain boundaries occur in both the cases with and without hydrogen charging [21, 24]. The primary effect of hydrogen is to accelerate occurrence of the nm-scale inter-granular damage [32]. Subsequently, hydrogen causes brittle-like damage growth from nm to μm size, which does not appear in uncharged specimen [33-36]. Therefore, the hydrogen embrittlement susceptibility is dependent on a balance of resistance to the formation of plasticity-induced nm-size damage, and subsequent brittle-like growth to μm-size on grain boundaries. Since brittleness generally increases with hydrogen content, the balance of the plasticity-induced and brittleness-driven damage resistance is also considered to be dependent on the hydrogen content. The change in damage evolution behaviour with hydrogen content is important to estimate the risk of hydrogen embrittlement in practical structures. Accordingly, in this paper, we aim to clarify the hydrogen effects on damage initiation and growth in a commercial precipitation-strengthened Fe-Cr-Ni austenitic steel with different hydrogen contents.

4.2 Experimental procedure

4.2.1. Material and specimen

The present study deals with a commercial grade γ′-precipitation-strengthened austenitic steel, *i.e*. SUH 660. We received the material in the form of a cylindrical bar with a diameter of 120 mm. Table 4.1 shows the chemical composition of the material

used [21]. The as-received material had already been aged at 1003 K for 16 h and then air cooled, which thereby contains γ′ [$Ni_3(Al,Ti)$] precipitates. Figure 4.1(a) shows the microstructure in the as-received condition, obtained by scanning electron microscopy (SEM) operated at an acceleration voltage of 15 kV. A significant amount of coarse particles, which were inclusions/precipitates, were observed. The chemical composition of the particles was analyzed by energy dispersive X-ray spectroscopy (EDS) operated at 20 kV. Table 4.2 lists the chemical composition obtained by a point analysis at a location indicated in Fig. 4.1(b). According to the measured composition, the particle is (Ti, Mo)-C. The coarse carbide particles have been reported in commercial nickel alloys as well [37]. The elemental distribution is homogeneous in the particle as shown in Figs. 4.1(c-h). The average grain size was measured to be 58 ± 4 μm [21].

4.2.2. Hydrogen charging and mechanical testing

Three specimens with different hydrogen charging conditions were tensile-tested; two were hydrogen-charged, and one was uncharged. The specimens were electrochemically charged with hydrogen for 1 week in a 3% NaCl aqueous solution containing 3 g/L NH_4SCN. The cathodic current densities for the two specimens were set to be 1 and 10 A/m^2, respectively.

Dog-bone-shaped plate specimens with gauge dimensions of 10 mm in length, 4 mm in width and 1.2 mm in thickness were fabricated by electric discharge machining. Tensile tests were conducted at room temperature (296 K) with an initial strain rate of 10^{-4} s^{-1}. After test completion, a part of the fractured specimen was preserved in a refrigerator to avoid hydrogen desorption. This part could be used later for thermal desorption spectroscopy (TDS) studies to measure hydrogen content. The other part was used for further microscopic studies like fractography and microstructural characterization. Amount of hydrogen content in the specimen was measured by TDS using a quadrupole mass spectrometer. The sample was heated from room temperature to 1073 K at a heating rate of 200 K/h for hydrogen desorption and continuous measurement of hydrogen evolved.

4.2.3. Microstructure characterization

Microstructural analysis was carried out after the tensile test with the aid of optical microscopy and SEM. For characterising internal damage and microstructure, the specimen was cut in the transverse plane and mechanically polished until a mirror finish using colloidal silica with a particle size of 60 nm. Damages such as cracks and voids observed in the images were quantified as number of damage per unit area (n). This was obtained by dividing total number of damages with entire observation area. The number of damage per unit area was then plotted against the local reduction in thickness of the fractured specimen.

4.3 Results

4.3.1. Hydrogen uptake and its effect on mechanical behaviour

Figure 4.2 shows the TDS profiles of the specimen hydrogen-charged at current densities of 1 and 10 A/m^2. Cumulative hydrogen content from ambient temperature to 673 K for the specimens hydrogen charged at 1 and 10 A/m^2 were 8.8 and 66.7 mass ppm, respectively. In austenitic steels hydrogen-charged at ambient temperature, the in-depth distribution of hydrogen is usually non-uniform. The hydrogen diffusion depth from the specimen surface can be estimated by

$$z \cong 1.12\sqrt{Dt} \qquad (4.1)$$

where D is diffusion coefficient and t is hydrogen charging time. D can be obtained from

$$D = D_0 \exp\left(-\frac{Q}{RT}\right) \qquad (4.2)$$

where, D_0: Pre-exponential factor (1.21×10^{-5} m^{2}s^{-1}) [38], Q: Activation energy (63.1 kJmol^{-1}) [38], R: gas constant (8.3145 Jmol^{-1}K^{-1}), T: Absolute temperature.

For the present hydrogen charging condition (t = 6.048 x 10^5 s, T= 296 K), the

hydrogen diffusion depth was estimated to be 8.2 μm. The shows that the hydrogen is localized near the surface.

Figure 4.3 shows engineering stress-strain curves of the uncharged and hydrogen-charged specimens. The hydrogen charging did not cause significant changes in the yield strength and work hardening behaviour, however decreased the elongation. The degree of elongation degradation increased with increasing hydrogen-charging current density.

4.3.2. Damage quantification and surface damage morphology

Figures 4.4(a)-(c) show transverse cross-sectional images of the uncharged and hydrogen-charged specimens. The various small black regions that can be observed along the length of the specimen corresponds to damages such as cracks and voids. As indicated by the red arrows, the number of surface cracks increased by the hydrogen charging and with increasing current density from 1 to 10 A/m^2. On the other hand, as an average value, number of damage per unit area in the specimen interior did not change by the hydrogen charging, irrespective of current density (Fig. 4.5). These facts indicate that hydrogen affects the damage evolution behaviour only near the surface, where hydrogen localizes as analysed in section 4.3.1. Therefore, hereafter we have investigated surface cracks.

With respect to the surface cracks, we first note number of damage, damage morphology, and damage growth behaviour. For uncharged specimen, number of surface damage increased as one move closer to the fracture surface (Figs. 4.6(a)–(c)). As reported in our previous study [21], the primary damage initiation site was coarse carbide, and partially grain boundaries. Two dimensional shape of the damage was mostly square, circular or ellipsoidal. The appearance of the shapes arose from damage tip blunting owing to the plastic deformation of surrounding microstructures (Fig. 4.6(d)).

Hydrogen charging at 1 A/m^2 increased crack initiation probability (Fig. 4.7(a)), and crack coalescence and crack propagation were frequently observed (Fig. 4.7(b)) compared with the uncharged specimen. Furthermore, some cracks retained sharpness of its tip even near the fracture surface (Fig. 4.7(c)). In addition to carbides, grain boundaries also acted as an active initiation site (Fig. 4.7(d)). The cracks grew predominantly into grain interior and partially along grain boundaries as shown in Figs. 4.7(d-f). The crack

growth occurred via repetition of crack blunting and sharp crack growth or coalescence of μm-scale cracks (Figs. 4.7(e, f)). When the crack grew sharply, a slip trace that was nearly parallel to the crack surface was observed near the crack tip as shown in Fig. 4.7(e). It is noteworthy that path of the sharp trans-granular crack growth was aligned 45 degrees with respect to the tensile direction.

The increase in hydrogen charging current density to 10 A/m^2 further increased crack initiation probability and deteriorated capability of crack blunting, irrespective of distance from the fracture surface (Fig. 4.8). As seen in Fig. 4.9, the primary cracking site was grain boundary rather than carbide.

4.3.3. Fractographic features

Figure 4.10 shows the overall view of the fractured surface for the uncharged and hydrogen- charged specimens. Because hydrogen was localized near the surface, brittle-like features in the hydrogen-charged specimens appeared only near the edges of the fracture surfaces. In particular, corner has more affinity for hydrogen therefore the effect of hydrogen appeared most significantly at the corner of the fracture surfaces. Figures 4.11 (a)-(i) show details of the corners of the fracture surfaces with different magnifications. The fracture surface obtained without hydrogen charging was predominantly covered with dimples (Fig. 4.11(a) and (b)). In particular, coarse dimples containing particles (Fig. 4.11(c)), which indicates typical ductile fracture. Fine dimples without particles and quasi-cleavage feature, which was associated with planar-slip-induced damage [21], were also observed as a minor portion of the fracture surface (Fig. 4.11(c)). The hydrogen charging at 1 A/m^2 changed fracture surface morphology from ductile type to brittle-like faceted features (quasi-cleavage fracture) [39], as seen in Figs. 4.11 (d) and (e). The quasi-cleavage fracture surface can be classified into two types: (i) having some line patterns as shown in the inset of Fig. 4.11(f), and (ii) having relatively smooth faceted surface as indicated by arrows in Fig. 4.11(f). Also note that cliffs were observed around the quasi-cleavage fracture regions. With increasing current density to 10 A/m^2, the predominant feature of the fracture surface changed again to inter-granular fracture (Figs. 4.11 (g) and (h)). The inter-granular fracture surface exhibited slip traces (Fig. 4.11(i)).

4.4 Discussion

4.4.1. Mild hydrogen charging condition

The total elongation degraded with increasing current density (Fig. 4.3). According to the fracture surface shown in Figs. 4.11(d-f), the ductility degradation by hydrogen charging at 1 A/m^2 was caused by the occurrence of quasi-cleavage fracture. The quasi-cleavage fracture feature was partially observed in the uncharged specimen as well, which was caused by planar slip. That is, the hydrogen charging at 1 A/m^2 merely assisted the planar-slip-driven quasi-cleavage damage evolution occurring even without hydrogen charging.

The fact that the crack initiation probability significantly increased by the hydrogen charging at 1 A/m^2 (Figs. 4.7(a-c)) indicates that the crack initiation resistance was degraded by the hydrogen uptake. The crack initiation sites in this condition were grain boundaries as well as coarse carbide particles. Here note that two types of quasi-cleavage fracture surfaces were observed, namely, the first type containing line pattern, while the other did not (Fig. 4.11(f)). The cracking of non-metallic portion (carbide) with a size of 10-20 μm (e.g., Fig. 4.1(b)) can result in the quasi-cleavage feature. On the other hand, the presence of line patterns on the other type of quasi-cleavage fracture surface (Fig. 4.11(f)) indicates contribution of plasticity. The plasticity-driven crack initiation has been reported even without hydrogen charging [21], namely, localization of planar slip at microstructural stress concentration sites triggers such cracking mechanism. Specifically, after crack initiation at grain boundaries and relatively small carbides, slip localization occurs at the tiny cracks (Fig. 4.7(d)), which causes planar-slip-driven crack growth in grain interior. The planar slip coupled with hydrogen effects affects both inter-granular and quasi-cleavage crack initiation and growth [40-43].

After considering the crack initiation and slight propagation, we next discuss the crack propagation over the grain size. The cracks, that initiated and subsequently propagated slightly, were arrested via crack tip blunting (Figs. 4.7(e) and (f)). The cracks restarted to propagate via one of two processes. The first type was sharp crack growth that involves slip deformation along the crack tip. The local slip at the crack tip has been reported to assist crack growth particularly when the dislocation planarity was enhanced by the effect

of precipitation [21, 44, 45]. Hydrogen accelerates the slip-induced crack growth in terms of hydrogen-enhanced localized plasticity (HELP) hypothesis [46-48]. The second type was coalescence of blunted cracks. As seen in Fig. 4.7(e), the cracks whose tips had been blunted grew via shear strain localization occurring in between the cracks, which also can be accelerated by HELP [49, 50]. Because of the two crack growth mechanisms, crack size increased before the crack fully blunted unlike the case of uncharged specimen (e.g., Fig. 4.6). Hence, both trans-granular crack initiation and growth from nano to μm scale was related to the planar slip when hydrogen was introduced at 1 A/m^2. Specifically, the planar-slip-driven crack growth has been reported as minor mechanism in the uncharged specimen, and hydrogen enhanced the effect of dislocation planarity, which caused quasi-cleavage fracture and associated deterioration of elongation.

4.4.2. Severe hydrogen charging condition

Although the ductility was monotonically decreased by increasing current density, the damage evolution and associated fracture mode in the specimen hydrogen charged at 10 A/m^2 was totally different from the case of hydrogen charging at 1 A/m^2. A clear difference was found in the fracture surface, namely, intergranular fracture feature was observed (Figs. 4.11(g-i)).

In terms of sub-crack analyses, hydrogen charging at 10 A/m^2 increased crack initiation probability (Fig. 4.8(c)) and sharpness of crack tips (Fig. 4.9). These facts indicate that hydrogen charging at 10 A/m^2 deteriorates both crack initiation resistance and crack arrestability at grain boundaries [51]. According to Takakuwa's study [24], hydrogen-decorated dislocation motion plays a role in the inter-granular crack initiation in the precipitation-strengthened austenitic steel [52-54]. The dislocation motion may deposit hydrogen at the grain boundary during slip transfer through grain boundary because of their weak trapping force [55]. When multiple dislocations pass by grain boundary, a considerable amount of hydrogen is accumulated at the grain boundary. When hydrogen concentration reaches a critical value, cracks initiate and propagate along the grain boundary [56-58]. Additionally, the planar slip and deformation twins that impinged the grain boundaries also assisted the inter-granular crack initiation and propagation [24, 59]. The plasticity-assisted cracking results in slip traces on the inter-granular fracture

surface as shown in Fig. 4.11(f). When the local stress with a specific hydrogen concentration reaches a threshold value, the inter-granular cracking occurs at the weakest grain boundary. Even when crack initiation does not occur at relatively strong grain boundary, the presence of local stress and hydrogen at grain boundary assist the inter-granular crack propagation, when the initiated cracks approaches. Therefore, the crack arrestability at grain boundaries was also deteriorated by the combined effect of plasticity and hydrogen.

Assuming that the strain-dependent local stress and local hydrogen content play the primary roles triggering the hydrogen embrittlement, we can interpret the hydrogen content dependence of the fracture behaviour as indicated in Fig. 4.12. Because of the less plasticity in the non-metallic material, local stress increases with strain by an interaction between dislocation and coarse carbide, which preferentially causes cracking at the interface or in the carbide when hydrogen is not introduced (Fig. 4.6 and previous study [21]). Cracking at grain boundaries can occur only when planar dislocation array and deformation twins evolve after significant plastic straining (Fig. 4.12(a)). On the other hand, when hydrogen is introduced, hydrogen assists both trans-granular and inter-granular cracking, and the cracking behaviour is dependent on hydrogen content. When hydrogen charging condition is mild, e.g. 1 A/m^2 in the present study, hydrogen accelerates occurrence of carbide cracking and subsequent crack growth along slip bands. Only after large plastic straining, the local stress and hydrogen content reaches the critical values via hydrogen-decorated and planar dislocation slip (Fig. 4.12(b)). Therefore, the inter-granular cracking is a minor phenomenon in the mild hydrogen charging condition. When hydrogen charging condition gets severe (e.g., hydrogen charging at 10 A/m^2), local hydrogen content easily reaches the critical value. Accordingly, numerous inter-granular crack initiation and easy crack growth along grain boundaries occur, which thereby caused the intergranular fracture [60].

4.5. Conclusions

Effects of hydrogen content on damage evolution and associated tensile properties were investigated for precipitation-strengthened Fe-Cr-Ni austenitic steel. The hydrogen content was controlled by changing hydrogen-charging current density from 0 to 10 A/m^2

in an aqueous solution of 3% NaCl + 3g/L NH_4SCN. Total elongation degrades with an increase in hydrogen content. In addition, the important finding in this chapter is the change in damage initiation and propagation modes with increasing hydrogen content. For uncharged specimen, the ductile fracture occurred mainly due to cracking at the carbides, and grain boundaries acted as a minor cracking site. The hydrogen charging at 1 A/m^2 accelerated the occurrence of cracking at carbides and grain boundaries, and the cracks propagated along slip bands. Furthermore, the hydrogen charging assisted localized slip-induced crack coalescence as well, which caused quasi-cleavage fracture. When the specimen was charged with hydrogen at 10 A/m^2, grain boundaries acted as the primary site of damage initiation and propagation, which resulted in inter-granular fracture.

References

[1] T. Ogata, Hydrogen Environment Embrittlement Evaluation in Fatigue Properties of Stainless Steel SUS304L at Cryogenic Temperatures, AIP Conference Proceedings, American Institute of Physics, 2010, pp. 25-32.

[2] T. Ogata, Influence of high pressure hydrogen environment on tensile and fatigue properties of stainless steels at low temperatures, AIP Conference Proceedings, American Institute of Physics, 2012, pp. 39-46.

[3] M. Koyama, C.C. Tasan, K. Tsuzaki, Overview of metastability and compositional complexity effects for hydrogen-resistant iron alloys: Inverse austenite stability effects, Engineering Fracture Mechanics (2019).

[4] L. Tsay, S. Yu, R.-T. Huang, Effect of austenite instability on the hydrogen-enhanced crack growth of austenitic stainless steels, Corrosion science 49(7) (2007) 2973-2984.

[5] K. Hirata, S. Iikubo, M. Koyama, K. Tsuzaki, H. Ohtani, First-principles study on hydrogen diffusivity in BCC, FCC, and HCP iron, Metallurgical and Materials Transactions A 49(10) (2018) 5015-5022.

[6] J. Yamabe, T. Awane, S. Matsuoka, Investigation of hydrogen transport behavior of various low-alloy steels with high-pressure hydrogen gas, international journal of hydrogen energy 40(34) (2015) 11075-11086.

[7] J. Yamabe, O. Takakuwa, H. Matsunaga, H. Itoga, S. Matsuoka, Hydrogen diffusivity and tensile-ductility loss of solution-treated austenitic stainless steels with external and internal hydrogen, International Journal of Hydrogen Energy 42(18) (2017) 13289-13299.

[8] A. Thompson, Ductility Losses in Austenitic Stainless Steels Caused by Hydrogen, Hydrogen in Metals, ed, IM Berstein, AW Thompson, ASM, Cleveland (1974) 91.

[9] J. Holbrook, A. West, Hydrogen effect in materials, ed. by IM Bernstein and AW Thompson, AIME, Warrendale, Pa 655 (1981).

[10] C. San Marchi, Hydrogen embrittlement of stainless steels and their welds, 2012, pp. 592-623.

[11] A. Thompson, J. Brooks, The mechanism of precipitation strengthening in an iron-base superalloy, Acta Metallurgica 30(12) (1982) 2197-2203.

[12] P. Ordin, Safety Standard for Hydrogen and Hydrogen Systems: Guidelines for Hydrogen System Design, Materials Selection, Operations, Storage, and Transportation. Office of Safety and Mission Assurance, National Aeronautics and Space Administration, Washington DC (1997).

[13] A.W. Thompson, J.A. Brooks, Hydrogen performance of precipitation-strengthened stainless steels based on A-286, Metallurgical Transactions A 6(7) (1975) 1431.

[14] W.W. Gerberich, Y. Chen, Hydrogen-controlled cracking—An approach to threshold stress intensity, Metallurgical Transactions A 6(2) (1975) 271.

[15] J.A. Brooks, A.W. Thompson] Microstructure and hydrogen effects on fracture in the alloy A-286, Metallurgical Transactions A 24(9) (1993) 1983-1991.

[16] M. Wang, E. Akiyama, K. Tsuzaki, Effect of hydrogen on the fracture behavior of high strength steel during slow strain rate test, Corrosion science 49(11) (2007) 4081-4097.

[17] O. Takakuwa, J. Yamabe, H. Matsunaga, Y. Furuya, S. Matsuoka, Comprehensive understanding of ductility loss mechanisms in various steels with external and internal hydrogen, Metallurgical and Materials Transactions A 48(11) (2017) 5717-5732.

[18] E. Martínez-Pañeda, Z.D. Harris, S. Fuentes-Alonso, J.R. Scully, J.T. Burns, On the suitability of slow strain rate tensile testing for assessing hydrogen embrittlement susceptibility, Corrosion Science 163 (2020) 108291.

[19] N. Tajima, A. Orita, T. Matsuo, Y. Yamaguchi, J. Yamabe, S. Matsuoka, Effect of Internal Hydrogen on Tensile Properties of Iron-Based Superalloy SUH 660, TRANSACTIONS OF THE JAPAN SOCIETY OF MECHANICAL ENGINEERS Series A 78 (2012) 1173-1188.

[20] A.-M. Brass, J. Chêne, Hydrogen uptake in 316L stainless steel: Consequences on the tensile properties, Corrosion science 48(10) (2006) 3222-3242.

[21] V.K. Verma, M. Koyama, S. Hamada, E. Akiyama, Multiple damage mechanisms facilitated by planar dislocation glide in a commercial-grade precipitation-strengthened Fe–Ni–Cr-based steel, Materials Science and Engineering: A 782 (2020) 139250.

[22] I. Robertson, The effect of hydrogen on dislocation dynamics, Engineering fracture mechanics 68(6) (2001) 671-692.

[23] Y. Mine, K. Hirashita, M. Matsuda, M. Otsu, K. Takashima, Effect of hydrogen on tensile behaviour of micrometre-sized specimen fabricated from a metastable austenitic stainless steel, Corrosion science 53(2) (2011) 529-533.

[24] O. Takakuwa, Y. Ogawa, J. Yamabe, H. Matsunaga, Hydrogen-induced ductility loss of precipitation-strengthened Fe-Ni-Cr-based superalloy, Materials Science and Engineering: A 739 (2019) 335-342.

[25] S. Chen, M. Zhao, L. Rong, Hydrogen-induced cracking behavior of twin boundary in γ′ phase strengthened Fe−Ni based austenitic alloys, Materials Science and Engineering: A 561 (2013) 7-12.

[26] S. Chen, M. Zhao, L. Rong, Effect of grain size on the hydrogen embrittlement sensitivity of a precipitation strengthened Fe–Ni based alloy, Materials Science and Engineering: A 594 (2014) 98-102.

[27] J.P. Hirth, Effects of hydrogen on the properties of iron and steel, Metallurgical Transactions A 11(6) (1980) 861-890.

[28] M. Zhao, Z. Guo, H. Liang, L. Rong, Effect of boron on the microstructure, mechanical properties and hydrogen performance in a modified A286, Materials Science and Engineering: A 527(21-22) (2010) 5844-5851.

[29] P. Hicks, C. Altstetter, Internal hydrogen effects on tensile properties of iron-and nickel-base superalloys, Metallurgical Transactions A 21(1) (1990) 365-372.

[30] Z. Guo, M. Zhao, C. Li, S. Chen, L. Rong, Mechanism of hydrogen embrittlement in a gamma-prime phase strengthened Fe–Ni based austenitic alloy, Materials Science and Engineering: A 555 (2012) 77-84.

[31] S. Chen, M. Zhao, L. Rong, Role of γ 'characteristic on the hydrogen embrittlement susceptibility of Fe−Ni−Cr alloys, Corrosion Science 101 (2015) 75-83.

[32] R. Nishimura, O.M. Alyousif, A new aspect on intergranular hydrogen embrittlement mechanism of solution annealed types 304, 316 and 310 austenitic stainless steels, Corrosion science 51(9) (2009) 1894-1900.

[33] A.W. Thompson, Ductile fracture topography: geometrical contributions and effects of hydrogen, Metallurgical Transactions A 10(6) (1979) 727-731.

[34] B. Pound, The ingress of hydrogen into precipitation-hardened alloys A-286 and C17200, Corrosion Science 42(7) (2000) 1269-1281.

[35] N. Moody, M. Baskes, S. Robinson, M. Perra, Temperature effects on hydrogen-induced crack growth susceptibility of iron-based superalloys, Engineering Fracture Mechanics 68(6) (2001) 731-750.

[36] P. Platt, J. Sayers, D. Horner, A. Barrow, D. Engelberg, Hydrogen-induced brittle fracture in nickel based alloy 82 weld metal, Corrosion Science 153 (2019) 118-126.

[37] Y. Ogawa, O. Takakuwa, S. Okazaki, K. Okita, Y. Funakoshi, H. Matsunaga, S. Matsuoka, Pronounced transition of crack initiation and propagation modes in the hydrogen-related failure of a Ni-based superalloy 718 under internal and external hydrogen conditions, Corrosion Science 161 (2019) 108186.

[38] Y. Mine, T. Kimoto, Hydrogen uptake in austenitic stainless steels by exposure to gaseous hydrogen and its effect on tensile deformation, Corrosion science 53(8) (2011) 2619-2629.

[39] M. Koyama, E. Akiyama, T. Sawaguchi, K. Ogawa, I.V. Kireeva, Y.I. Chumlyakov, K. Tsuzaki, Hydrogen-assisted quasi-cleavage fracture in a single crystalline type 316 austenitic stainless steel, Corrosion science 75 (2013) 345-353.

[40] M. Koyama, E. Akiyama, Y.-K. Lee, D. Raabe, K. Tsuzaki, Overview of hydrogen embrittlement in high-Mn steels, international journal of hydrogen energy 42(17) (2017) 12706-12723.

[41] Z. Tarzimoghadam, D. Ponge, J. Klöwer, D. Raabe, Hydrogen-assisted failure in Ni-based superalloy 718 studied under in situ hydrogen charging: the role of localized deformation in crack propagation, Acta Materialia 128 (2017) 365-374.

[42] S.K. Dwivedi, M. Vishwakarma, Hydrogen embrittlement in different materials: A review, International Journal of Hydrogen Energy 43(46) (2018) 21603-21616.

[43] M. Koyama, K. Habib, T. Masumura, T. Tsuchiyama, H. Noguchi, Gaseous hydrogen embrittlement of a Ni-free austenitic stainless steel containing 1 mass% nitrogen: Effects of nitrogen-enhanced dislocation planarity, International Journal of Hydrogen Energy (2020).

[44] K. Nibur, D. Bahr, B. Somerday, Hydrogen effects on dislocation activity in austenitic stainless steel, Acta materialia 54(10) (2006) 2677-2684.

[45] Y. Mine, A. Orita, K. Murakami, J.-M. Olive, Fatigue crack growth behaviour in austenitic stainless steels subjected to superficial and entire hydrogenation, Materials Science and Engineering: A 548 (2012) 118-125.

[46] A. Turnbull, Modelling of environment assisted cracking, Corrosion Science 34(6) (1993) 921-960.

[47] S. Cao, S. Zhu, C.V. Samuel Lim, X. Zhou, X. Chen, B.R.W. Hinton, R.R. Boyer, J.C. Williams, X. Wu, The mechanism of aqueous stress-corrosion cracking of α + β titanium alloys, Corrosion Science 125 (2017) 29-39.

[48] S. Zhang, J. Wan, Q. Zhao, J. Liu, F. Huang, Y. Huang, X. Li, Dual role of nanosized NbC precipitates in hydrogen embrittlement susceptibility of lath martensitic steel, Corrosion Science 164 (2020) 108345.

[49] H.K. Birnbaum, P. Sofronis, Hydrogen-enhanced localized plasticity—a mechanism for hydrogen-related fracture, Materials Science and Engineering: A 176(1-2) (1994) 191-202.

[50] D.P. Abraham, C.J. Altstetter, Hydrogen-enhanced localization of plasticity in an austenitic stainless steel, Metallurgical and Materials transactions A 26(11) (1995) 2859-2871.

[51] Y. Liang, P. Sofronis, N. Aravas, On the effect of hydrogen on plastic instabilities in metals, Acta Materialia 51(9) (2003) 2717-2730.

[52] C. Beachem, A new model for hydrogen-assisted cracking (hydrogen "embrittlement"), Metallurgical and Materials Transactions B 3(2) (1972) 441-455.

[53] S. Lynch, L. SP, Mechanisms of hydrogen-assisted cracking, (1979).

[54] T. Tabata, H. Birnbaum, Direct observations of hydrogen enhanced crack propagation in iron, Scripta Metallurgica 18(3) (1984) 231-236.

[55] M. Martin, B. Somerday, R. Ritchie, P. Sofronis, I. Robertson, Hydrogen-induced intergranular failure in nickel revisited, Acta Materialia 60(6-7) (2012) 2739-2745.

[56] W. Geng, A.J. Freeman, R. Wu, C. Geller, J. Raynolds, Embrittling and strengthening effects of hydrogen, boron, and phosphorus on a Σ 5 nickel grain boundary, Physical Review B 60(10) (1999) 7149.

[57] D. Jiang, E.A. Carter, First principles assessment of ideal fracture energies of materials with mobile impurities: implications for hydrogen embrittlement of metals, Acta materialia 52(16) (2004) 4801-4807.

[58] M. Koyama, E. Akiyama, K. Tsuzaki, Effect of hydrogen content on the embrittlement in a Fe–Mn–C twinning-induced plasticity steel, Corrosion science 59 (2012) 277-281.

[59] D. Ulmer, C. Altstetter, Hydrogen-induced strain localization and failure of austenitic stainless steels at high hydrogen concentrations, Acta Metallurgica et Materialia 39(6) (1991) 1237-1248.

[60] C. McMahon Jr, Hydrogen-induced intergranular fracture of steels, Engineering Fracture Mechanics 68(6) (2001) 773-788.

List of tables and figures

Table 4.1. Chemical composition of the steel used (wt. %) [21].

C	Si	Mn	P	S	Ni	Cr	Mo	V	Al	B	Ti
0.05	0.12	0.11	0.006	0.001	24.16	13.76	1.11	0.34	0.17	0.0041	2.04

Table 4.2. Chemical composition of the carbide shown in Fig. 4.1(b) in wt.% (values in parentheses indicate at.%).

C	Fe	Cr	Ni	Mo	Ti
6.0 (21.0)	0.7 (0.5)	0.4 (0.3)	0.1 (0.1)	7.8 (3.4)	85.0(74.7)

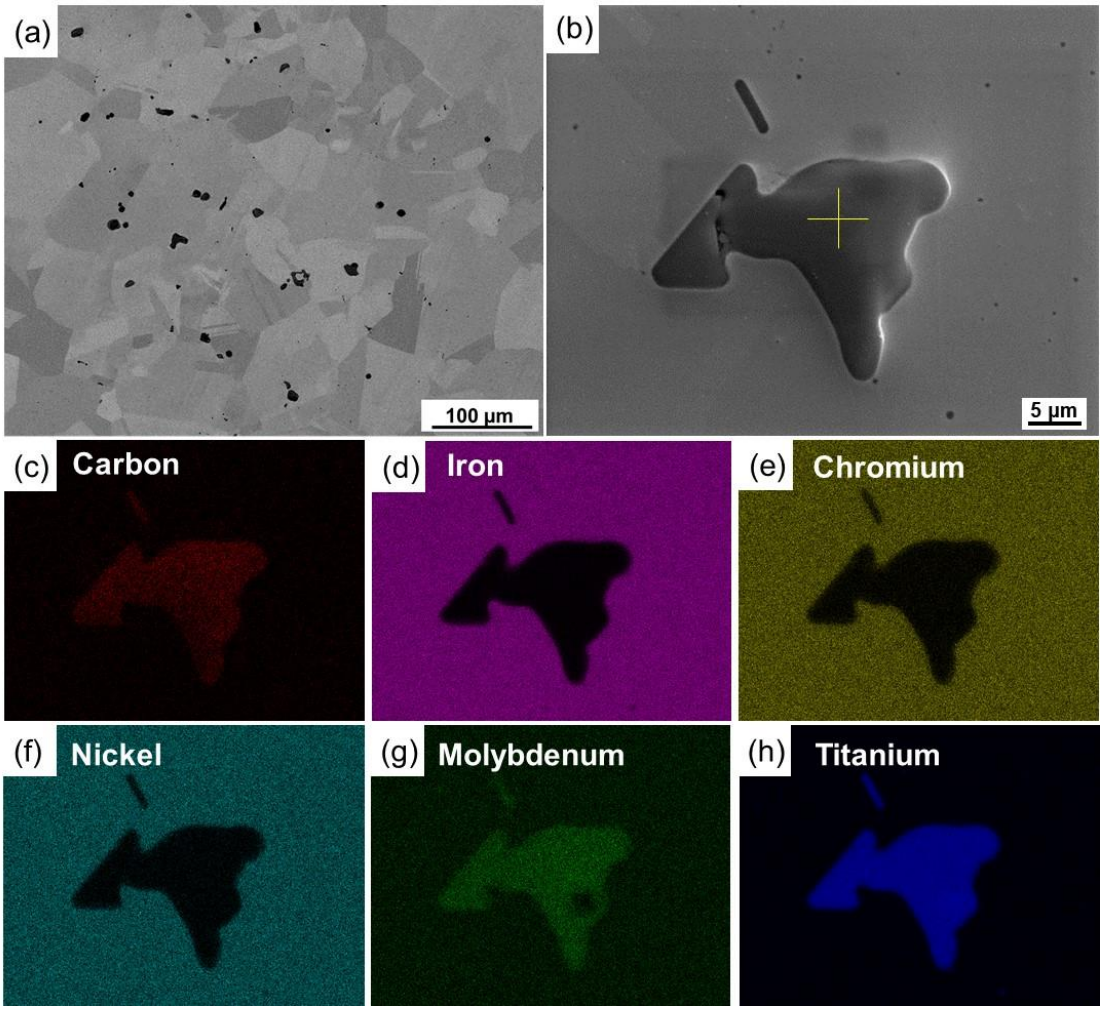

Fig. 4.1. SEM micrographs and EDS elemental maps in the as-received condition. (a) Overview and (b) magnification of an inclusion. The crossing point of the yellow lines in (b) indicates the site used for a point analysis of the EDS. EDS maps of (c) carbon, (d) iron, (e) chromium, (f) nickel, (g) molybdenum, and (h) titanium. The map of Mo was obtained from L-line, and the other EDS maps were measured from K-line.

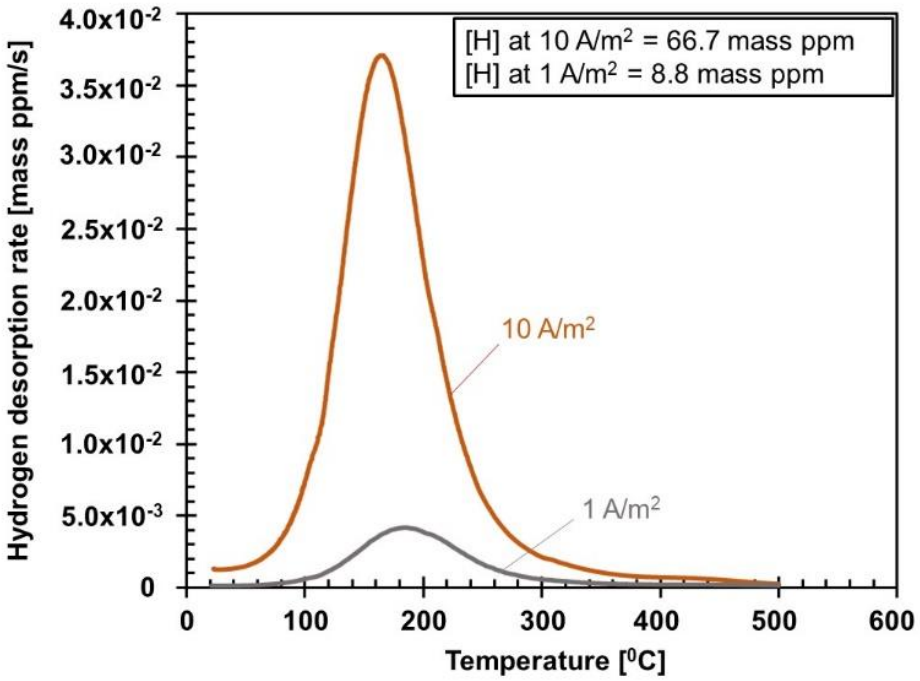

Fig. 4.2. TDS profiles of hydrogen-charged specimens.

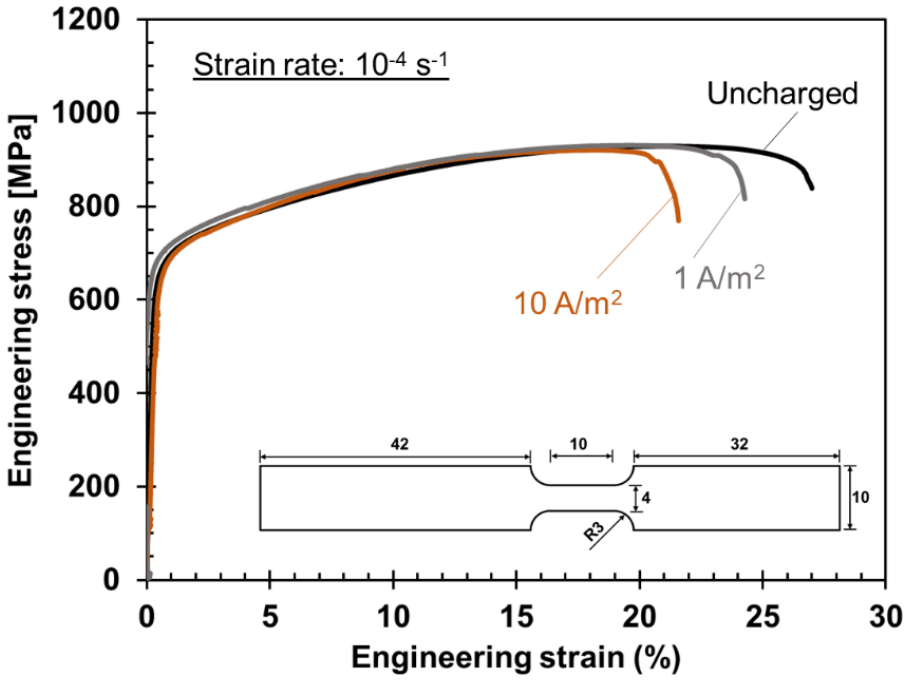

Fig. 4.3. Engineering stress-strain curves with different hydrogen charging conditions. The inset indicates tensile specimen used for these tests (in mm).

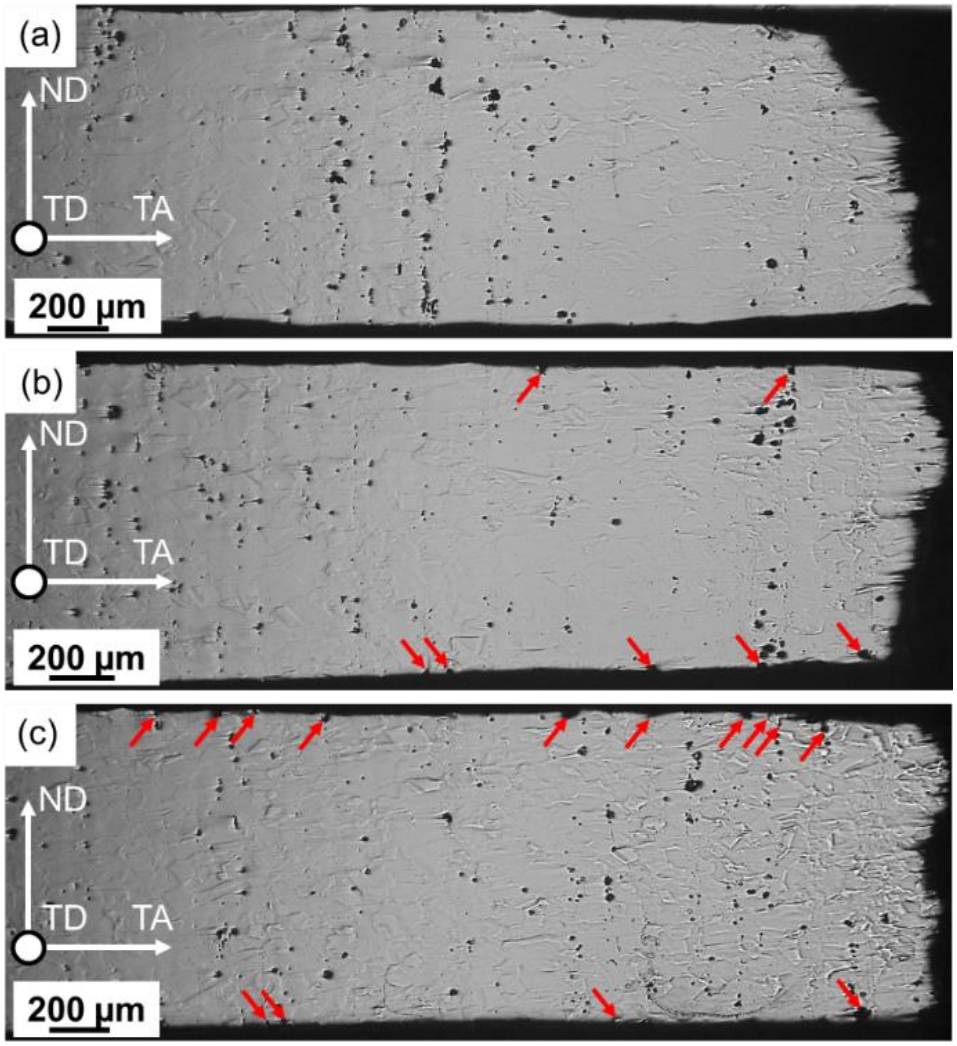

Fig. 4.4. Transverse cross-sectional images of the fractured specimens (a) without hydrogen-pre-charging and (b, c) with hydrogen pre-charging at 1 and 10 A/m^2, respectively. The red arrows indicate surface damages. ND, TD, and TA indicate normal direction, transverse direction, and tensile axis, respectively.

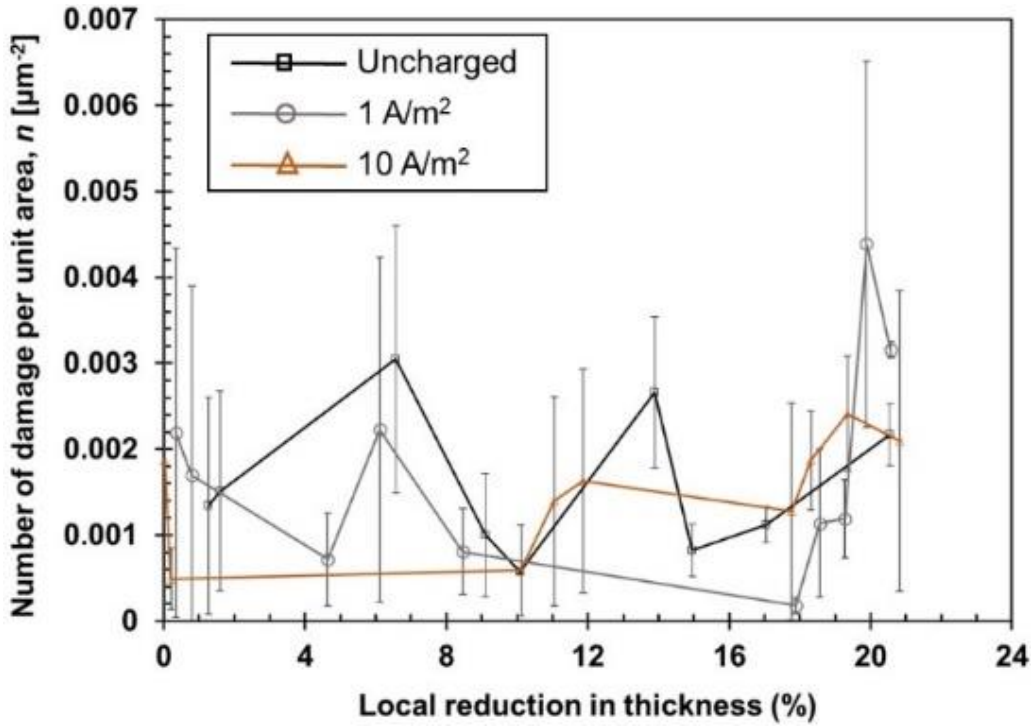

Fig. 4.5. Number of damage per unit area plotted against local reduction in thickness. The damage quantification was done along two-axis near the upper and lower edge of the cross- section.

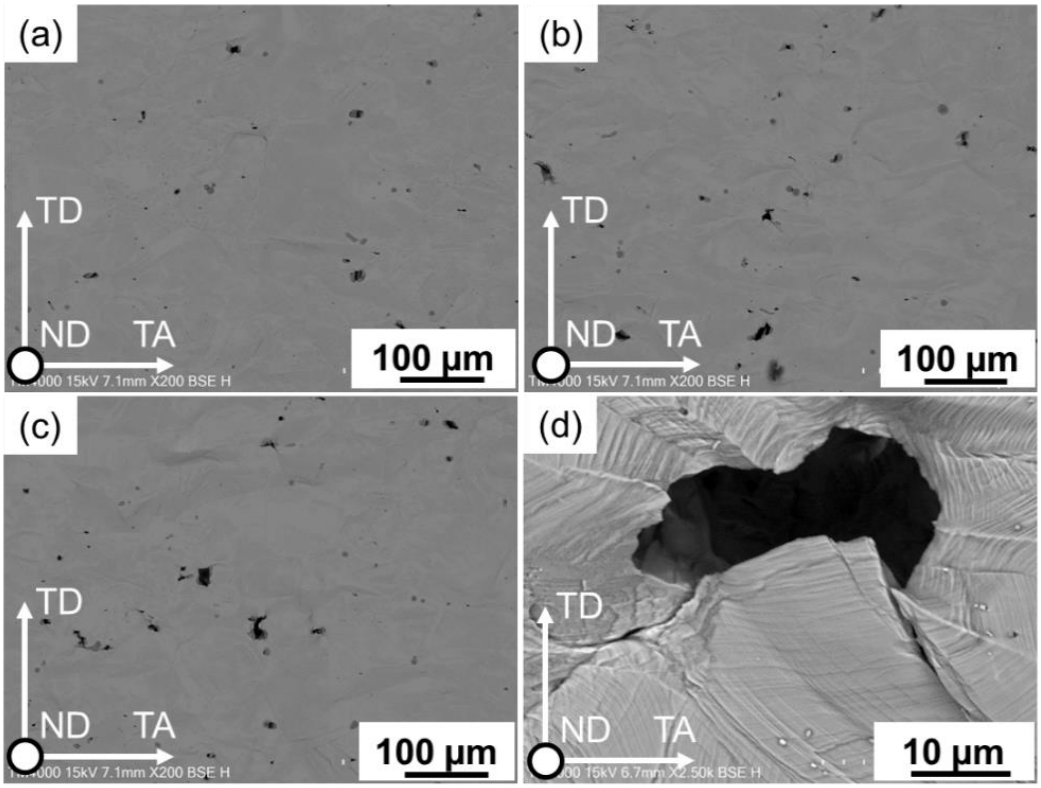

Fig. 4.6. Surface images of the fractured specimen without hydrogen charging taken at (a) 4.14, (b) 3.07, (c) 2.42, and (d) 1.05 mm from the fracture surface. The high-magnification image in (d) shows damage tip blunting involving a large plastic deformation.

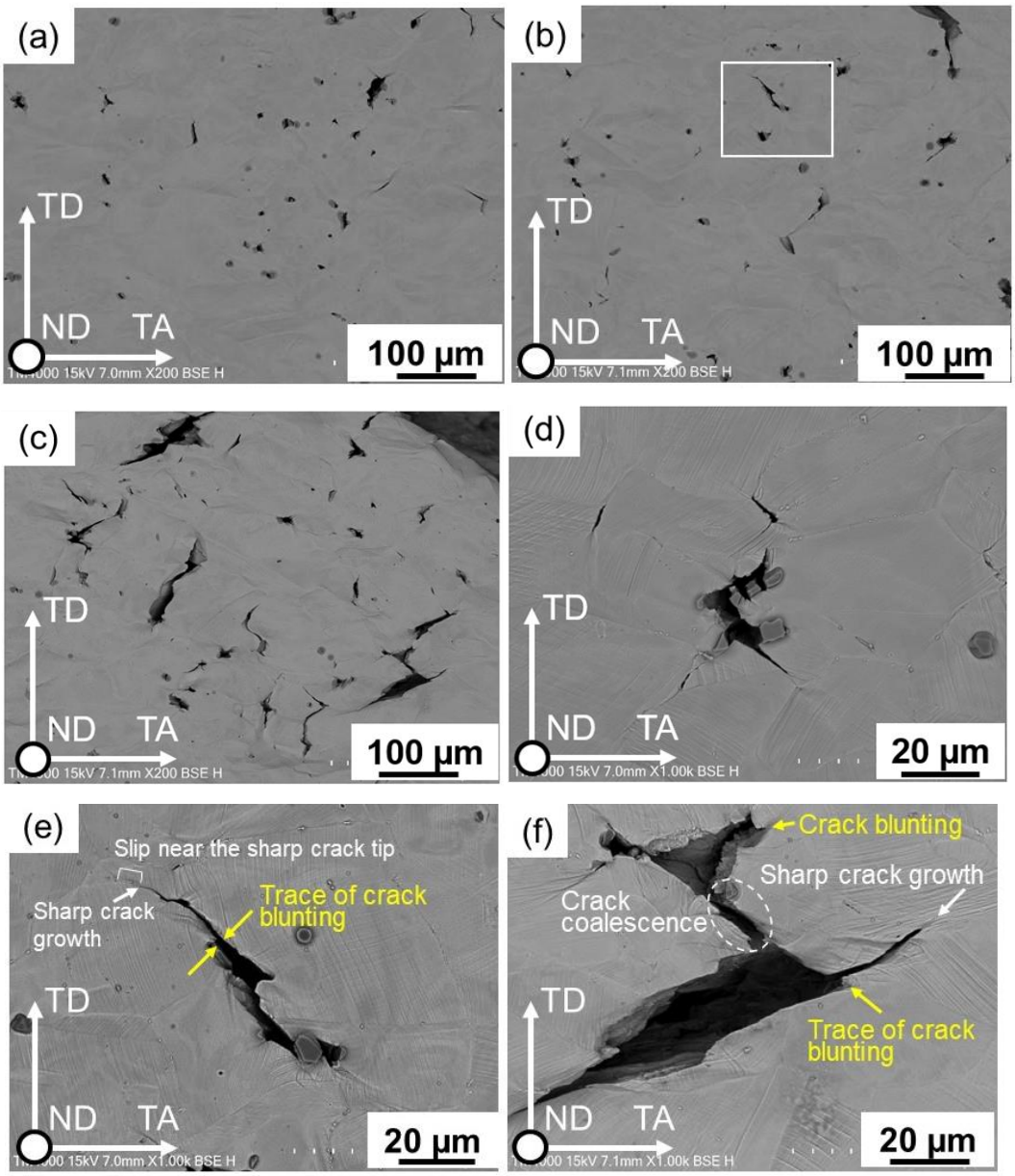

Fig. 4.7. Surface damage at low- (a, b, c) and high- (d, e, f) magnifications for the specimen hydrogen-charged at 1 A/m^2. These images were taken at (a) 3.06, (b, e) 2.06, and (c, f) 1.26, (d) 4.06 mm from the fracture surface.

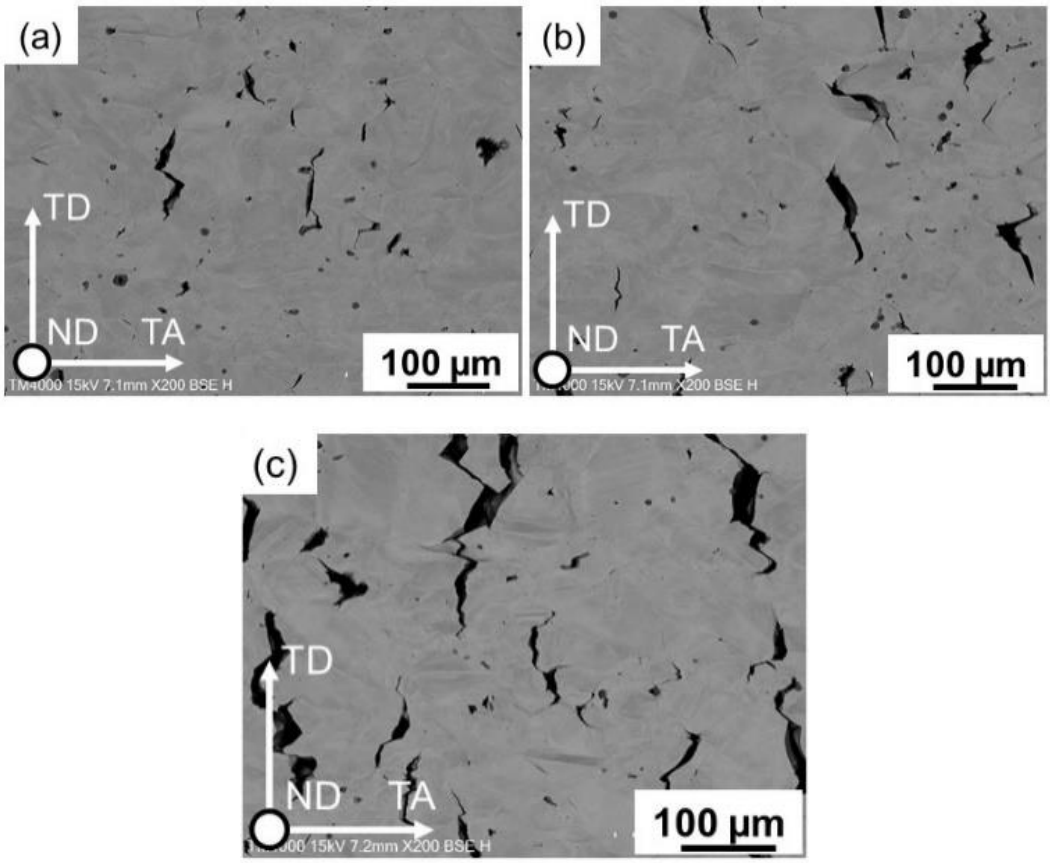

Fig. 4.8. Surface damage at low-magnification for the specimen hydrogen-charged at 10 A/m^2, which were taken at (a) 4.47, (b) 3.47, and (c) 2.47 mm from the fracture surface.

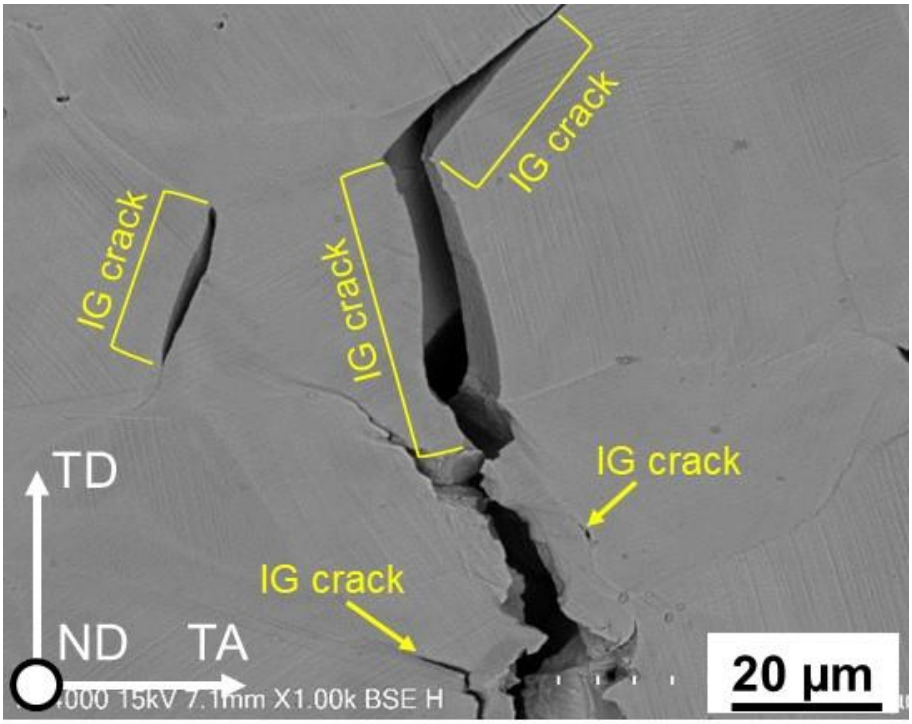

Fig. 4.9. Surface damage at high-magnification for the specimen hydrogen-charged at 10 A/m^2. This image was taken at a distance of 7.47 mm from the fracture surface. IG: Inter-granular.

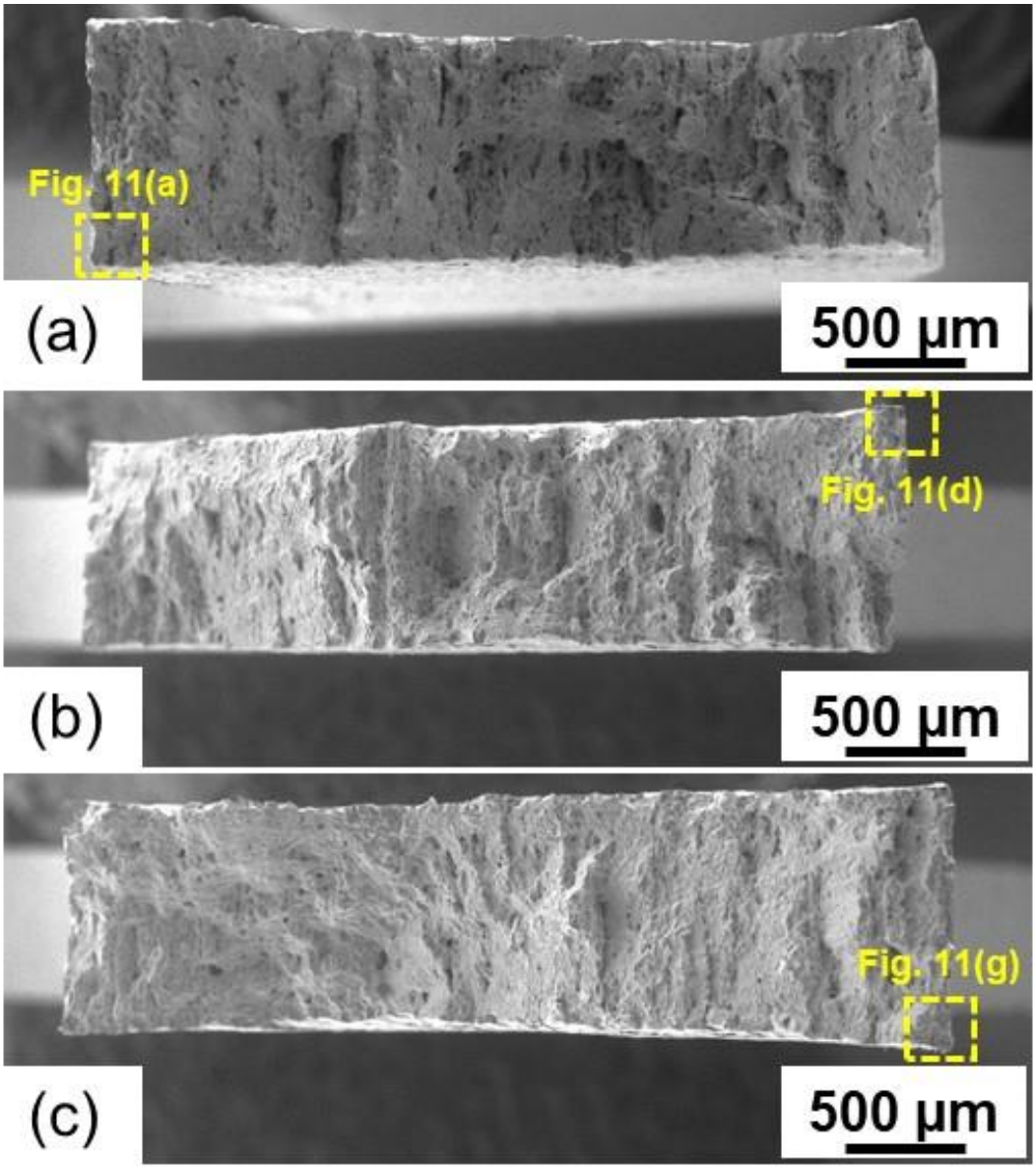

Fig. 4.10. Overall view of the fracture surfaces for specimens (a) uncharged and hydrogen-charged at (b) 1 and (c) 10 A/m^2.

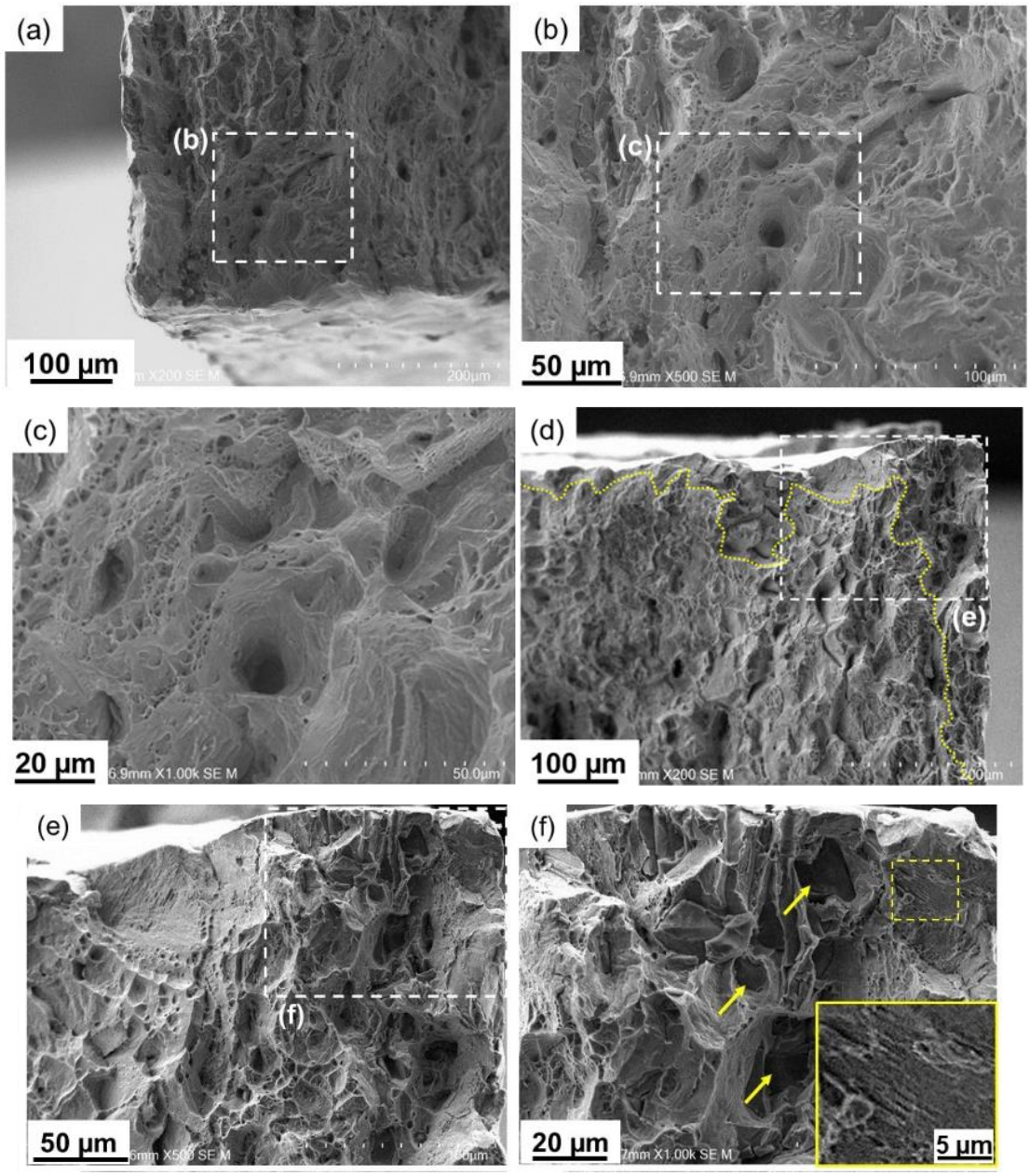

Fig. 4.11. Fractographs with different magnifications for the specimens (a, b, c) uncharged, (d, e, f) hydrogen-charged at 1 A/m^2, and (g, h, i) hydrogen-charged at 10 A/m^2. The yellow dotted curves indicate boundaries between ductile and brittle-like zones. The inset in (f) is a magnification of the region highlighted by the dashed yellow square. The yellow arrows in (f) indicate relatively smooth faceted surface regions.

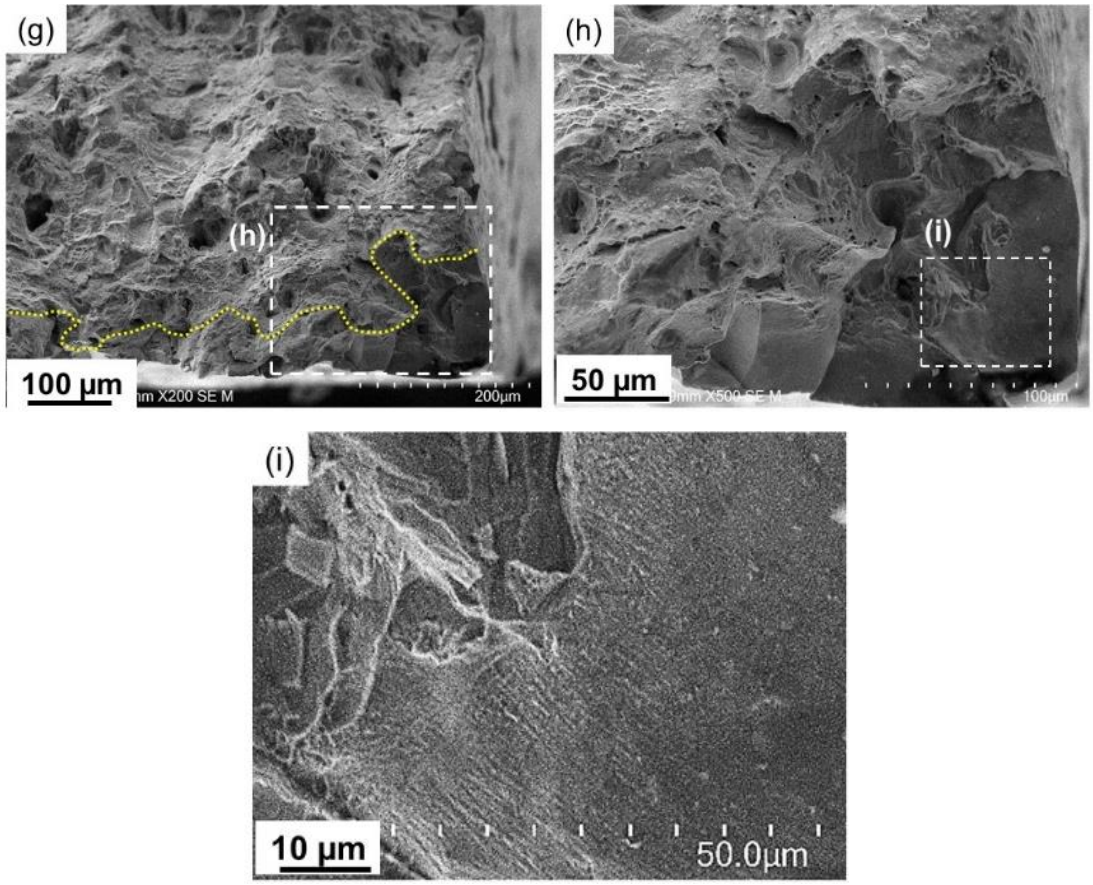

Fig. 4.11. Fractographs with different magnifications for the specimens (a, b, c) uncharged, (d, e, f) hydrogen-charged at 1 A/m^2, and (g, h, i) hydrogen-charged at 10 A/m^2. The yellow dotted curves indicate boundaries between ductile and brittle-like zones. The inset in (f) is a magnification of the region highlighted by the dashed yellow square. The yellow arrows in (f) indicate relatively smooth faceted surface regions. (continued)

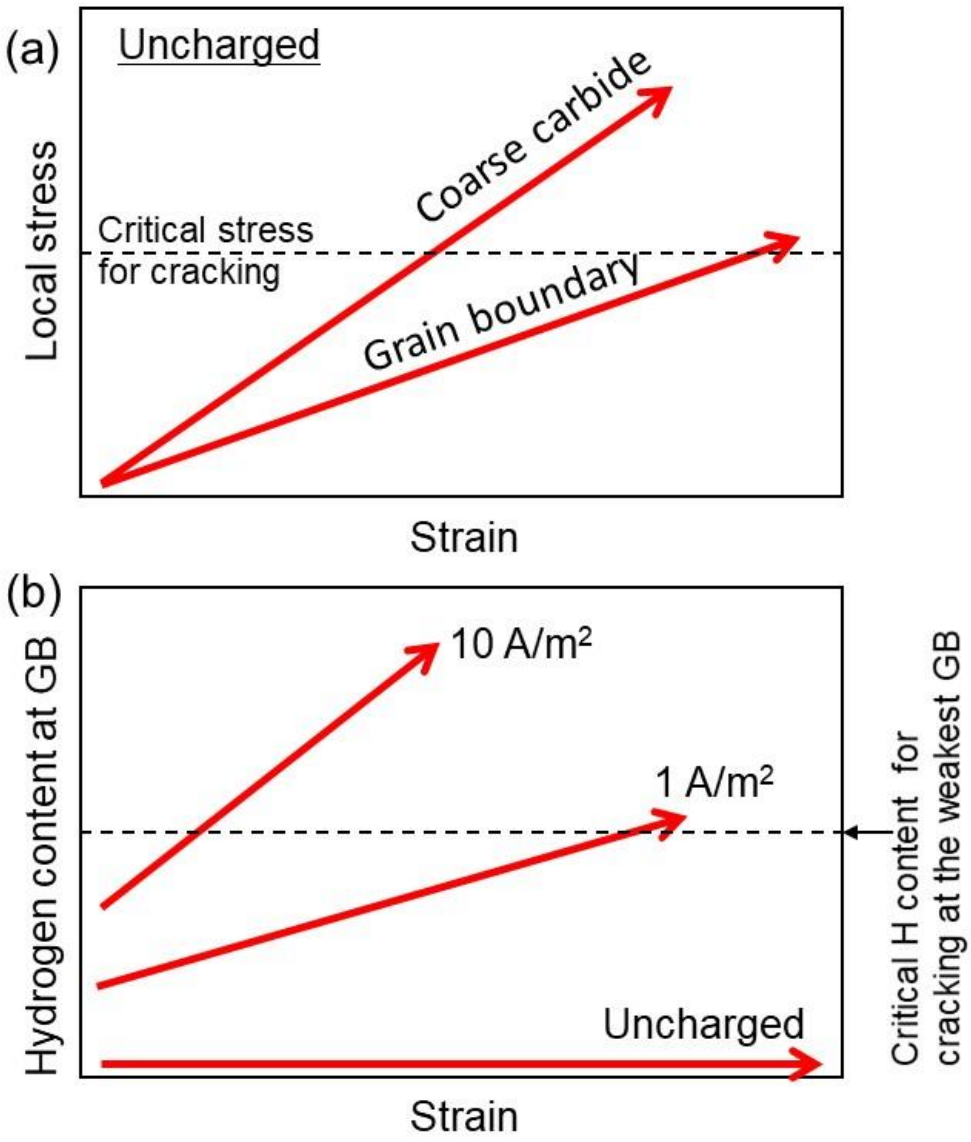

Fig. 4.12. Schematics for the strain-dependent (a) local stress and (b) hydrogen content at grain boundaries (GB). Here, in (a), the critical stress for cracking at carbide was assumed to be the same as that at grain boundary, but there would be a significant difference between them in reality.

Chapter 5 Effect of strain localization on fatigue crack initiation and fatigue limit prediction of commercial grade precipitation-strengthened Fe-Cr-Ni based steel

5.1. Introduction

Previous studies have a major focus on damage evolution and crack behaviour of this material [1, 2]. However, crack initiation and fatigue limit prediction is one of the crucial factors for long term reliability of the material. Chapter 3 focused on the sequential evolution of the damage and its quantification, under tensile loading, in order to predict a better design while considering this material. It was observed that the primary damage initiation site was inclusions and grain boundary acts as a secondary damage initiation site [1], which was also confirmed by fractography. In chapter 4, when the same phenomenon was studied under hydrogen environment, it was found that the damage initiation site shows a transition from inclusion to slip bands and then to grain boundary [3-5]. It was evident from these studies that damage evolution initiated in the early deformation stage because of the dislocation slip planarity. Moreover, the characteristics associated with damage evolving even in a uniform deformation stage play a disadvantageous role in fatigue [6, 7] for the following three reasons: (1) fatigue damage evolution is a plasticity-induced phenomenon, (2) it occurs without necking of specimens, and (3) it is sensitive to planar slip. Therefore, in this study, the author will examine the crack initiation phenomenon in the case of fatigue loading. Since inclusions and grain boundary were found to be the primary sites of damage initiation, it will be important to report the actual crack initiation site in the case of fatigue loading. Based on the analysis of crack initiation site an effort will be made to predict the fatigue limit in the case of plain specimens without any artificial defect.

5.2 Experimental procedure

5.2.1. Material and specimen

The material used for this chapter is SUH 660, i.e. a commercial grade γ′-precipitation-strengthened austenitic steel. The detail of material along with microstructure is already mentioned in chapter 3, section 3.2.1.

5.2.2. Hardness measurement

It was reported by the previous researcher that SUH 660 shows a considerable scatter in the hardness data [8]. In order to have clarity on the hardness distribution of this material hardness test is carried out. The material preparation is the same as discussed previously in chapter 3, section 3.2.2. The hardness test was carried out on HMV – G series, Shimadzu, Japan.

5.2.3. Fatigue test

Dog-bone shaped specimens were fabricated and mirror polished. The specimen design and the artificial defect geometry is shown in Fig. 5.1. The tension-compression fatigue test was carried out on dog-bone plate specimens with an artificial defect [9]. The test was done on ono-type rotating-bending fatigue machine. Further fatigue test was carried out on plain specimens in order to determine the fatigue limit of the material.

5.2.4. Microscopic analysis

The fatigue tested specimen was observed under a scanning electron microscope (Hitachi, SU3500). Two types of observation were carried out, at first the specimen surface was analysed, and secondly, fractography of the fracture surface was done.

5.3 Results

5.3.1. Hardness measurement

Vickers hardness was measured at two different indentation loads of 4.9 N and 19.61 N. The two loads were chosen in order to have an indentation, within the grain and other having more than one grain. The average diagonal length of the resulting indentations is 58 μm and 109 μm for indentation loads of 4.9 N and 19.61 N, respectively. By following

this method micro (within grain) and macro (bulk) hardness were measured. The plot of Fig. 5.2 shows the hardness distribution. It was observed that the slope of fit is approximately same in both cases, average hardness is 295 ± 10 kgf/mm^2, approximately. It can be observed that the macro-hardness distribution is fairly confined near the average hardness. This shows that the hardness of the material is fairly constant and is independent of the measurement location.

5.3.2. Fatigue limit

The tension-compression fatigue test was carried out at different stress amplitudes to find out the fatigue limit. Fig. 5.3 shows the *S-N* diagram. The fatigue limit in this chapter is defined as the run-out stress at 10^7 cycles, having non-propagating cracks. It shows that the specimen has a fatigue limit of 193 MPa.

5.3.3. Fatigue test of specimen with artificial defect

Based on the previous study [1, 3], it was assumed that in the case of fatigue loading, the crack would initiate from artificial defect. Based on approximate inclusion size in microstructure, the size of the artificial defect ($\sqrt{area} = 125$ μm) is chosen to be fairly large enough to act as primary damage initiation site. The fatigue test was carried out at stress amplitude of 300 MPa. The results of the fatigue test show that the crack has initiated from a location other than the artificial defect, as shown in Fig. 5.4. In order to analyse the crack propagation behaviour EBSD observation was carried out, Fig. 5.5. We have traced the crack propagation path to see that whether the crack propagation is along the slip plane of the fcc metal, i.e. [111] plane. Since the crack propagation is along the slip plane, we can assure the application of Murakami's equation for estimating the fatigue limit of the material.

5.3.4. Microscopic damage evolution

In order to investigate the origin of the damage, crack initiation is investigated, with the help of scanning electron microscope. Fig. 5.6 shows the overall images of the non-propagating crack at the fatigue limit, stress amplitude of 193 MPa after $N = 10^7$ cycles. Many long and small cracks are visible, the tendency of coalescence in neighbouring cracks is also evident. Fig. 5.7 shows the high magnification images of the non-

propagating cracks. It was observed that the crack initiation takes place at the grain boundary and within the grain. Majority of the crack initiation is at the grain boundary with a maximum crack length of 193 μm. Multiple cracks coalesce to propagate to show a final non-propagating crack. Some cracks are also stopped by inclusions.

5.3.5. Fractography

Fig. 5.8 shows the fractography images of the sample fractured at a stress amplitude of 200 MPa (N_f = 1.75×10^6 cycles). This could be very helpful in relating the surface observation with fracture morphology. The overall image in Fig. 5.8(a) shows several flat areas present near the surfaces and also within the surface near the middle portion. The large flat areas are shown by regions enclosed by yellow areas. The region shown by enclosed white, elliptical region resembles coalescence of the cracks. The assumed crack propagation direction is shown by the white arrows. Fig. 5.8(b) shows the enlarged view of the region enclosed by the white rectangular region which will be helpful in apprehending the crack initiation and subsequent propagation.

5.4. Discussion

It has been reported by many researchers that in FCC metals the crack initiation results from persistent slip bands (PSBs) [10-12]. It was reported that the micro-cracks on the surface of the specimen was as long as crystal grain size and propagated through the grain boundary [13]. However, the PSBs could not propagate through the grain boundary [14]. Thus the cracks that are no longer than grain size are supposed to be generated because of cyclic strain localization in the PSBs. The study conducted by Wu et al. [2] also pointed out that the grain itself acts as a self- generated flaw and will result in crack initiation because of strain localization in the grain. However, the opinion of I and the co-authors [1] is quite different from the previous researchers as we have found that inclusions and grain boundary are the major sites of damage initiation in uniaxial tensile loading.

Having this as background fatigue test was carried out on specimen with an artificial defect. The defect size is large enough to be considered as an inclusion, surprisingly the crack did not initiate from the defect (Fig. 5.4). The crack has initiated from a different location. This indicates that the primary site of damage initiation in fatigue loading is different from that in the case of uniaxial loading.

In order to look for this surface, SEM study was done for fatigue limit sample (Fig. 5.6). It was found that there are two sites of crack initiation, that is grain and grain boundary. A majority of crack initiated from the grain boundary, therefore grain boundary is the primary site of crack initiation. The cracks that are initiated from the grain or grain boundary coalesce after they face each other in their neighbour. The cause of damage initiation at the grain and grain boundary is assumed to be strain localization at the microstructural barriers due to less affinity for stress accommodation because of planar dislocation motion [15]. Fractography results (Fig. 5.8) also supports this observation. As evident from the fractography that many flat areas (yellow enclosed area) are formed in the fractured sample, this is the result of intergranular crack propagation along grain boundary, which acts as primary damage initiation site because of strain localization. The fractographic features also give evidence of crack coalescence on propagation (shown by elliptical enclosed area).

The other consideration is that the corresponding $\sqrt{area}$ calculation by applying Murakami's equation gives a value of 845 μm (HV = 295 kgf/mm^2, σ_w= 193 MPa). This value seems to be far greater if we consider the crack propagation from a single crack initiation site. This proves the necessity of considering multiple cracks as the initial self-generated flaw to calculate the fatigue limit. The length of multiple cracks, shown in Fig. 5.6, and their area is calculated, and the total area is considered as the area of initial defect [16]. On calculating the fatigue life based on the total area from multiple cracks ($\sqrt{area}$ = 339 μm), the fatigue life σ_w was found as 224 MPa, which is quite relevant as fatigue data is always accompanied by scattering. This shows that in the case of fatigue loading, multiple cracks initiated in the grain and grain boundary will have a cumulative effect, and act as the initial defect.

But still there needs to have a clear understanding of primary fatigue crack initiation site in time scale, so as to have a more precise fatigue limit prediction of the material. As reported previously, we need to consider multiple crack initiation thus we need to implement better statistical tools to predict $\sqrt{area}$. A better prediction of $\sqrt{area}$ will lead to considerably reduced error in fatigue limit prediction.

5.5. Conclusions

The fatigue study of SUH 660 shows that the crack did not initiate from the artificial defect ($\sqrt{area} = 125$ µm), instead it initiated from a different location. This shows that the inclusions are not the primary site of crack initiation. The SEM surface study shows that grain boundary acts as the primary site of crack initiation, due to considerable strain localization, and grain acts as the secondary site. Flat areas in the fractography confirm the major damage in the form of intergranular crack growth and coalescence. Multiple crack initiation should be considered as the initial damage for predicting the fatigue limit.

References

[1] V.K. Verma, M. Koyama, S. Hamada, E. Akiyama, Multiple damage mechanisms facilitated by planar dislocation glide in a commercial-grade precipitation-strengthened Fe–Ni–Cr-based steel, Materials Science and Engineering: A 782 (2020) 139250.

[2] H. Wu, S. Hamada, H. Noguchi, Fatigue strength characteristics evaluation of SUH660 considering small fatigue crack propagation behavior and hardness distribution, International Journal of Fatigue 63 (2014) 1-11.

[3] V.K. Verma, M. Koyama, S. Hamada, E. Akiyama, Effects of hydrogen content that alters damage evolution mechanisms in SUH 660 precipitation-strengthened Fe–Cr–Ni steel, Materials Science and Engineering: A 791 (2020) 139750.

[4] H. Wu, Y. Oshida, S. Hamada, H. Noguchi, Fatigue strength properties of precipitation strengthening stainless steel A286 focused attention on small fatigue crack behaviour, Procedia Engineering 10 (2011) 1973-1978.

[5] Y. Murakami, S. Matsuoka, Effect of hydrogen on fatigue crack growth of metals, Engineering Fracture Mechanics 77(11) (2010) 1926-1940.

[6] P. Cotterill, J. King, Hydrogen embrittlement contributions to fatigue crack growth in a structural steel, International journal of fatigue 13(6) (1991) 447-452.

[7] Y. Murakami, T. Kanezaki, Y. Mine, S. Matsuoka, Hydrogen embrittlement mechanism in fatigue of austenitic stainless steels, Metallurgical and materials Transactions A 39(6) (2008) 1327.

[8] H. Wu, S. Hamada, H. Noguchi, Fatigue strength prediction for inhomogeneous face-centered cubic metal based on Vickers hardness, International Journal of Fatigue 48 (2013) 48-54.

[9] K. Habib, M. Koyama, H. Noguchi, Impact of Mn–C couples on fatigue crack growth in austenitic steels: Is the attractive atomic interaction negative or positive?, International Journal of Fatigue 99 (2017) 1-12.

[10] J. Man, T. Vystavěl, A. Weidner, I. Kuběna, M. Petrenec, T. Kruml, J. Polák, Study of cyclic strain localization and fatigue crack initiation using FIB technique, International Journal of Fatigue 39 (2012) 44-53.

[11] J. Miao, T.M. Pollock, J. Wayne Jones, Crystallographic fatigue crack initiation in nickel-based superalloy René 88DT at elevated temperature, Acta Materialia 57(20) (2009) 5964-5974.

[12] K. Differt, U. Esmann, H. Mughrabi, A model of extrusions and intrusions in fatigued metals II. Surface roughening by random irreversible slip, Philosophical Magazine A 54(2) (1986) 237-258.

[13] J. Miao, T.M. Pollock, J. Wayne Jones, Microstructural extremes and the transition from fatigue crack initiation to small crack growth in a polycrystalline nickel-base superalloy, Acta Materialia 60(6) (2012) 2840-2854.

[14] K.V. Rasmussen, O.B. Pedersen, Fatigue of copper polycrystals at low plastic strain amplitudes, Acta Metallurgica 28(11) (1980) 1467-1478.

[15] O. Takakuwa, Y. Ogawa, J. Yamabe, H. Matsunaga, Hydrogen-induced ductility loss of precipitation-strengthened Fe-Ni-Cr-based superalloy, Materials Science and Engineering: A 739 (2019) 335-342.

[16] M. Yukitaka, Metal fatigue: effects of small defects and nonmetallic inclusions, Elsevier science, Oxford, UK, 2002.

List of figures and tables

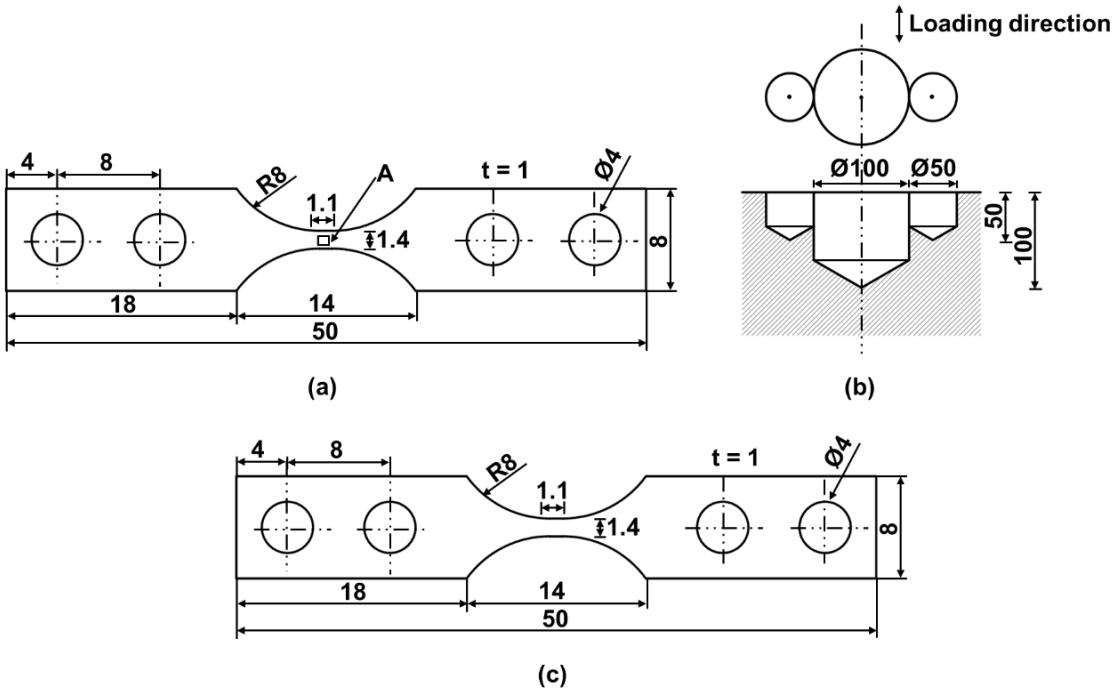

Fig. 5.1. Specimen geometry for tension-compression fatigue test by using rotating-bending fatigue test machine (a) specimen with artificial defect (all dimensions in mm), (b) artificial defect, A, geometry (all dimensions in μm) (b) plane specimen geometry (all dimensions in mm).

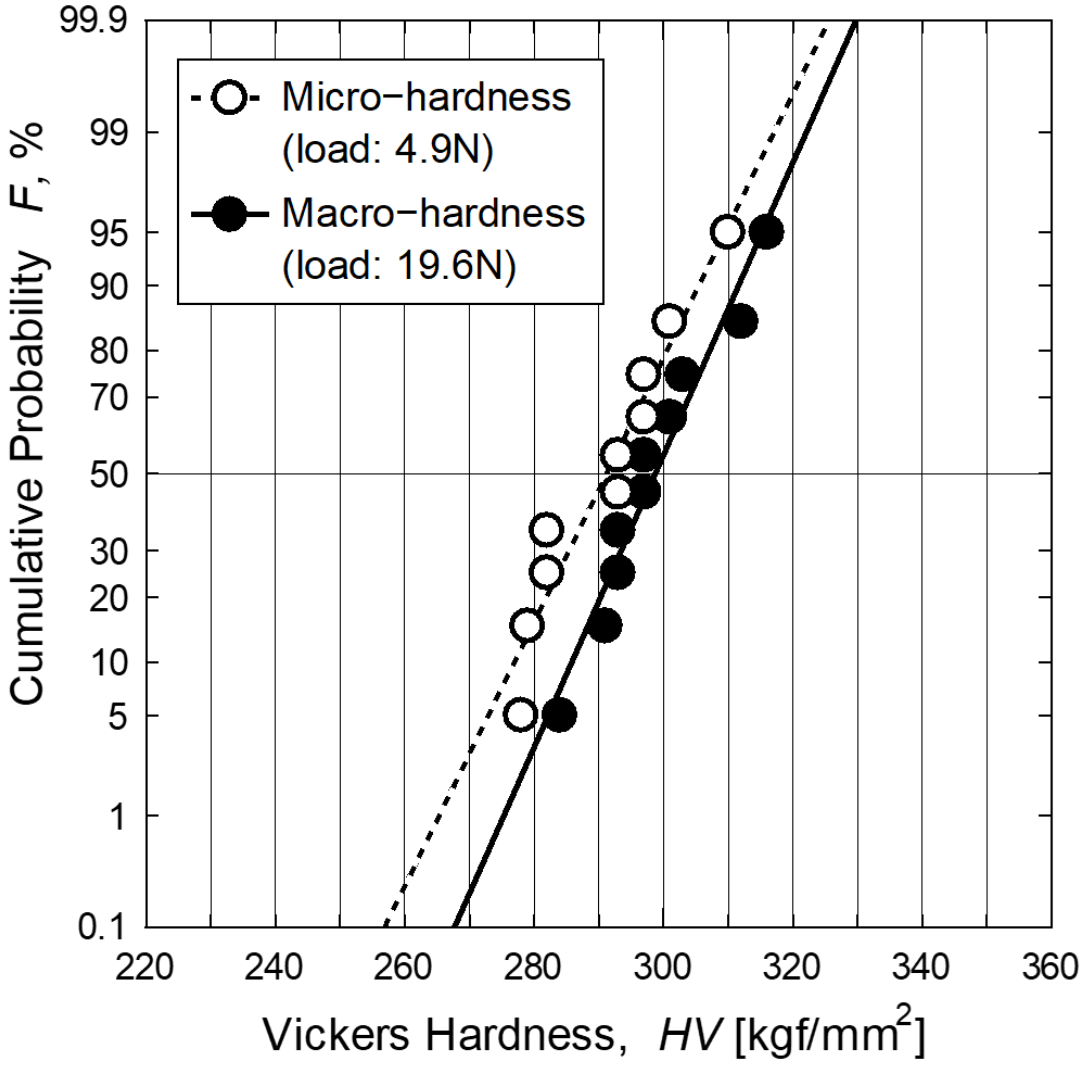

Fig. 5.2 Micro and macro- hardness measurement of SUH 660.

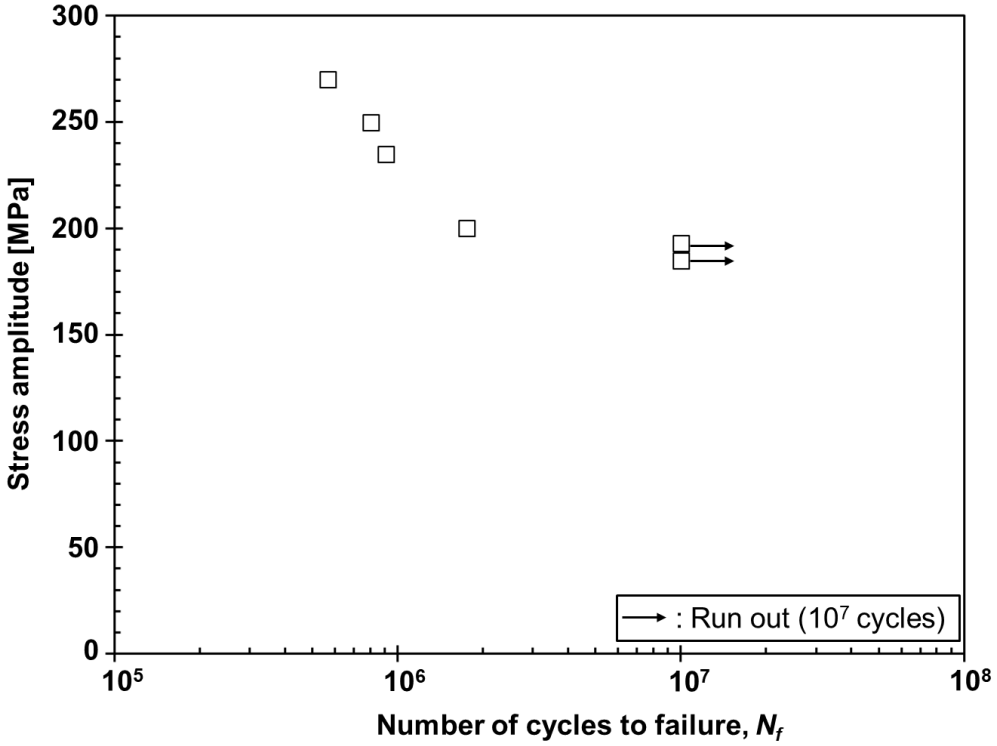

Fig. 5.3 *S*-*N* diagram for SUH 660.

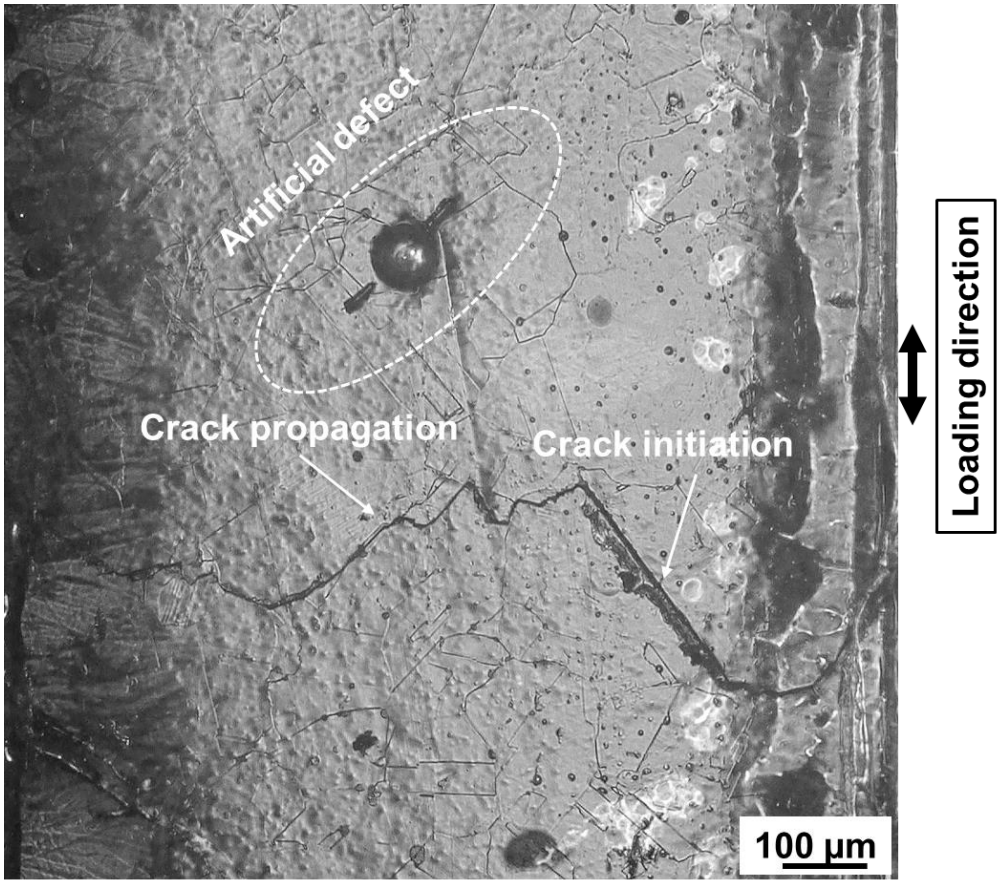

Fig. 5.4 Replica image of tension-compression fatigue test failed specimen ($\sigma_a =$ 300 MPa, $N_f = 4.35 \times 10^5$ cycles) with an artificial defect. The defect is shown by the elliptical region, and the fatigue crack is shown by arrows.

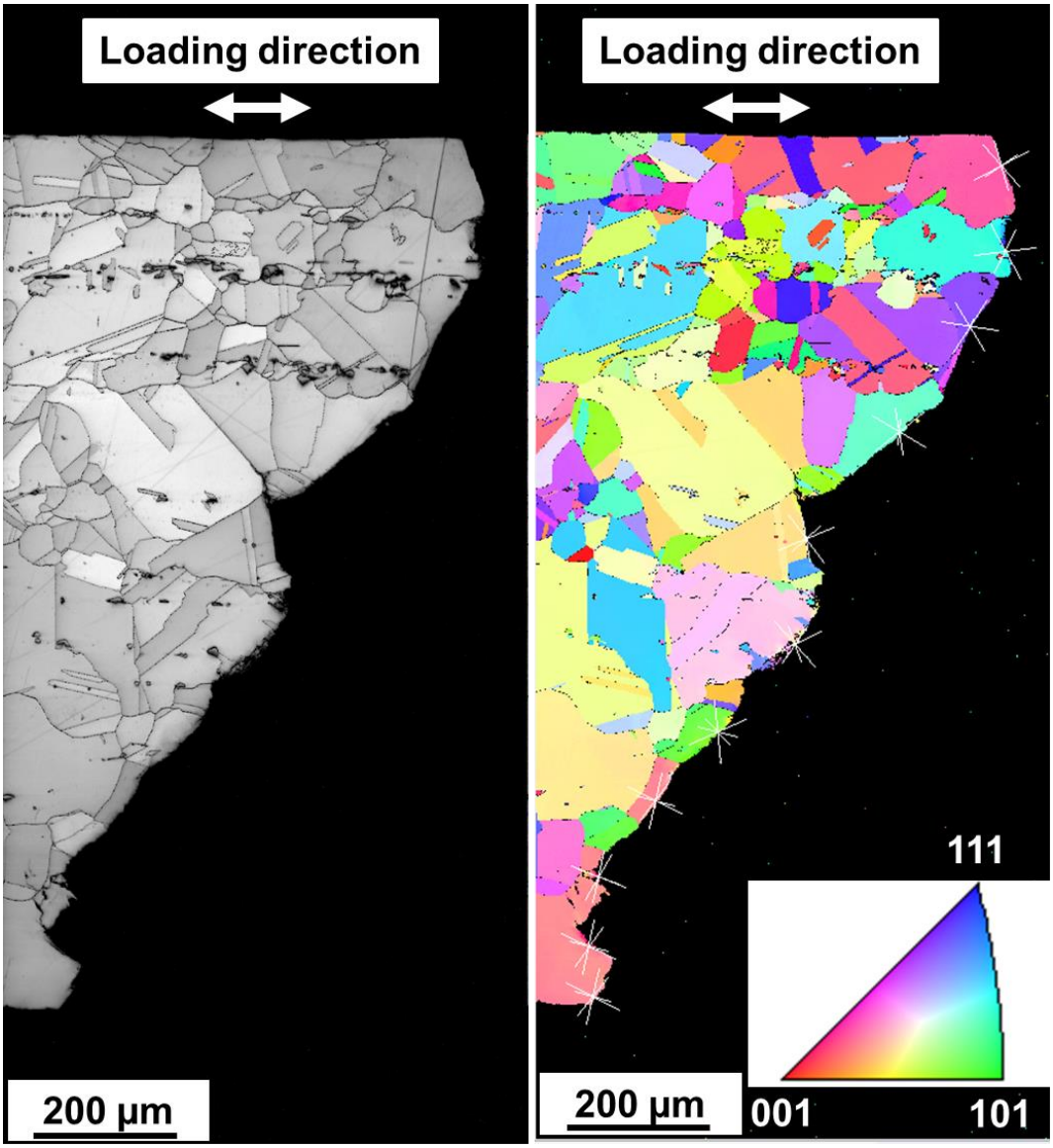

Fig. 5.5. EBSD of the specimen with an artificial defect, the crack initiated and propagation from a different location other than artificial defect ($\sigma_a = 300$ MPa, $N_f = 4.35 \times 10^5$ cycles). (a) IQ map (b) IPF map, plane [111] traces are shown by white lines.

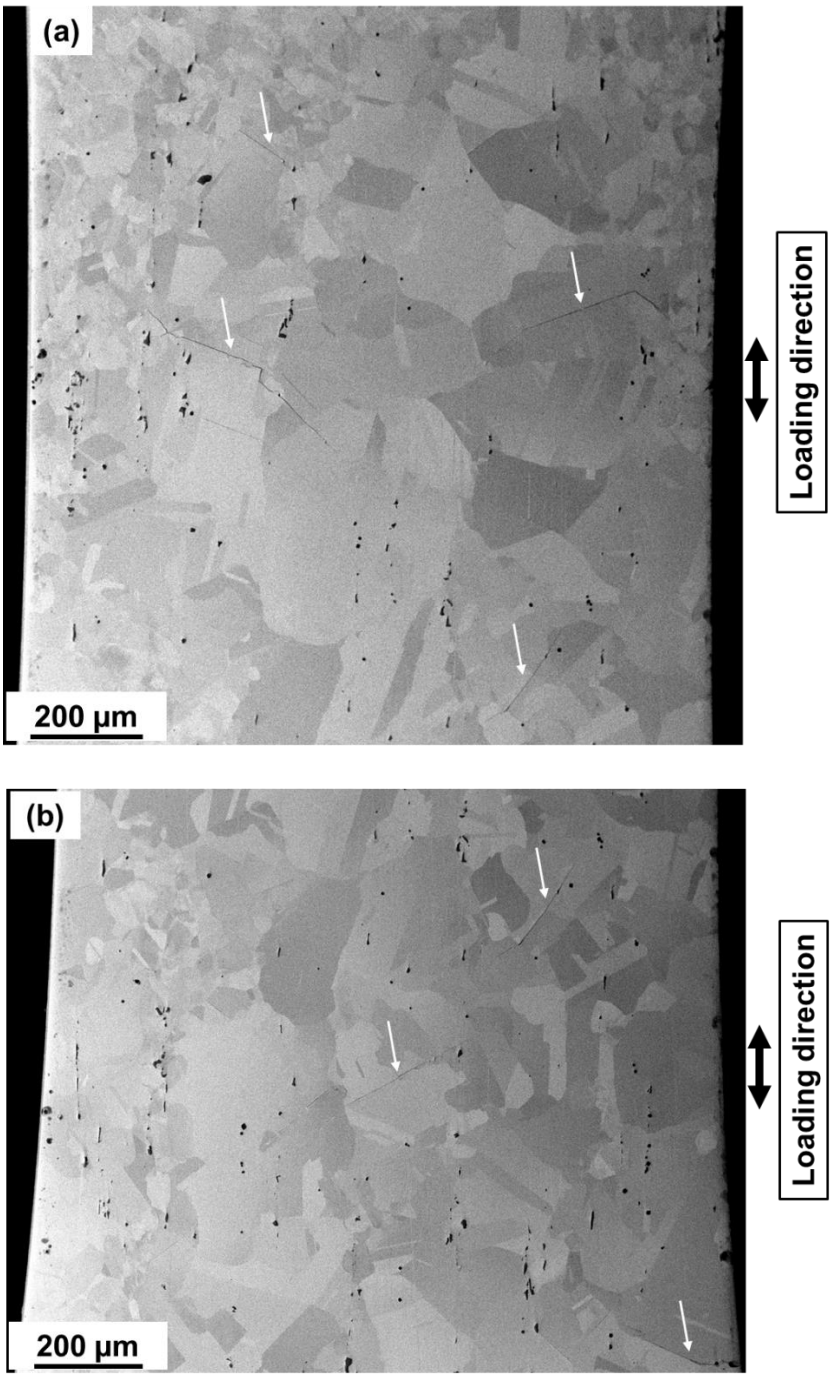

Fig. 5.6. SEM analysis of specimen surface, in back scattered mode, at fatigue limit (σ_a= 193 MPa), run-out for 10^7 cycles. Black entities observed are inclusions, non-propagating cracks are shown by the arrows.

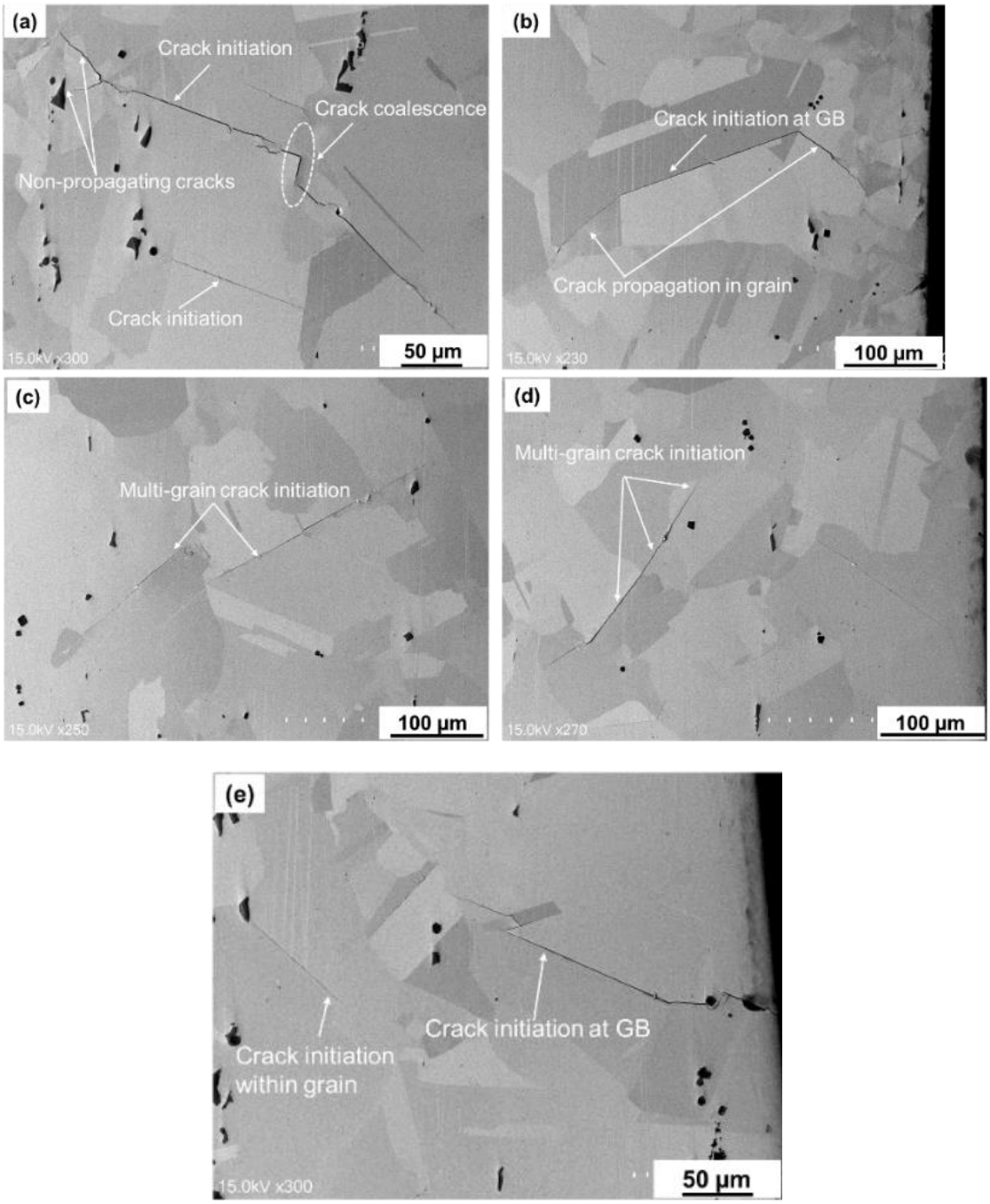

Fig. 5.7. Magnified images of the non-propagating cracks, observed under SEM in back scattered mode. Several intergranular and transgranular crack propagation is observed. Coalescence is shown by the elliptical area.

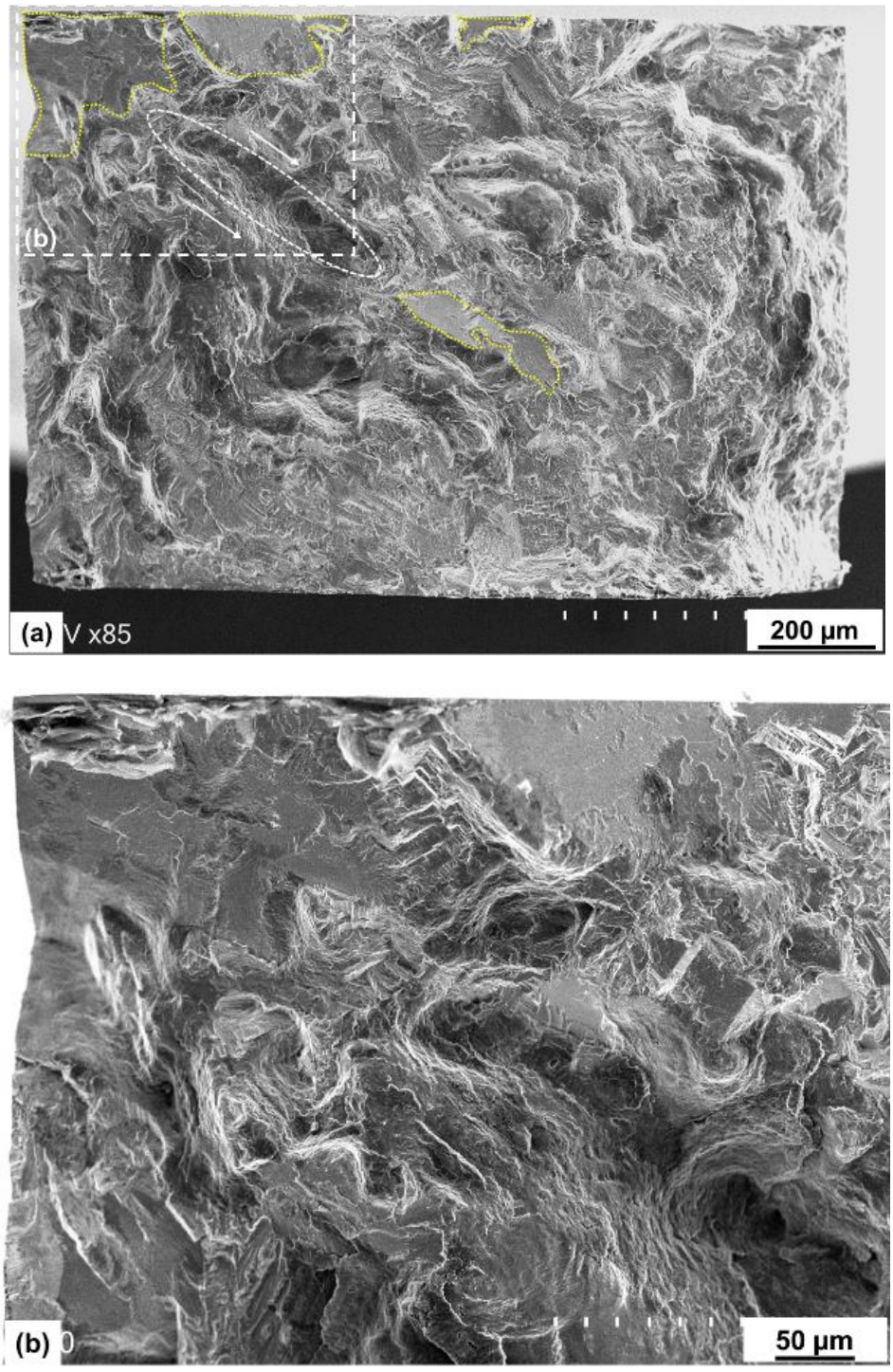

Fig. 5.8. Fractography images in secondary electron mode (a) Flat areas are shown by yellow enclosed area. Coalescence is indicated by elliptical area (b) magnified image of the region in (a) ($\sigma_a = 200$ MPa, $N_f = 1.75 \times 10^6$ cycles).

Appendix

A1. Fractography of the fatigue failed specimen with an artificial defect, at stress amplitude of 300 MPa

As mentioned in the Chapter 5 the crack in the specimen has initiated from a location other than the artificial defect. This gives an indication towards the intensive strain localisation at microstructural entities and the presence of a self-generated initial flaw. Fractography is done, on Hitachi SU3500 operated at 20kV, to analyse the fracture surface morphology. Several flat regions were observed which indicate the dominance of intergranular type of fracture.

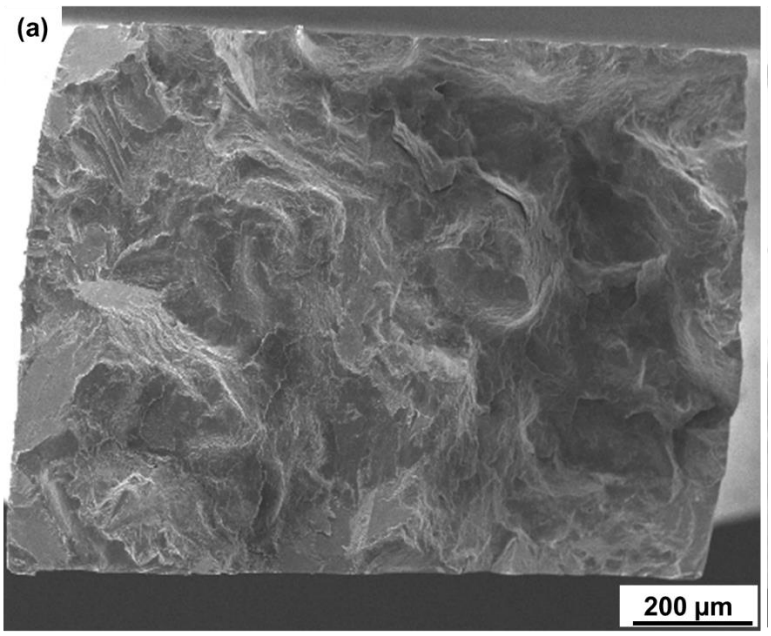

Fig. A1. Fractography of the specimen with an artificial defect, the crack initiated and propagation from a different location other than artificial defect ($\sigma_a = 300$ MPa, $N_f = 4.35 \times 10^5$ cycles). (a) Overall image of the fractured specimen, (b) and (c) magnified images of the flat features showing intergranular fracture.

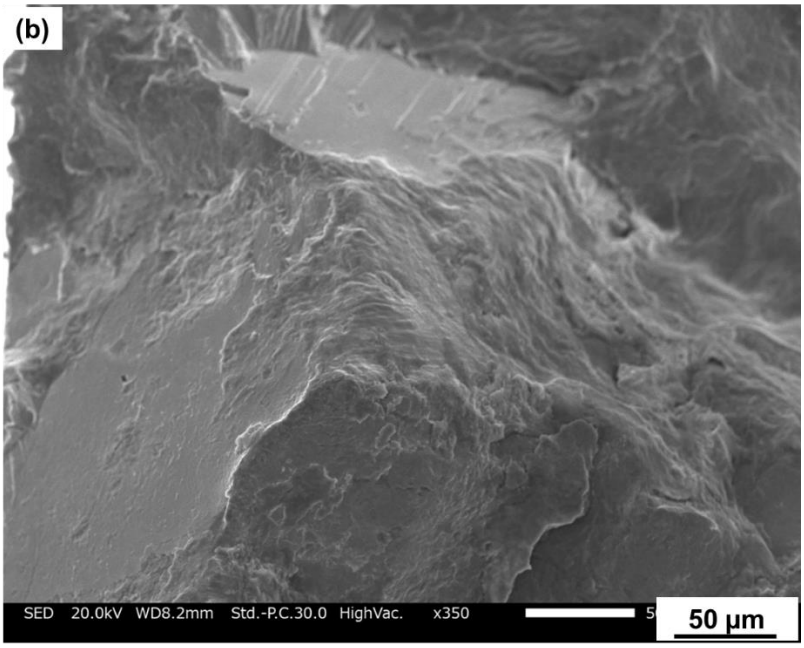

Fig. A1. Fractography of the specimen with an artificial defect, the crack initiated and propagation from a different location other than artificial defect ($\sigma_a = 300$ MPa, $N_f = 4.35 \times 10^5$ cycles). (a) Overall image of the fractured specimen, (b) and (c) magnified images of the flat features showing intergranular fracture. (continued)

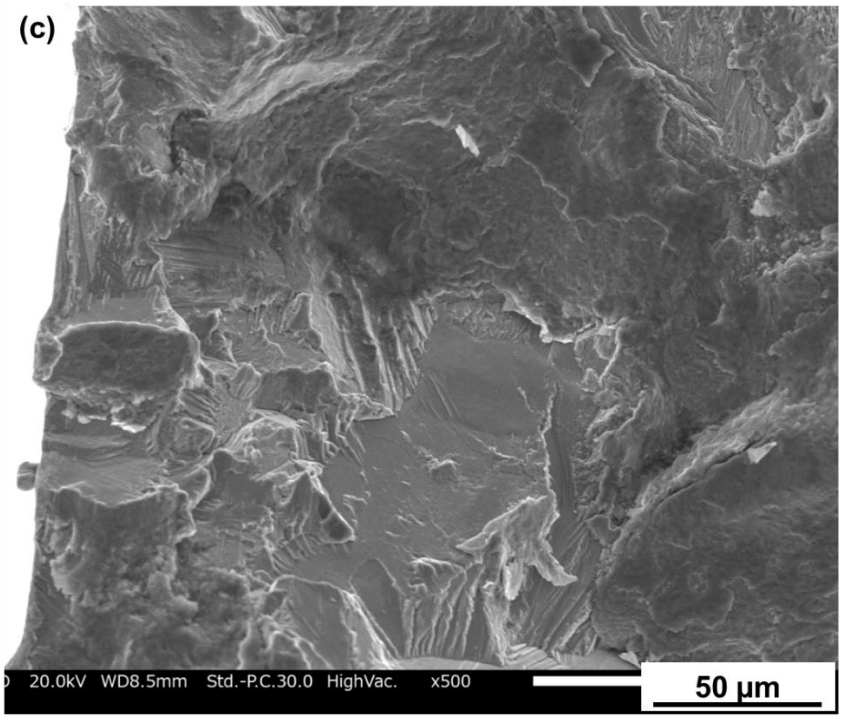

Fig. A1. Fractography of the specimen with an artificial defect, the crack initiated and propagation from a different location other than artificial defect ($\sigma_a = 300$ MPa, $N_f = 4.35 \times 10^5$ cycles). (a) Overall image of the fractured specimen, (b) and (c) magnified images of the flat features showing intergranular fracture. (continued)

Chapter 6 General conclusions

This study is carried out in order to find the possible reasons why precipitation-strengthened steels are weaker than their fatigue strength. The proposed fatigue strength based on empirical equation, $\sigma_w \cong 1.6\,HV$, predicts a higher value of fatigue strength. This signifies the possibility of factors that have negative influence on the fatigue health of precipitation-strengthened steels. As we know that precipitates impart the strength to the material by pinning the dislocation motion. Most of the studies are concerned with the positive impacts of precipitation overlooking the ill effects of precipitation. This study is carried out to conclude the limitations of precipitation-strengthening.

The present study considers three different types of precipitation-strengthened steels, with copper (Cu) precipitate (C6), titanium carbide (TiC) precipitate (T6) and γ′ [Ni_3(Al,Ti)] precipitate (SUH 660). The mechanical behaviour of these steels is considered for different loading conditions and environments, based on strain localization. The way in which the presence of precipitate simulates the mechanical behaviour of the material is concluded in the following paragraphs.

While considering two steels having a difference in the nature of precipitate they bear but having the same tensile strength and micro-hardness, we found that their behaviour for fatigue loading is different. The steel bearing the hard precipitate was supposed to be prone to strain localization while the strain is uniform for the case of steel having soft precipitate. This pre-assumption of strain localization in T6 is confirmed based on the results of tensile test (serrations in T6) and DIC test. Thus from this, we can conclude that the presence of precipitate may result in strain localization which may have an adverse effect on the material fatigue property.

On the other hand, when we look for general precipitation-strengthened steel, we found that the precipitate may also act as an indirect source of strain localization. Instead of strain localization due to dislocation-precipitation interaction, here the strain is localized at the secondary sites due to inability of cross slip. The strain localization at the secondary sites will result in the generation of voids and void-coalescence, in the case of uniaxial loading. This phenomenon is further enhanced by hydrogen environment as hydrogen

will improve the dislocation mobility. However, for the case of fatigue loading, it is surprising to see that the primary crack initiation site is grain boundary and grain itself, because of strain localization.

Thus this study gives a wide range of possibility of how a precipitate will result in tensile and fatigue life depreciation based on strain localization. This can be applied well to the steels bearing similar properties.

Chapter 7 Future plan

In the chapter 2, we have studied about "Effect of strain localization on fatigue properties of precipitation-strengthened steel with an arbitrary length crack", but there is a lack of evidence to our proposed assumptions. Few of them are:

Proposing the theory of strain localization based on which I have explained the results of crack propagation behavior in short crack and long crack regime. I feel that this needs to be cross-checked with the help of advanced experimental techniques. So it is proposed to use high precision digital image correlation (DIC), crystal plasticity finite element method (CP-FEM) or kernel-average-misorientation techniques to compare the strain localization in the short crack and long crack regimes. Also, since both the material bears different type of precipitates it is important to check the important precipitation-strengthening parameters that will have an impact on mechanical behavior of material. So it is proposed to carry out transmission electron microscopy studies in order to report precipitate size, volume fraction, distribution, hardness, inter-particle spacing etc. which will support the susceptibility of strain localization in one material compared to other. Depending on the conclusive results it will be possible to have a better classification of material based on strain localization. Additionally, this study will help in predicting the mechanical behavior of material under fatigue loading conditions.

Moreover, in chapter 5, we have studied about "Effect of strain localization on fatigue crack initiation and fatigue limit prediction of commercial grade precipitation-strengthened Fe-Cr-Ni based steel", we need to consider multiple crack initiation thus we need to be more precise in $\sqrt{area}$ calculation. A better prediction of $\sqrt{area}$ will lead to a better and more closer prediction of experimental fatigue limit.

Acknowledgement

Firstly, I am very grateful to my supervisor, Associate Prof. Shigeru Hamada, for his patience and valuable guidance during the period of my Ph.D. study. He taught me how to study and think, what to innovate and dedicate. He allowed me to make mistakes and gave me opportunities to correct them in research. Under his guidance, I gained not only a wealth of knowledge but also advanced concepts.

I am also thankful to Prof. Hiroshi Noguchi, who is the head of Solid Mechanics Laboratory, for allowing me to conduct my experiments. Not only this, but also, I am very grateful to him that he keeps encouraging me during my research period. I also appreciate that he imparted his considerable, precious time, in keep discussing and analyzing my experimental results.

I am thankful to the committee members, Prof. Hiroshi Noguchi, Prof. Hiroyuki Toda and Prof. Hisao Matsunaga, for their critical views on modifying this thesis.

I am also thankful to Prof. Eiji Akiyama, Associate Prof. Motomichi Koyama and Assistant Prof. Tomohiko Hojo for providing their immense support in conducting a part of this research in Institute for Materials Research (IMR), Tohoku University.

I also want to extend my thanks to Mrs. Masako Kadota and Mrs. Arisa Mapp, laboratory secretaries at Kyushu and Tohoku University respectively, for the care and help they provided in my daily life and study.

I should also thank JICA for their financial and moral support during my PhD. Along with this I would like to thank Dr. Tatsuo Yokoi, from Nippon steel corporation, for providing the specimen material and getting involved in the discussion.

Apart from this, I would also like to thanks all my laboratory friends at Kyushu and Tohoku University for their caring and helping nature during my research period. I specially thanks Abbas, Liu for their frequent availability as and when I needed their help and support.

Finally, I would like to thanks my family, specially my mother, friends in India for their emotional support.